Chem, Volume *7*

Supplemental information

Breaking the trade-off between selectivity and adsorption capacity for gas separation

Naveen Kumar, Soumya Mukherjee, Nathan C. Harvey-Reid, Andrey A. Bezrukov, Kui Tan, Vinicius Martins, Matthias Vandichel, Tony Pham, Lisa M. van Wyk, Kolade Oyekan, Amrit Kumar, Katherine A. Forrest, Komal M. Patil, Leonard J. Barbour, Brian Space, Yining Huang, Paul E. Kruger, and Michael J. Zaworotko

Supplemental Information for

Breaking the trade-off between selectivity and adsorption capacity for C_2H_2/CO_2 separation

Naveen Kumar,[1,†] Soumya Mukherjee,[1,†] Nathan C. Harvey-Reid,[2] Andrey A. Bezrukov,[1] Kui Tan,[3] Vinicius Martins,[4] Matthias Vandichel,[1] Tony Pham,[5] Lisa M. van Wyk,[6] Kolade Oyekan,[3] Amrit Kumar,[1] Katherine A. Forrest,[5] Komal M. Patil,[2] Leonard J. Barbour,[6] Brian Space,[5] Yining Huang,[4] Paul E. Kruger,[2] and Michael J. Zaworotko[1,]*
*correspondence: xtal@ul.ie
[†]These authors contributed equally.

Tables S1-S4

Materials and Methods.

Starting materials, reagents and solvents were purchased from commercial sources (Sigma-Aldrich, TCI Europe N.V., AK Scientific Inc. USA) and used without further purification.

Powder X-ray Diffraction (PXRD). Diffractograms were recorded using a PANalytical Empyrean™ diffractometer equipped with a PIXcel^{3D} detector operating in scanning line detector mode with an active length of 4 utilizing 255 channels. The diffractometer is outfitted with an Empyrean Cu LFF (long fine-focus) HR (9430 033 7310x) tube operated at 40 kV and 40 mA and CuK$_{\alpha}$ radiation (λ_{α} = 1.540598 Å) was used for diffraction experiments. Continuous scanning mode with the goniometer in the theta-theta orientation was used to collect the data. Incident beam optics included the Fixed Divergences slit with anti-scatter slit PreFIX module, with a 1/8° divergence slit and a 1/4° anti-scatter slit, as well as a 10 mm fixed incident beam mask and a Soller slit (0.04 rad). Divergent beam optics included a P7.5 anti-scatter slit, a Soller slit (0.04 rad) and a Ni-*β* filter. In a typical experiment, 25 mg of sample was dried, ground into a fine powder and was loaded on a zero background silicon disks. The data was collected from 5°–40° (2θ) with a step-size of 0.0131303° and a scan time of 30 seconds per step. Crude data were analyzed using the X'Pert HighScore Plus™ software V 4.1 (PANalytical, The Netherlands).

Variable Temperature Powder X-ray Diffraction (VT-PXRD). Diffractograms at different temperature were recorded using a PANalytical X'Pert Pro-MPD diffractometer equipped with a PIXcel3D detector operating in scanning line detector mode with an active length of 4 utilizing 255 channels. Anton Paar TTK 450 stage coupled with the Anton Paar TCU 110 Temperature Control Unit was used to record the variable temperature diffractograms. The diffractometer is outfitted with an Empyrean Cu LFF (long fine-focus) HR (9430 033 7300x) tube operated at 40 kV and 40 mA and CuKα radiation (λα = 1.54056 Å) was used for diffraction experiments. Continuous scanning mode with the goniometer in the theta-theta orientation was used to collect the data. Incident beam optics included the Fixed Divergences slit, with a 1/4° divergence slit and a Soller slit (0.04 rad). Divergent beam optics included a P7.5 anti-scatter slit, a Soller slit (0.04 rad), and a Ni-β filter. In a typical experiment, 20 mg of sample was dried, ground into a fine powder and was loaded on a zero background sample holder made for Anton Paar TTK 450 chamber. The data was collected from 5°–45° (2θ) with a step-size of 0.0167113° and a scan time of 50 seconds per step. Crude data were analyzed using the X'Pert HighScore Plus™ software V 4.1 (PANalytical, The Netherlands).

Thermogravimetric Analysis (TGA). Thermograms were recorded under nitrogen using TGA instrument TA Q50 V20.13 Build 39. Platinum pans and a flow rate of 60 cm^3 min^{-1} for the nitrogen gas were used for the experiments. The data was collected in the High Resolution Dynamic mode with a sensitivity of 1.0, a resolution of 4.0 and a temperature ramp of 20 °C min^{-1} up to 550 °C. The data was evaluated using the T.A. Universal Analysis suite for Windows XP/Vista Version 4.5A.

Gas Sorption Measurements. For gas sorption experiments, ultrahigh-purity gases were used as received from BOC Gases Ireland: research-grade He (99.999%), CO_2 (99.995%), C_2H_2 (98.5%) and N_2 (99.998%). Adsorption experiments (up to 1 bar) for 77 K N_2 and 195 K CO_2 were performed on Micromeritics Tristar II 3030. Micromeritics 3Flex surface area and pore size analyser 3500 was used for collecting the 273 and 298 K sorption isotherms for C_2H_2 and CO_2. Before sorption measurements, activation of all six different **HUMs** was achieved by degassing the air-dried samples on a SmartVacPrep™ using dynamic vacuum and heating for 8 h (each sample heated from RT to 333 K with a ramp rate of 5 °C). Brunauer-Emmett-Teller (BET) surface areas were determined from the CO_2 and N_2 adsorption isotherms at 195 K and 77 K respectively, using the Micromeritics Microactive software. About 100 mg of activated samples were used for the measurements. A Julabo temperature controller was used to maintain a constant temperature in the bath throughout the experiment. The bath temperatures of 273 and 298 K were precisely controlled with a Julabo ME (v.2) recirculating control system containing a mixture of ethylene glycol and water. The low temperature at 77 K and 195 K were controlled by a 4 L Dewar filled with liquid N_2 and dry ice/acetone, respectively. At every interval of two independent isotherms recorded for any sorbent, samples were regenerated by degassing over 5 h under high vacuum at 333 K, before commencing the next sorption experiment.

Accelerated Stability Protocol. In a typical experiment, as followed by the pharmaceutical industries,[1] microcrystalline samples of each of the HUMs was exposed to 313 K and 75 % RH for 1, 7 and 14 days (d) in a desiccator (corresponding to 4 d, 1 month and 2 months shelf-life, respectively). These conditions were achieved by using a supersaturated aqueous solution of NaCl maintained at 313 K in a closed desiccator. After 1, 7 and 14 d, sample aliquots were removed from desiccator and characterized by PXRD measurements in order to detect signs the sample which may have been affected by humidity.

Single-gas sorption cycling test. Gravimetric uptakes were recorded under pure C_2H_2 gas, using TGA instrument TA Q50 V20.13 Build 39. Platinum pans and gas flow rates of 10 cm^3/min were used in these experiments. Desorption at 60 °C was performed under N_2 flow of 20 cm^3/min. The data was collected in the High Resolution Dynamic mode with a sensitivity of 1.0, a resolution of 4.0 and the weight changes during C_2H_2 gas adsorption step were monitored under isothermal condition at 60 °C. The data was evaluated using the T.A. Universal Analysis suite for Windows

XP/Vista Version 4.5A. The flowrates of all these sorbates were monitored by pre-calibrated Bronkhorst Mass Flow Controllers.

Breakthrough Experiments. In typical breakthrough experiments, ~ 0.5 g of pre-activated **HUMs** were placed in quartz tubing (8 mm diameter; 8 mm x 6 mm x 400 mm) to form fixed beds. First, the adsorbent bed was purged under a 30 cm^3 min^{-1} flow of He gas at 333 K for 30 min prior to breakthrough experiment. Upon cooling to room temperature, the gas flow was switched to the desired C_2H_2/CO_2 gas mixture compositions (2:1 and 1:1 respectively), maintained at a total flow rate of 1.0 cm^3 min^{-1}. Herein, 2:1 and 1:1 C_2H_2/CO_2 binary breakthrough experiments were conducted at 298 K for all six **HUMs**. The outlet composition was continuously monitored by a Shimadzu Nexis GC-2030 gas chromatograph until complete breakthrough was achieved. For temperature programmed desorption (TPD), post-breakthrough saturated sorbent beds were heated at a constant rate to 60 °C under He flow, 20 cm^3min^{-1}. The desorbed gases were monitored continuously.

Supplemental Text

Single Crystal X-ray Diffraction.

Single crystal X-ray diffraction data of all the crystals were collected on a Bruker Quest diffractometer equipped with a IμS microfocus X-ray source (Cu Kα, λ = 1.54178 Å; Mo *K*α, (λ = 0.71073 Å) and CMOS detector. APEX3 was used for collecting, indexing, integrating and scaling the data.[2] Open-flow nitrogen attachment with Oxford Cryosystem was used for low temperature measurements. Absorption correction was performed by multi-scan method.[3] Space groups were determined using XPREP[4] as implemented in APEX3. All the scaled data were solved using intrinsic phasing method (XT)[5] and refined on F^2 using SHELXL[6] inbuilt in OLEX2 v1.2 (2009) program.[7] All non-hydrogen atoms present in the frameworks were refined anisotropically. Hydrogen atoms were located at idealized positions from the molecular geometry and refined isotropically with thermal parameters based on the equivalent displacement parameters of their carriers. The reported structures were refined from twin crystals. Each of the crystals of **SIFSIX-21-Ni**, **TIFSIX-4-Ni**, **SIFSIX-21-Cu** and **TIFSIX-4-Cu** was revealed as a two-domain twin. Appropriate PART instructions were used to model framework disorder in these structures. Where needed, especially for disordered sections of the frameworks, restraints (SIMU, DELU, ISOR, RIGU) were used to ensure proper geometry of the molecules and to allow anisotropic refinement of non-hydrogen atoms. Crystallographic data for all the HUMs reported in this paper, are summarised in Table S2. Crystal structures are deposited to the Cambridge Crystallographic Data Centre (CCDC 2052024-2052025; 2052046-2052047).

Adsorption Energy Calculations.

Except the six HUMs studied herein, other Q_{st} plots and associated parameters were obtained from data extraction using WebPlotDigitizer.[8]

A virial-type expression of the below form was used to fit the combined 273 and 298 K isotherm data of C_2H_2 and CO_2 for all six **HUMs**, where P is the pressure described in Pa, N is the adsorbed amount in mmol g^{-1}, T is the temperature in K, a_i and b_i are virial coefficients and m and n are the number of coefficients used to describe the isotherms. Q_{st} is the coverage-dependent enthalpy of adsorption and R is the universal gas constant. All fitting was performed using Origin Pro 8.[9] Fitting parameters thus obtained for the six **HUMs** can be found in Figures S33–S44.

$$\ln P = \ln N + \sum_{i=0}^{m} a_i N_i + \sum_{i=0}^{n} \binom{n}{k} b_i N_i$$

Q_{st} was calculated from the virial model using the equation below.

$$-Q_{st} = -R \sum_{i=0}^{m} a_i N_i$$

Adsorption Selectivity Calculations.

The selectivities for the adsorbate mixture composition of interest were calculated from the single-component adsorption isotherms using Ideal Adsorbed Solution Theory (IAST), using a modified version of the program pyIAST.[10] First, the single-component isotherms for the gas sorbates at 298 K were fitted to the dual-site Langmuir-Freundlich (DLF) equation.[11]

$$n(P) = \frac{q_1 (k_1 P)^{n_1}}{1 + (k_1 P)^{n_1}} + \frac{q_2 (k_2 P)^{n_2}}{1 + (k_2 P)^{n_1}}$$

In this equation, q_i is the amount adsorbed per unit mass of material (in mmol g^{-1}), P is the total pressure (in bar) of the bulk gas at equilibrium with the adsorbed phase, q_1 and q_2 are the saturation uptakes (in mmol g^{-1}) for sites 1 and 2 respectively, k_1 and k_2 are the affinity coefficients (in bar^{-1}) for sites 1 and 2 respectively and n_1^{-1} and n_2^{-1} represent the deviations from the ideal homogeneous surface (unit-less) for sites 1 and 2 respectively. Final selectivity for adsorbate *i* relative to adsorbate *j* was calculated using the following equation.

$$S_{i/j} = \frac{(x_i/x_j)}{(y_i/y_j)}$$

Here, x_i and x_j are the mole fractions of components *i* and *j*, respectively, in the adsorbed phase and y_i and y_j are the mole fractions of components *i* and *j*, respectively, in the gas phase. Dual-site Langmuir-Freundlich equation fitting parameters thus obtained for all the adsorbents can be found in Table S3.

Separation factor / Separation selectivity Calculations.

The amount of adsorbed gas *i* (q_i) is calculated from the breakthrough curve as follows:

$$q_i = \frac{V_i T_0 - V_{dead} - \int_0^{t_0} V_e \, \Delta T}{m}$$

Here, V_i is the influent flow rate of gas (cm^3 min^{-1}), V_e is the effluent flow rate of gas (cm^3 min^{-1}), V_{dead} is the dead volume of the system (cm^3), T_0 is the adsorption time (min) and *m* is the mass of the sorbent (g).[12]

The amount of adsorbed gas *i* (q_i) is calculated from the breakthrough curve as follows:

$$q_i = \frac{V_T \Delta T P_i}{m}$$

Here, V_T is the total flow rate of gas (cm^3 min^{-1}), P_i is the partial pressure of gas *i* (bar), ΔT is the time for initial breakthrough of gas *i* to occur (min) and *m* is the mass of the sorbent (g). The separation factor, also known as separation selectivity (α) for the breakthrough experiment *i.e.* breakthrough derived selectivity is determined as follows:

$$\alpha = \frac{q_{1\,y_2}}{q_{2\,y_1}}$$

y_i is the partial pressure of gas i in the gas mixture. In the case where one gas component has negligible adsorption, the amount of gas adsorbed is treated as ≤ 1 cm^3 for calculations.

For C_2H_2/CO_2 DCB experiments, the C_2H_2 concentration is defined by:

$$Concentration(\mathrm{C_2H_2}) = \frac{signal(\mathrm{C_2H_2})}{signal(\mathrm{C_2H_2}) + signal(\mathrm{CO_2})}$$

CO_2 purity is defined by:

$$Purity(\mathrm{CO_2}) = \frac{signal(\mathrm{CO_2})}{signal(\mathrm{C_2H_2}) + signal(\mathrm{CO_2})}$$

The C_2H_2 uptake calculation in breakthrough experiment is defined by:

$$n(\mathrm{C_2H_2}) = \frac{\int_0^{t_2}(u_i y_{C_2H_2} - u_e(t)y_e(t)A dt}{V_m} = \frac{F \times y_{C_2H_2} \times \int_0^{t_2}(1 - \frac{C(t)}{C_0})dt}{V_m}$$

$$= \frac{F \times y_{C_2H_2} \times (t_2 - \int_0^{t_2}\frac{C(t)}{C_0}\,dt)}{V_m}$$

Where $n(\mathrm{C_2H_2})$ is the C_2H_2 uptake in mmol g^{-1}, t_2 is the C_2H_2 saturation time, $u_e(t)$ is the transient linear velocity in outlet gas, $y_e(t)$ is the transient C_2H_2 volume fraction in the outlet gas, u_i is the transient linear velocity in inlet gas, F is the inlet gas volume flow rate, $y_{C_2H_2}$ is the volume fraction of C_2H_2 in the mixed gas, $\int_0^{t_2}\frac{C(t)}{C_0}\,dt$ is the integrated area between the C_2H_2 breakthrough curve and the X-axis within the range 0 and t_2, $C(t)$ is the detected C_2H_2 concentration in the outlet gas, C_0 is the detected C_2H_2 concentration in the outlet gas and V_m is molar volume of the gas.

In situ Variable Pressure PXRD.

Crystals of each material were activated in a glass oven at 40 °C under vacuum (pressure: ~1 x 10^{-2} millibar) for approximately 4 h. The activated solid was ground into a fine powder using a pestle and mortar and packed into an environmental gas cell (EGC). The EGC consists of a 0.5 mm glass Lindemann Capillary attached to a steel nut with epoxy, which is then screwed into a valve body. The EGC allows for pressurisation/evacuation of the immediate sample environment while the valve allows for this environment to be isolated and transported to the diffractometer. To determine a diffractogram under vacuum an EGC was attached to a manifold, that in turn was connected to a vacuum pump (pressure: ~7 x 10^{-3} millibar) and left to equilibrate for approximately 4 h. For the variable pressure studies an EGC was attached to a C_2H_2 cylinder *via* a regulator. The system was pressurised and left to equilibrate under static pressure for approximately 4–6 h. After the valve to the EGC was closed, it could be transported to the diffractometer. A PANalytical XPERT-PRO diffractometer was used to record experimental diffractograms. The diffractometer utilises Bragg-Brentano geometry and Cu Kα radiation (λ = 1.5418 Å) as the incident beam. Intensity data were recorded using a capillary spinner to which the EGC was attached. The samples were scanned between 4° and 45° 2θ with a varying scan speed and step size, which was dependent on the nature of the sample.

In situ Infrared (IR) Spectroscopy.

In situ IR measurements were performed on a Nicolet 6700 FTIR spectrometer using a liquid N_2-cooled mercury cadmium telluride (MCT-A) detector. A vacuum cell is placed in the sample compartment of the infrared spectrometer with the sample at the focal point of the beam. The samples (~5 mg) were gently pressed onto KBr pellet and placed into a cell that is connected to a vacuum line for evacuation. The samples of **NbOFFIVE-3-Cu** and **SIFSIX-21-Ni** were activated by evacuation overnight at 60 ºC, respectively, and then cooled back to room temperature for CO_2 and C_2H_2 gas exposure measurement. Note that the IR absorption of the gas phase is prohibitively high at this pressure, making the observation of adsorbed molecules impossible. We pumped out the gas phase and recorded spectra as a function of time in the desorption process. Within ~5 seconds of evacuation, the pressure of gas-phase drops below ~500 mTorr (negligible gas-phase IR absorption).

DFT calculation of vibrational bands of pypz linker.

The DFT calculations and IR vibrational modes presented here were obtained using the Jaguar electronic structure program.[13, 14] Geometry relaxation included perturbation of all rotatable proper and improper torsions, except those in rings and double bonds, to ensure convergence at the minimum energy structure. Subsequent single point vibrational frequencies calculation was carried out to obtain the IR spectrum shown in Figure S62. All structure derivatives were computed using the B3LYP-D3 hybrid functional[15] and 6-31G** basis set.[16] The chemical structure images were drawn with Maestro.[17]

Solid-state (SS) NMR Spectroscopy.

100 mg of the **NbOFFIVE-3-Cu** sample was ground into a fine powder, packed into an L-shaped glass tube, and then connected to a Schlenk line where it was left evacuating at room temperature for 24 h. The samples were then loaded with the guest gases ($^{13}CO_2$: 0.4 eq. per metal; C_2D_2: 0.4 and 0.8 eq. per metal) and sealed off from the Schlenk line. The guest-loaded samples were then left at room temperature for 24 h before the NMR experiments to allow for the equilibration.

All SSNMR experiments were carried out using a Varian Infinity Plus NMR spectrometer, equipped with an Oxford 9.4 T wide-bore magnet and a 5 mm HX static Varian/Chemagnetics probe. Static ^{13}C NMR spectra [$\upsilon_0(^{13}C)$ = 100.5 MHz] were referenced to TMS using the high-frequency signal of ethanol at 58.05 ppm as a secondary reference.[18] Experiments were performed using the DEPTH-echo pulse sequence to remove the background from the probe,[19] with a 90° pulse width of 3.2 μs and a 180° pulse width of 6.4 μs. The spectral width was 300 kHz and the optimized recycle delay was 3 s. The number of scans required for static VT ^{13}C ranges from 700 to 1000 scans. Static ^{2}H NMR spectra [$\upsilon_0(^{13}C)$ = 61.3 MHz] were referenced using the signal of D_2O(l) at 4.80 ppm as a secondary reference.[18] A quadrupolar echo pulse sequence of the form ($\pi/2- \tau1- \pi/2- \tau2$) was used with a 90° pulse width of 4.0 μs, a τ_1 of 30.0 μs and a τ_2 of 30.0 μs. The spectral width was 500 kHz and the optimized ^{2}H recycle delay was 0.5 s. The number of scans required for static ^{2}H VT SSNMR experiments ranges between 3000 and 3200 scans. The WSolids software package[20] was used to simulate all static SSNMR spectra in order to extract the NMR parameters of gas molecules from observed spectra. The EXPRESS software[21] was used to simulate the effects of guest motion.

Synthesis of compounds.

3,5-dimethyl-1*H*-pyrazol-4-yl)pyridine (pypz) synthesis.

3,5-dimethyl-1*H*-pyrazol-4-yl)pyridine was synthesized following reported procedure.[22]

Preparation of SIFSIX-21-Ni single crystals. Single crystals of the compound **SIFSIX-21-Ni** were obtained by solvothermal reaction as following: a suspension of **pypz** (0.1 mmol, 17 mg) and $NiSiF_6.6H_2O$ (0.05 mmol, 15 mg) in MeOH (3 mL) were reacted at 85 °C in a small 10.5 mL glass vial for overnight, keeping in a fixed-temperature oven. The crystals were collected in *ca.* 75 % yield by filtration and washed with MeOH three times.

Preparation of TIFSIX-4-Ni single crystals. MeOH (2 mL) was carefully layered over a solution of $NiTiF_6.6H_2O$ (0.05 mmol, 16 mg) 2 mL of MeOH to which **pypz** (0.1 mmol, 17 mg) in 2 mL of MeOH was layered. Light pink single crystals were obtained after several days with *ca.* 60 % yield. The crystals were harvested by filtration and washed with MeOH three times.

Preparation of SIFSIX-21-Cu single crystals.

Single crystals of the compound **SIFSIX-21-Cu.** An ethylene glycol solution (2 ml) of $Cu(NO_3)_2$ (8.4 mg, 0.035 mmol) and $(NH_4)_2SiF_6$ (6.2 mg, 0.035 mmol) was prepared and carefully transferred to a test tube of 10 cm length and 1 cm diameter. A buffer solution of ethylene-glycol:methanol (1:1/v:v) was prepared and 6 ml of this was carefully layered above the first solution, creating a defined layer between the two. A methanol solution (2 ml) of ligand **pypz** (12 mg, 0.07 mmol) was layered on top of the buffer solution creating a third layer. The test-tube was sealed and left to stand. After two weeks, small blue/violet coloured crystals formed on the inside of the test-tube.

Preparation of TIFSIX-4-Cu single crystals.

Single crystals of the compound **TIFSIX-4-Cu.** Crystals were made following the same method as that used for **TIFSIX-4-Cu**, however $(NH_4)_2TiF_6$ (6.7 mg, 0.035 mmol) was used in place of $(NH_4)_2SiF_6$.

Preparation of NbOFFIVE-3-Ni crystalline powder. Crystalline powder of **NbOFFIVE-3-Ni** can be prepared by solvothermal reaction as following: a suspension of **pypz** (1 mmol, 170 mg) and $NiNbOF_5.6H_2O$ (0.5 mmol, 185 mg) in MeOH (15 mL) were reacted at 85 °C in a 100 ml Schott Duran® bottle for overnight, keeping in a fixed-temperature oven. The powder was collected in *ca.* 70% yield by filtration and washed with MeOH three times.

Preparation of NbOFFIVE-3-Cu crystalline powder. Crystalline powder of **NbOFFIVE-3-Cu** can be prepared from the similar procedure of **NbOFFIVE-3-Ni**, using $CuNbOF_5.6H_2O$ (0.5 mmol, 187 mg) instead of $NiNbOF_5.6H_2O$.

Preparation of SIFSIX-21-Cu crystalline powder. Crystalline powder of **SIFSIX-21-Cu** can be prepared from the similar procedure of **NbOFFIVE-3-Ni**, using $CuSiF_6.6H_2O$ (0.5 mmol, 157 mg) instead of $NiNbOF_5.6H_2O$.

Preparation of TIFSIX-4-Cu crystalline powder. Crystalline powder of **TIFSIX-4-Cu** can be prepared from the similar procedure of **NbOFFIVE-3-Ni**, using $CuTiF_6.6H_2O$ (0.5 mmol, 167 mg) instead of $NiNbOF_5.6H_2O$.

Preparation of TIFSIX-4-Ni crystalline powder. Crystalline powder of **TIFSIX-4-Ni** can be prepared from the similar procedure of **NbOFFIVE-3-Ni**, using $NiTiF_6.6H_2O$ (0.5 mmol, 164 mg) instead of $NiNbOF_5.6H_2O$.

Scale up for SIFSIX-21-Ni. SIFSIX-21-Ni can be scaled up from the similar procedure of **NbOFFIVE-3-Ni**, using $NiSiF_6.6H_2O$ (0.5 mmol, 154 mg) instead of $NiNbOF_5.6H_2O$.

Modelling Studies.

The binding sites for C_2H_2 and CO_2 in **SIFSIX-21-Ni** were determined through classical molecular simulations. All parametrizations and simulations were performed on the single X-ray crystallographic structure published herein for the material.

All atoms of **SIFSIX-21-Ni** were treated with Lennard-Jones (LJ) parameters (ε and σ), point partial charges and point polarizabilities in order to model repulsion/dispersion, stationary electrostatic and many-body polarization interactions, respectively. The LJ parameters for all C and H atoms were taken from the Optimized Potentials For Liquid Simulations – All Atom (OPLS-AA) force field,[23] while those for the N, F, Si and Ni atoms were taken from the Universal Force Field (UFF).[24] The partial charges for the chemically distinct atoms in **SIFSIX-21-Ni** were determined through the Restrained Electrostatic Potential (RESP) method[25] using the CP2K program.[26] The exponential damping-type polarizability values for all C, H, N and F atoms were taken from a carefully parametrized set provided by the work of van Duijnen and Swart.[27] The polarizability parameter for Si^{4+} and Ni^{2+} was calculated in previous work[28, 29] and used herein. After the hydrogen nuclei were optimized, a Restrained Electrostatic Surface Potential (RESP) charge fit was performed to obtain partial charges on each atom for use in empirical simulation. Universal force Field (UFF)[24] radii were used during the sphere sampling protocol.

Simulated annealing (SA) calculations[30] were performed for a single molecule of both adsorbates through a canonical Monte Carlo (*NVT*) process in a 2 × 2 × 2 supercell of **SIFSIX-21-Ni**. This was done in order to identify the most favorable binding site for both adsorbates in the material. All HUM atoms were kept fixed at their crystallographic positions throughout the simulations. A spherical cut-off distance of 14.6342 Å, representing half the shortest supercell dimension length, was used for the simulations. C_2H_2 and CO_2 were modeled using polarizable potentials of the respective adsorbates that were developed previously.[31, 32] The total potential energy of the HUM–adsorbate system was calculated through the sum of the repulsion/dispersion, stationary electrostatic and many-body polarization energies. These were calculated using the LJ potential,[33] the Ewald summation technique,[34, 35] and a Thole-Applequist type model,[36-39] respectively. SA calculations for both adsorbates utilized an initial temperature of 500 K and this temperature was scaled by a factor of 0.99999 after every 1.0×10^3 Monte Carlo steps. The simulations continued until the temperature of the system dropped below 10 K.

Next, canonical Monte Carlo (CMC) simulations were performed for a single molecule of C_2H_2 and CO_2, individually, positioned at their global minimum in **SIFSIX-21-Ni**. This was done in order to evaluate the averaged classical potential energy for both adsorbates about their energy minimum position in the material. As with the SA calculations, the simulations were carried out within the rigid 2 × 2 × 2 supercell of the HUM using the same force fields. The CMC simulations were performed at a temperature of 298 K and a pressure of 0.10 atm. These simulations ran for a total of 1.0×10^6 Monte Carlo steps to ensure reasonable ensemble averages for the total potential energy of the system. The averaged classical potential energies for C_2H_2 and CO_2 localized about their energy minimum position in **SIFSIX-21-Ni** are presented in Table S4. All SA calculations and CMC simulations were carried out using the Massively Parallel Monte Carlo (MPMC) code.[40, 41]

Modelling details of C_2H_2 and CO_2 sites which corresponds to the Figure S53.

To study the C_2H_2 and CO_2 binding sites in **SIFSIX-21-Ni** systematically, periodic DFT calculations are performed with the Vienna Ab Initio Simulation Package (VASP 5.4.4).[42, 43] To describe the interactions between the HUM and adsorbates accurately, we opted for the BEEF-vdW functional.[44] This functional is parametrized with training data based on the CCSD(T) method, it is therefore also an excellent choice to account for van der Waals interactions as well as hydrogen bonds especially valuable for the comparison of CO_2 and C_2H_2 adsorption enthalpies. The one-electron Kohn-Sham orbitals were expanded in a plane wave basis set with a kinetic energy cut-off of 550 eV for all calculations. PAW potentials are employed to describe the interaction between the valence electrons and the core.[45] The HUM is first structurally cell-optimized (Γ-point) until the largest force is smaller than 0.02 eV/Å. Afterwards, the atomic positions of the HUM-lattice are fixed and the adsorbates are optimized until the largest force is smaller than 0.01 eV/Å. Furthermore, a Gaussian smearing of 0.05 eV is applied to improve convergence,[42] while the convergence criterion for the electric self-consistent field (SCF) problem is set to 10^{-5} eV for all optimizations. For the energy calculations on the converged structures, the reciprocal space integration over the Brillouin zone is approximated with finite sampling using

Monkhorst-Pack grids [46, 47] using a 3x3x3 k-point grid. For the optimized binding site of C_2H_2 (Figure S53a), there were no imaginary modes observed, while for the optimized binding sites of CO_2, there are 1 or 2 imaginary modes for the geometries given in Figures S53b and S53c, respectively. For the calculation of the enthalpies, these imaginary modes are replaced by an arbitrary mode of 100 cm^{-1}. To verify the local minima, a relevant partial Hessian vibrational analysis (PHVA) is employed, keeping all atoms from the framework fixed except the adsorbate. The PHVA is used also to obtain zero-point corrections and enthalpy contributions.[48, 49] The numerical partial Hessian is calculated by displacements in x, y and z-directions of ±0.004 Å and the vibrational modes are extracted using the normal mode analysis as implemented in the post-processing toolkit TAMKIN.[50]

Powder X-ray Diffraction.

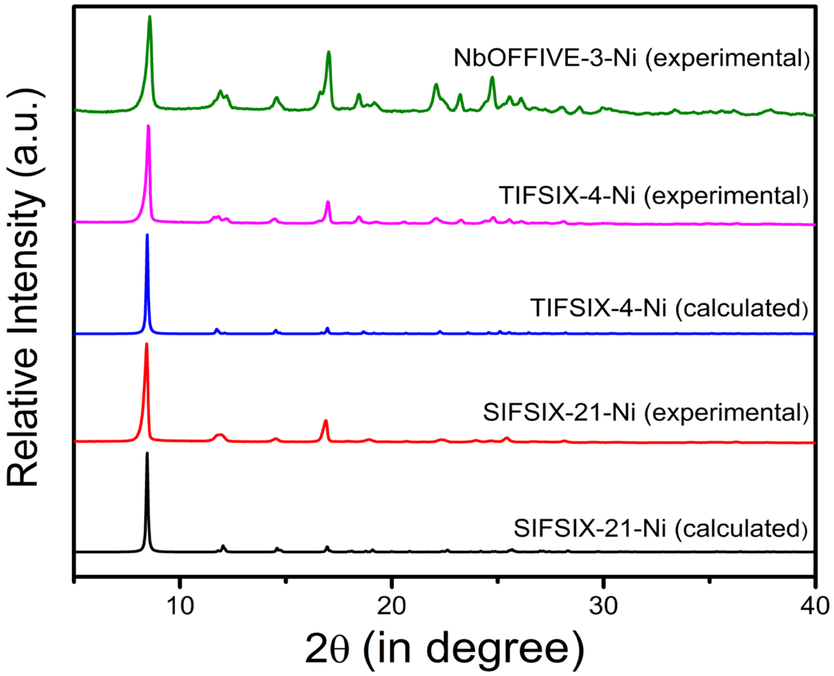

Figure S1. PXRD profiles of **SIFSIX-21-Ni, TIFSIX-4-Ni and NbOFFIVE-3-Ni**, validating phase purity.

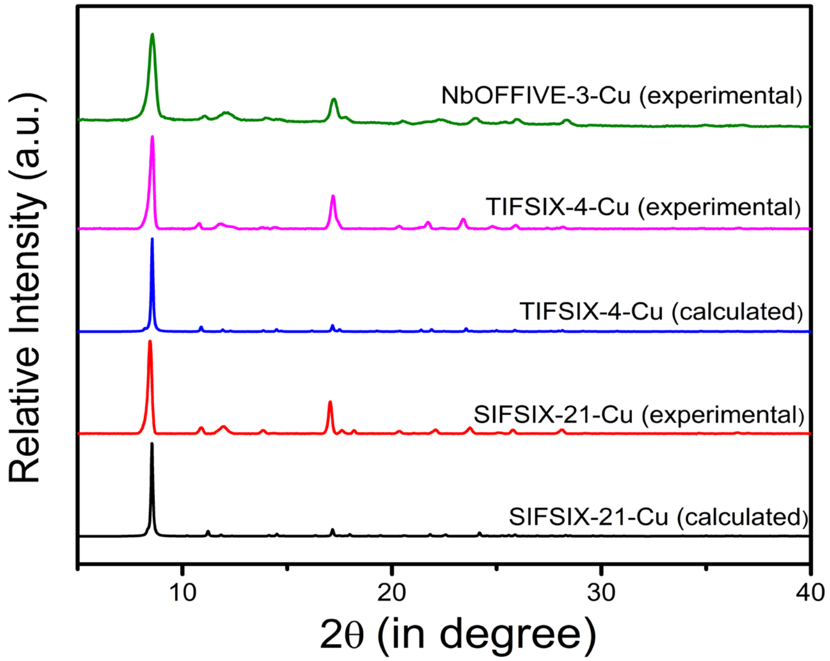

Figure S2. PXRD profiles of **SIFSIX-21-Cu, TIFSIX-4-Cu and NbOFFIVE-3-Cu**, validating phase purity.

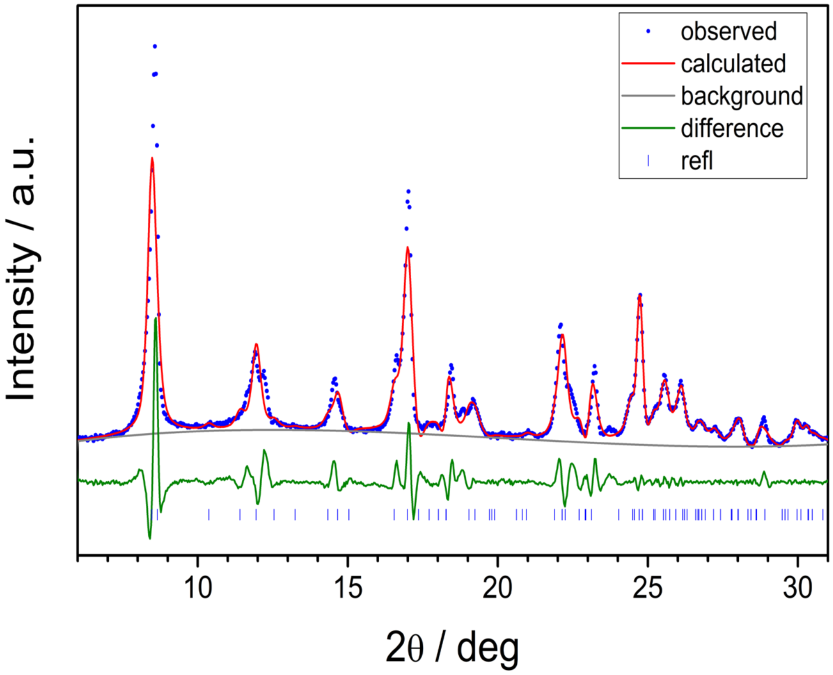

Figure S3. Pawley profile fit of the PXRD patterns of **NbOFFIVE-3-Ni**. Space group = *Pnna*, a = 14.804(8) Å, b = 15.50(15) Å, c = 14.10(12) Å, *α* = 90°, *β* = 90°, *γ* = 90°, V = 3236(3) Å^3, Rwp = 16.9 %.

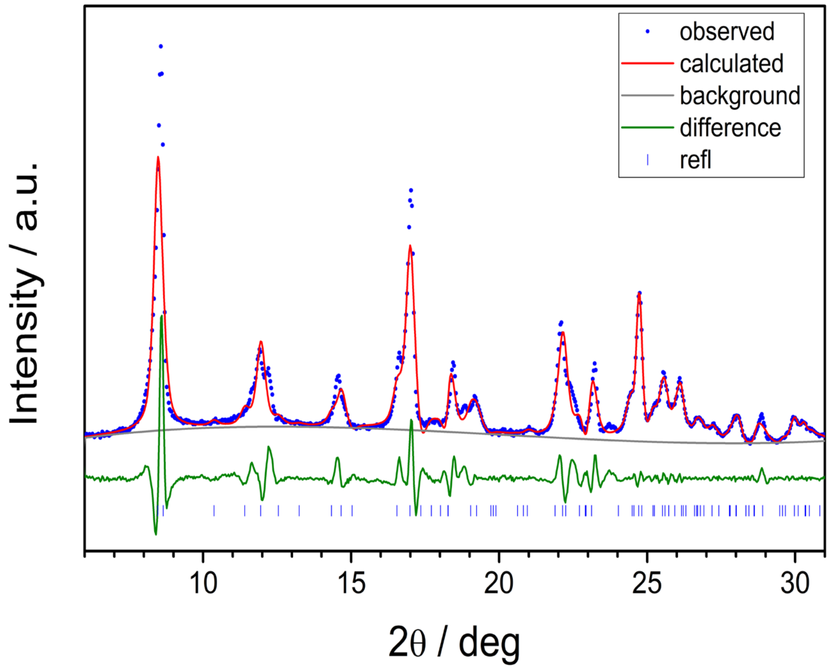

Figure S4. Pawley profile fit of the PXRD patterns of **NbOFFIVE-3-Cu**. Space group = *Pnna*, a = 14.894(3) Å, b = 15.705(3) Å, c = 14.272(3) Å, *α* = 90°, *β* = 90°, *γ* = 90°, V = 3338(17) Å^3, Rwp = 9.18 %.

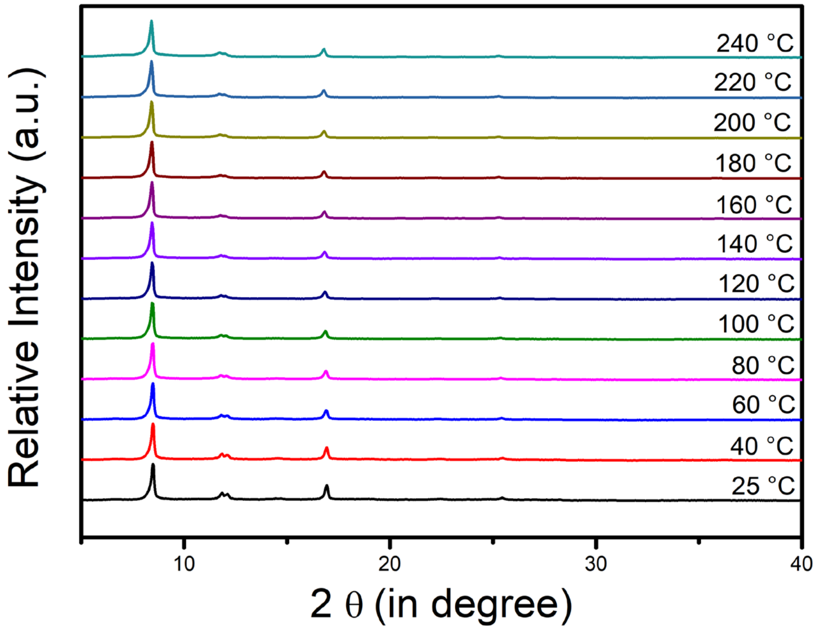

Figure S5. Variable temperature (VT) PXRD profiles of **SIFSIX-21-Ni**.

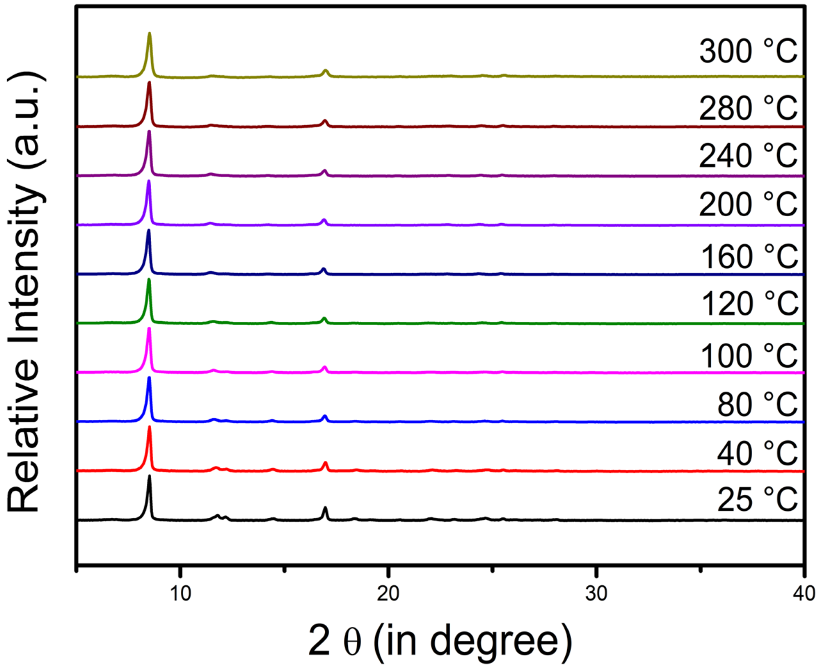

Figure S6. VT-PXRD profiles of **TIFSIX-4-Ni**.

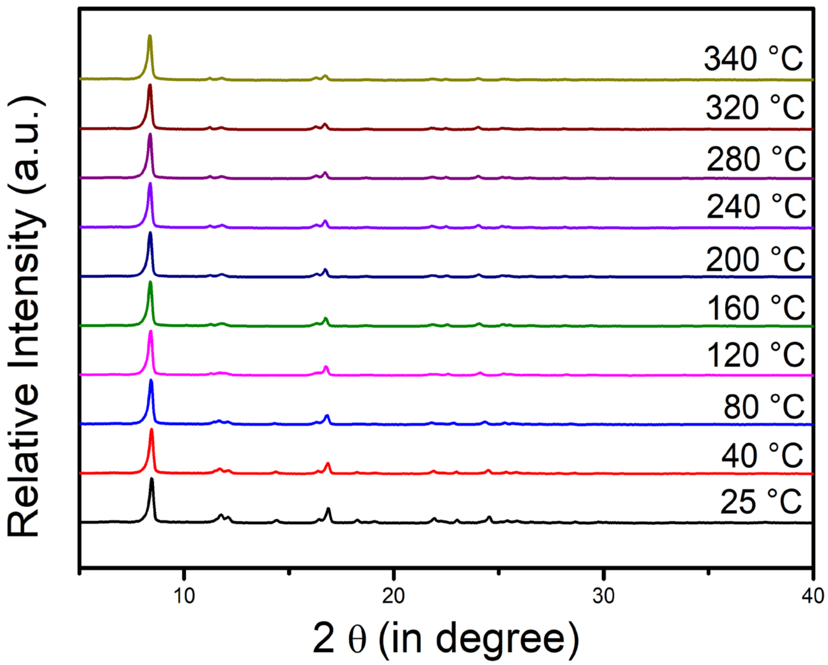

Figure S7. VT-PXRD profiles of **NbOFFIVE-3-Ni**.

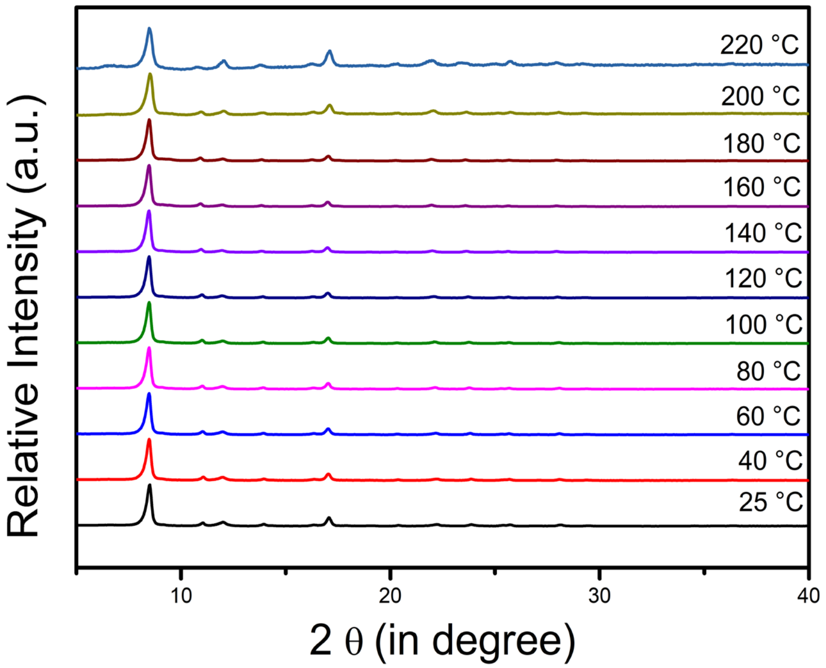

Figure S8. VT-PXRD profiles of **SIFSIX-21-Cu**.

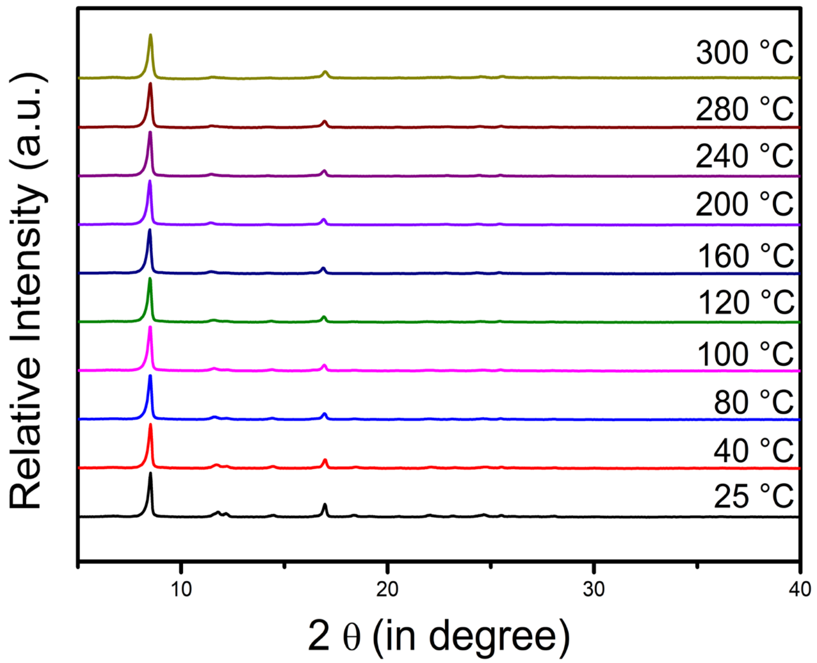

Figure S9. VT-PXRD profiles of **TIFSIX-4-Cu**.

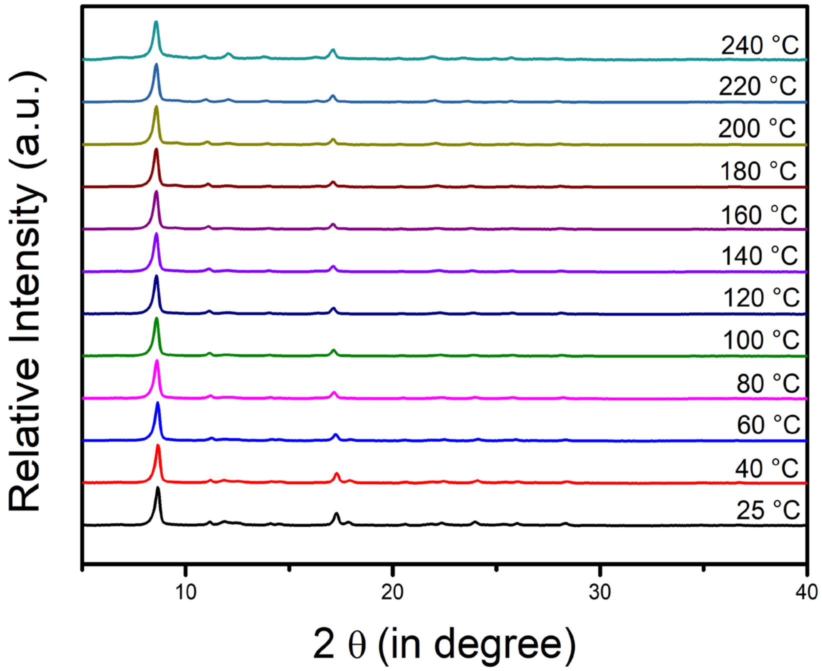

Figure S10. VT-PXRD profiles of **NbOFFIVE-3-Cu**.

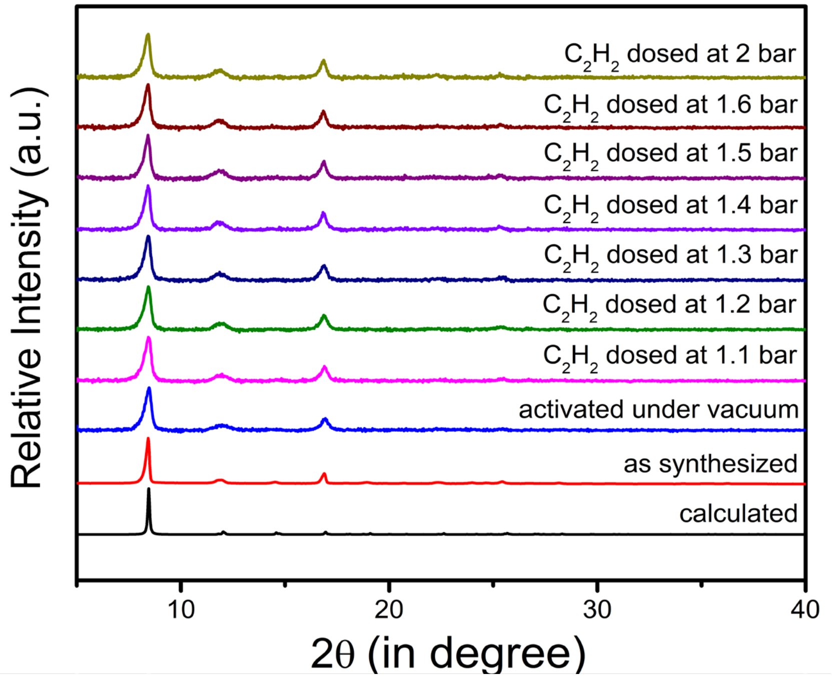

Figure S11. *In situ* PXRD profiles of **SIFSIX-21-Ni** on C_2H_2 dosing.

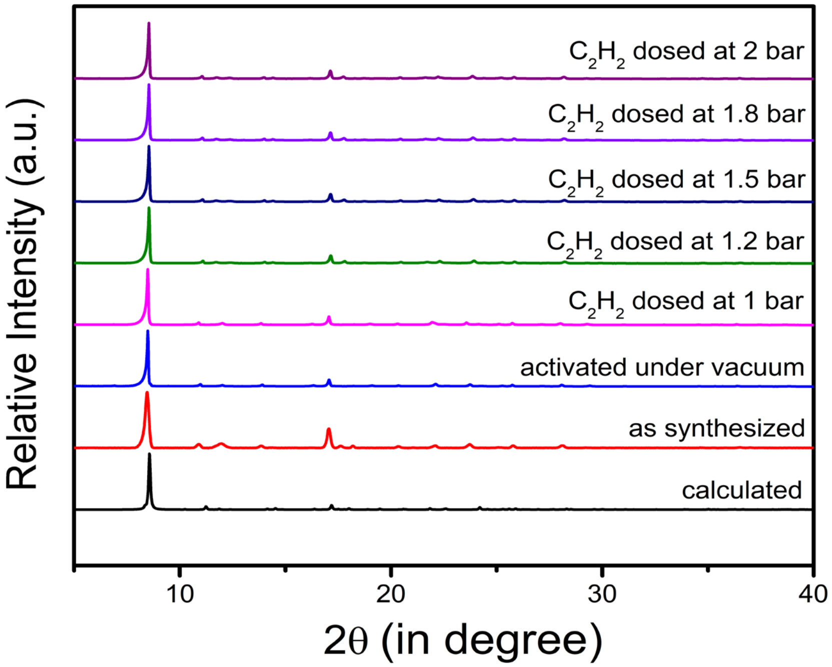

Figure S12. *In situ* PXRD profiles of **SIFSIX-21-Cu** on C_2H_2 dosing.

Thermogravimetric Analysis (TGA).

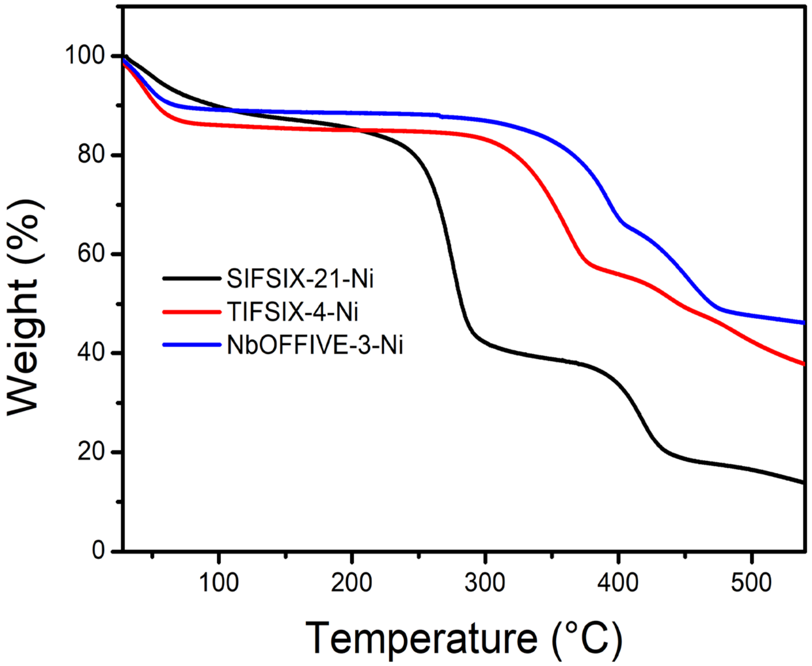

Figure S13. Thermogravimetric analysis profiles of the as-synthesised **SIFSIX-21-Ni, TIFSIX-4-Ni** and **NbOFFIVE-3-Ni**.

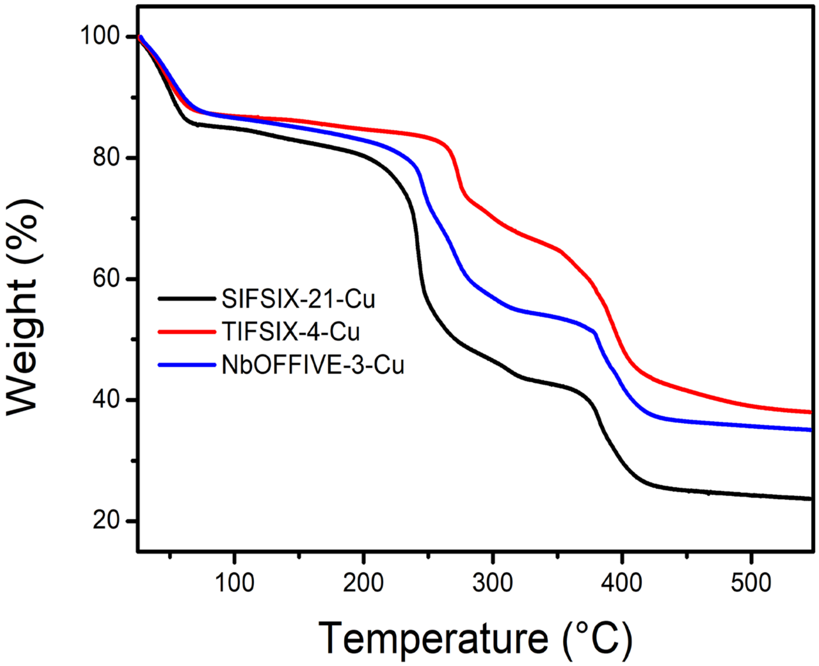

Figure S14. Thermogravimetric analysis profiles of the as-synthesised **SIFSIX-21-Cu, TIFSIX-4-Cu** and **NbOFFIVE-3-Cu**.

Gas Sorption Isotherms.

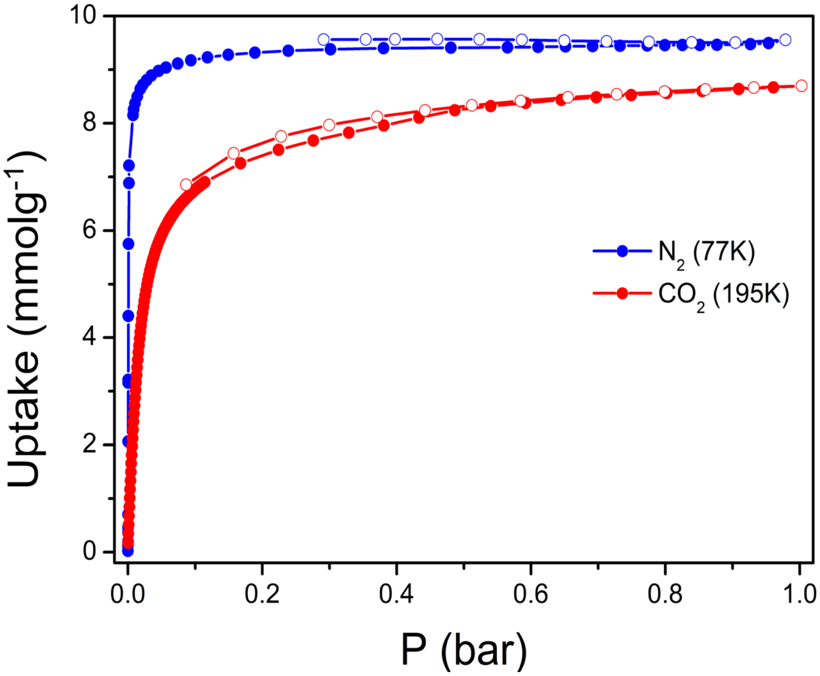

Figure S15. Low temperature CO_2 and N_2 sorption isotherms for **SIFSIX-21-Ni** (filled shape: adsorption; hollow shape: desorption) with BET surface areas 871 m^{2}g^{-1} and 776 m^{2}g^{-1} determined from N_2 and CO_2 isotherms respectively.

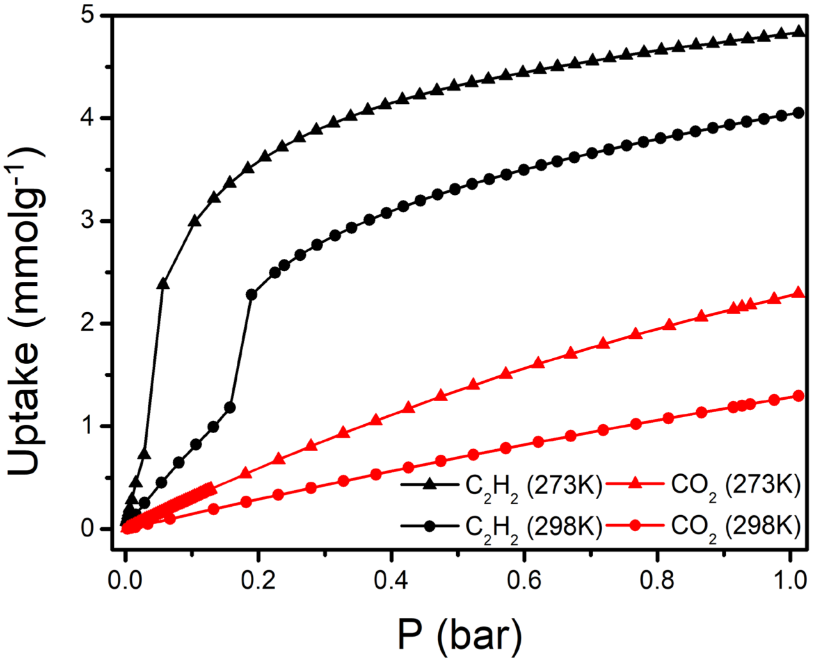

Figure S16. C_2H_2 and CO_2 adsorption isotherms for **SIFSIX-21-Ni**.

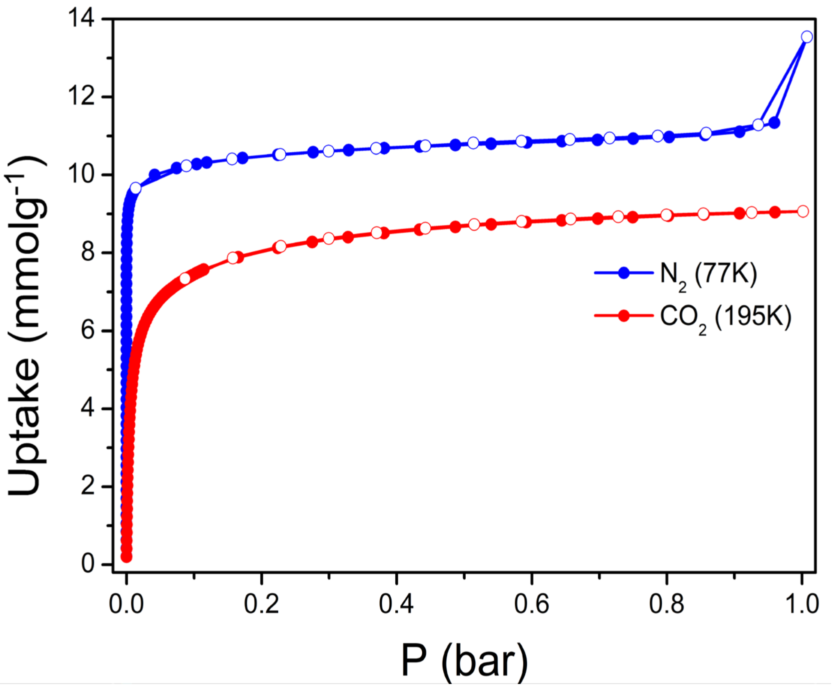

Figure S17. Low temperature CO_2 and N_2 sorption isotherms for **TIFSIX-4-Ni** (filled shape: adsorption; hollow shape: desorption) with BET surface areas 931 m^{2}g^{-1} and 700 m^{2}g^{-1} determined from N_2 and CO_2 isotherms respectively. Last adsorption data point is an outcome of condensation in inter-particle voids (similar to other physisorbents, such as **ZIF-8**, microporous silica material, and carbon nitride).[51-54]

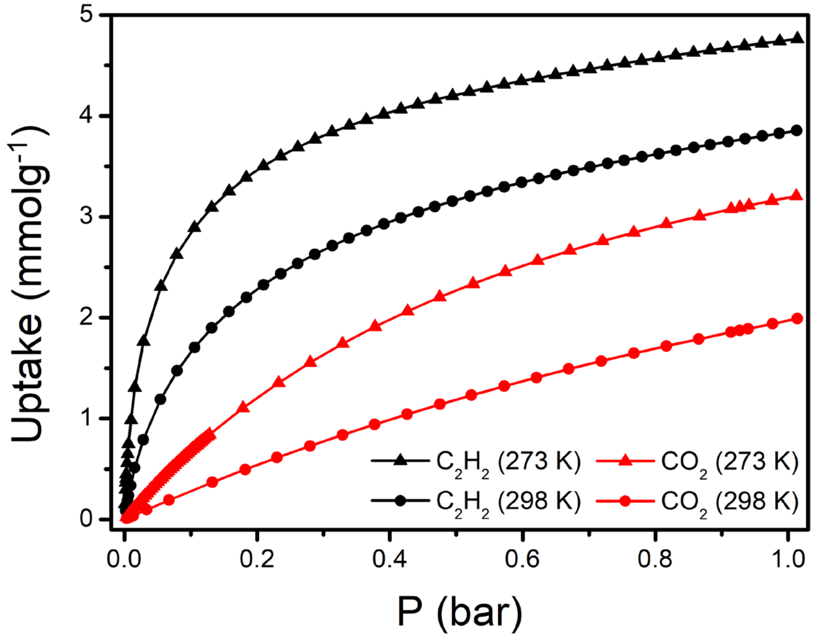

Figure S18. C_2H_2 and CO_2 adsorption isotherms for **TIFSIX-4-Ni**.

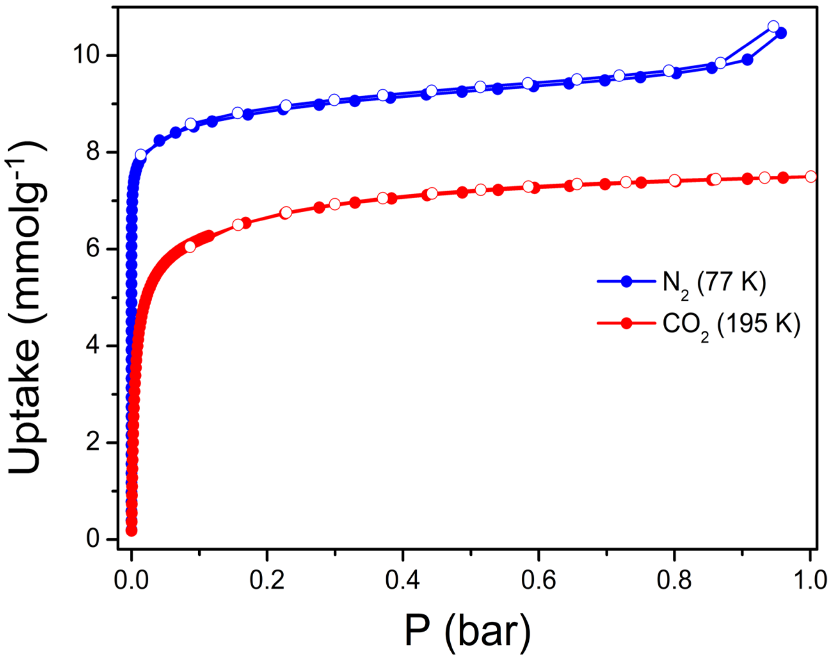

Figure S19. Low temperature CO_2 and N_2 sorption isotherms for **NbOFFIVE-3-Ni** (filled shape: adsorption; hollow shape: desorption) with BET surface areas 761 m^2g^{-1} and 599 m^2g^{-1} determined from N_2 and CO_2 isotherms respectively. Last adsorption data point is an outcome of condensation in inter-particle voids (similar to other physisorbents, such as ZIF-8, microporous silica material, and carbon nitride).[51-54]

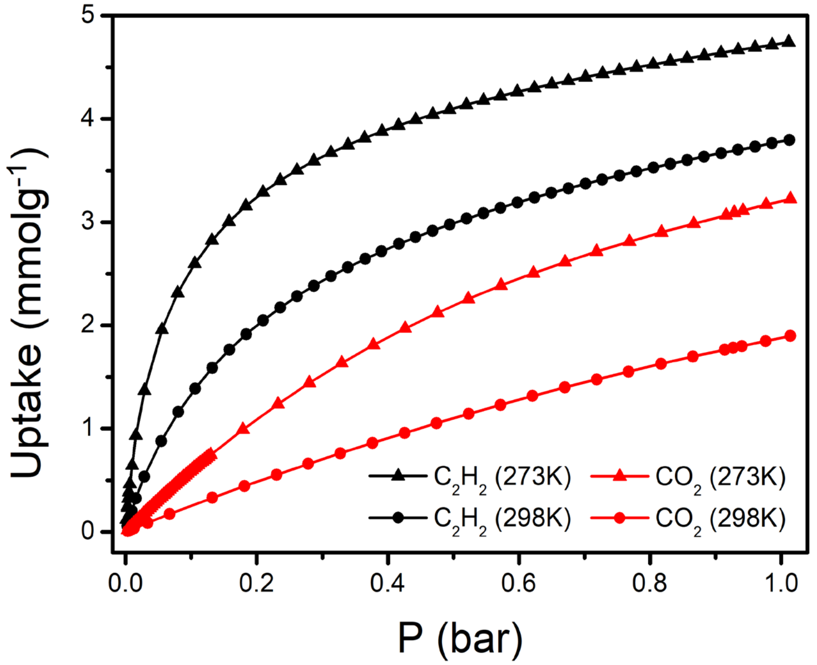

Figure S20. C_2H_2 and CO_2 adsorption isotherms for **NbOFFIVE-3-Ni**.

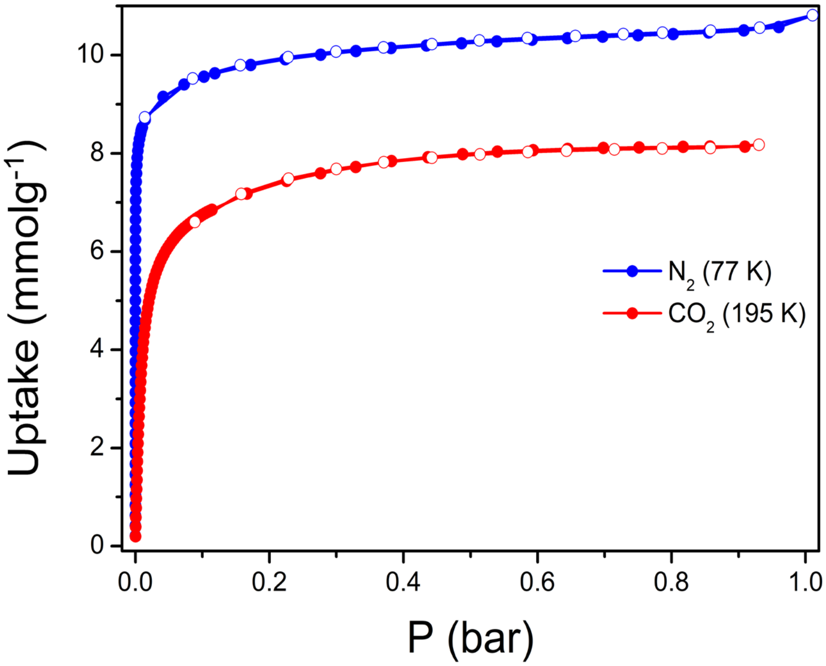

Figure S21. Low temperature CO_2 and N_2 sorption isotherms for **SIFSIX-21-Cu** (filled shape: adsorption; hollow shape: desorption) with BET surface areas 839 m^{2}g^{-1} and 695 m^{2}g^{-1} determined from N_2 and CO_2 isotherms respectively.

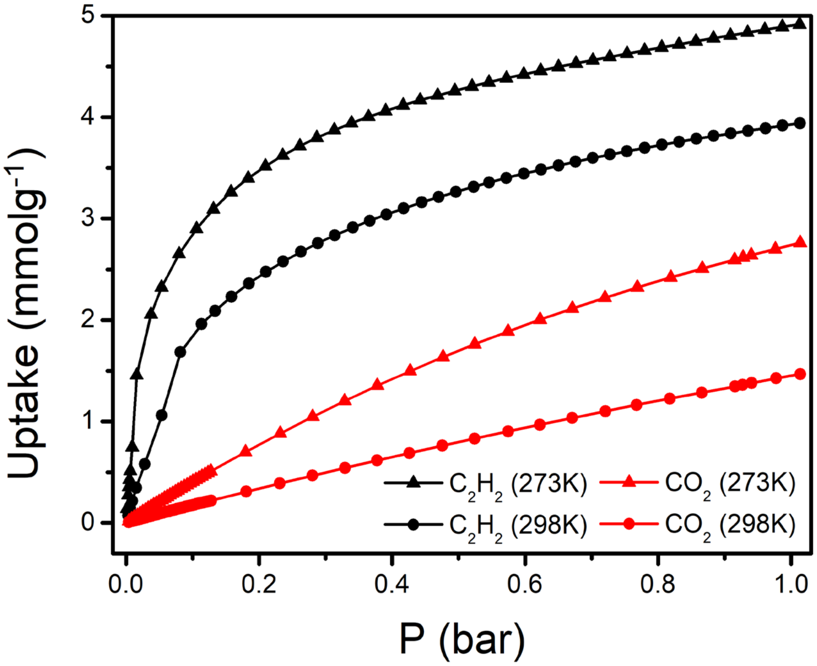

Figure S22. C_2H_2 and CO_2 adsorption isotherms for **SIFSIX-21-Cu**.

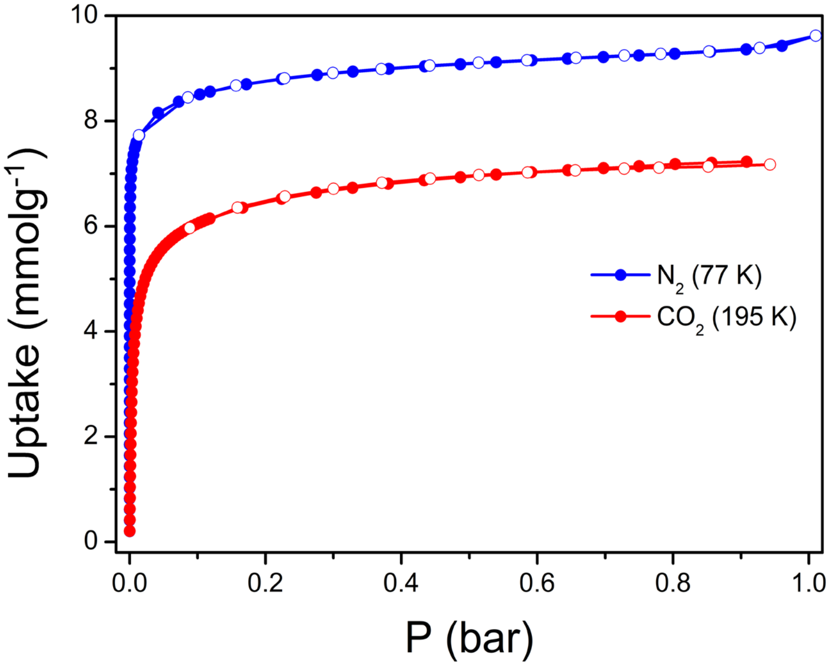

Figure S23. Low temperature CO_2 and N_2 sorption isotherms for **TIFSIX-4-Cu** (filled shape: adsorption; hollow shape: desorption) with BET surface areas 747 m^{2}g^{-1} and 568 m^{2}g^{-1} determined from N_2 and CO_2 isotherms respectively.

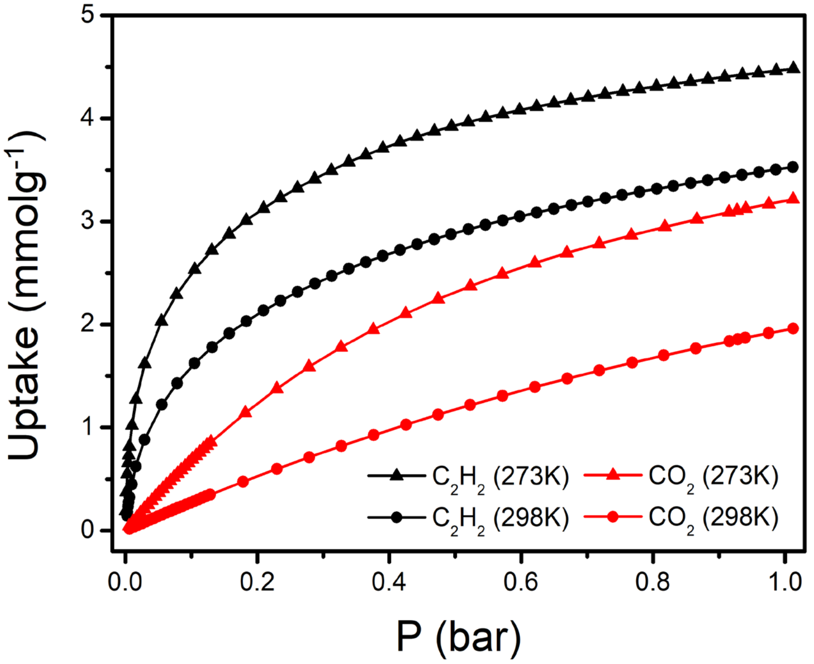

Figure S24. C_2H_2 and CO_2 adsorption isotherms for **TIFSIX-4-Cu**.

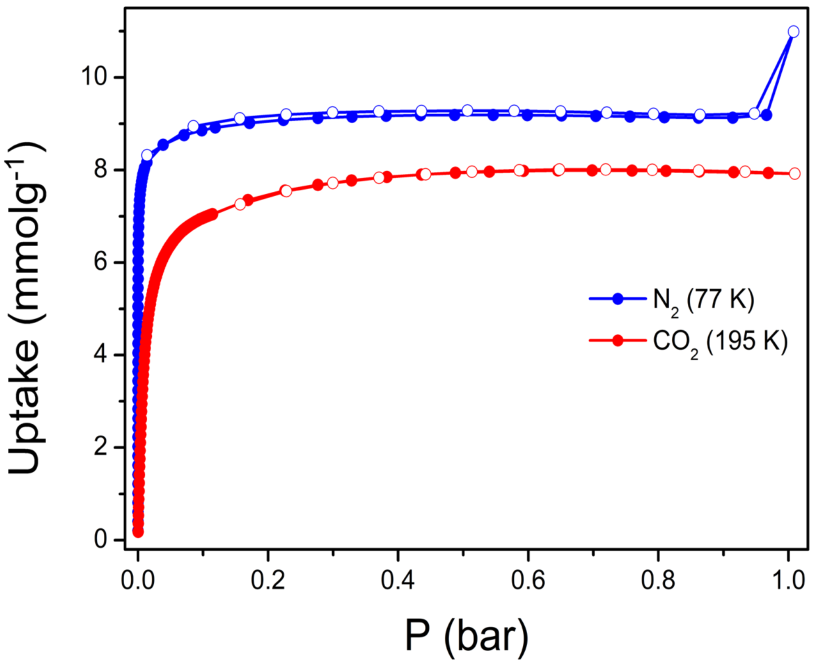

Figure S25. Low temperature CO_2 and N_2 sorption isotherms for **NbOFFIVE-3-Cu** (filled shape: adsorption; hollow shape: desorption) with BET surface areas 805 m^{2}g^{-1} and 722 m^{2}g^{-1} determined from N_2 and CO_2 isotherms respectively Last adsorption data point is an outcome of condensation in inter-particle voids (similar to other physisorbents, such as ZIF-8, microporous silica material, and carbon nitride).[51-54]

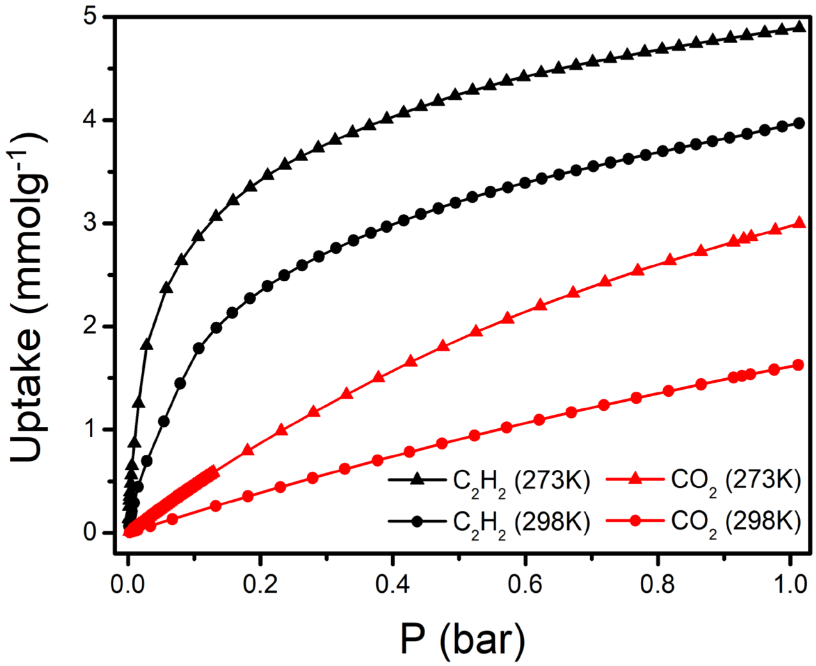

Figure S26. C_2H_2 and CO_2 adsorption isotherms for **NbOFFIVE-3-Cu**.

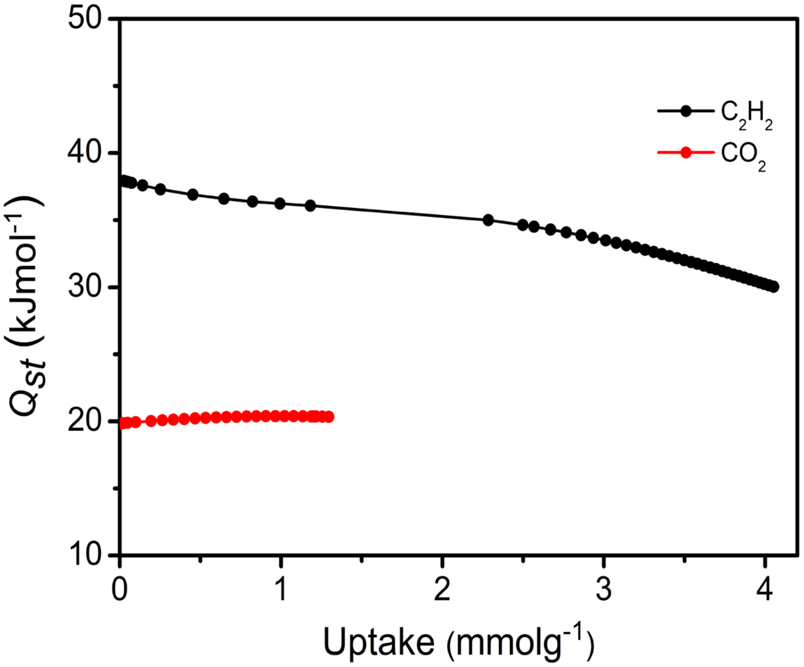

Figure S27. Isosteric enthalpies of adsorption for C_2H_2 and CO_2 for **SIFSIX-21-Ni**.

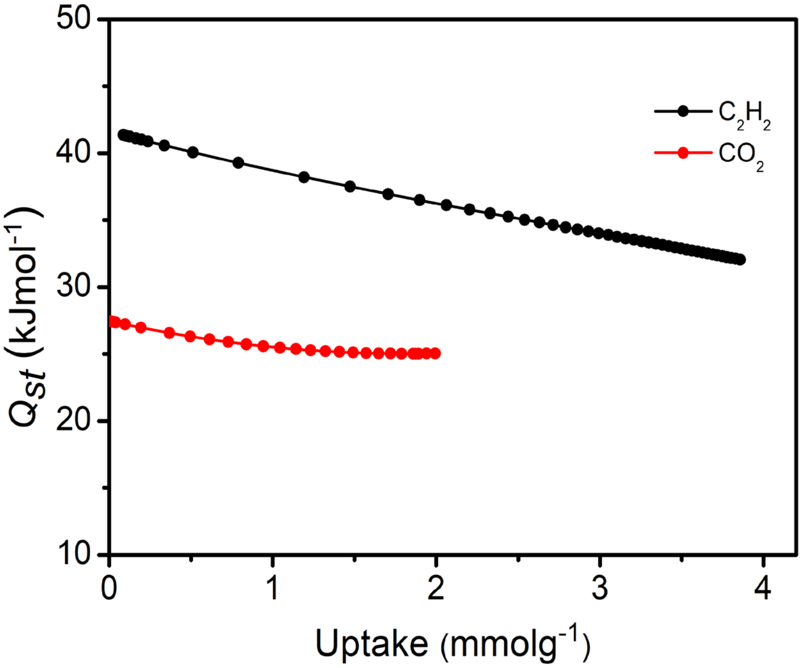

Figure S28. Isosteric enthalpies of adsorption for C_2H_2 and CO_2 for **TIFSIX-4-Ni**.

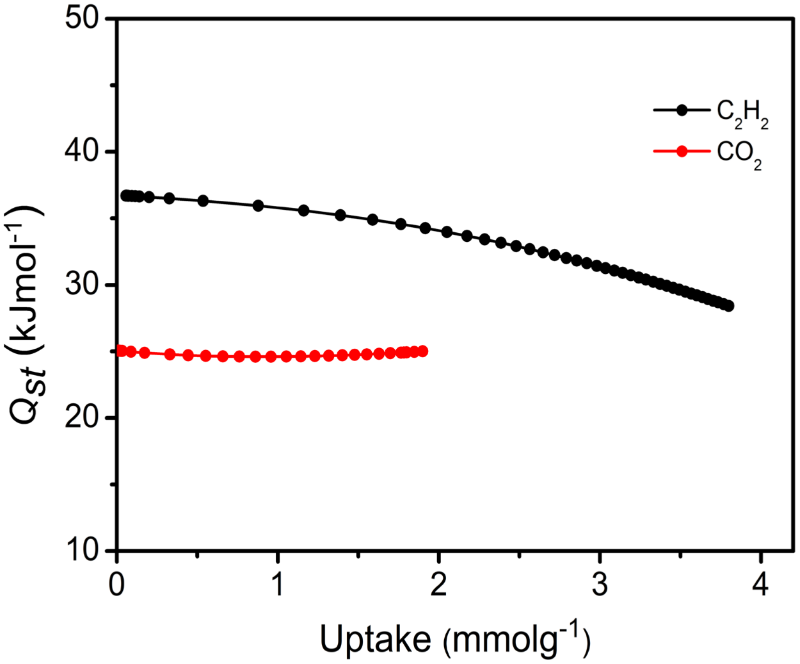

Figure S29. Isosteric enthalpies of adsorption for C_2H_2 and CO_2 for **NbOFFIVE-3-Ni**.

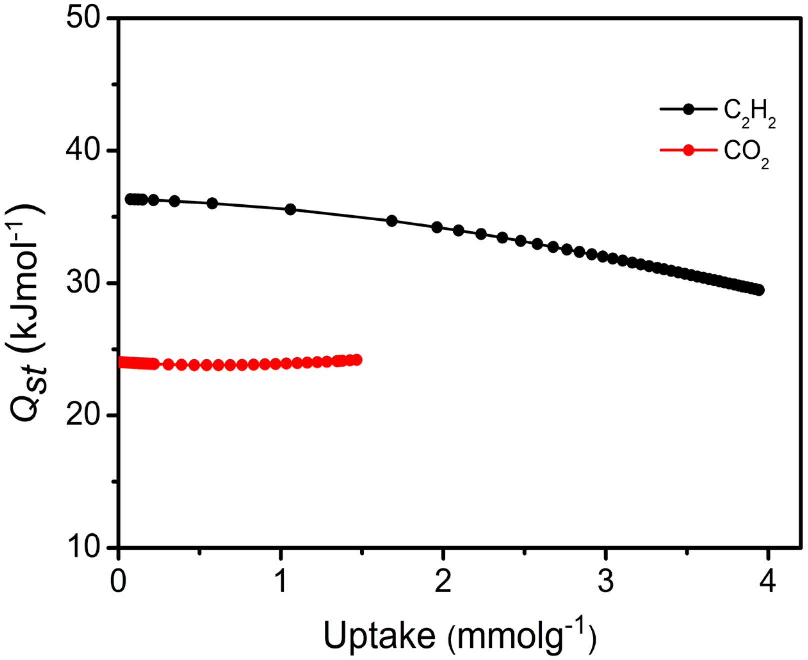

Figure S30. Isosteric enthalpies of adsorption for C_2H_2 and CO_2 for **SIFSIX-21-Cu**.

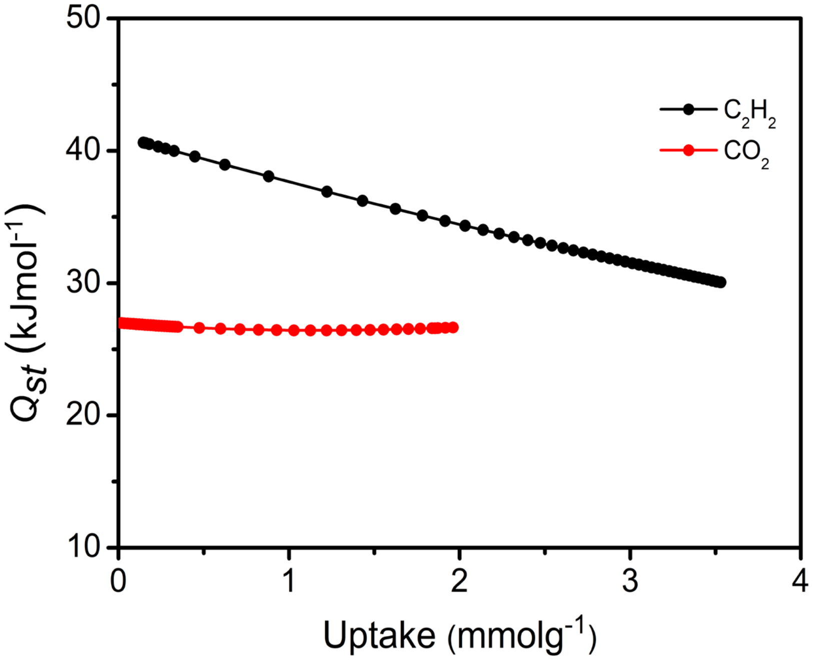

Figure S31. Isosteric enthalpies of adsorption for C_2H_2 and CO_2 for **TIFSIX-4-Cu**.

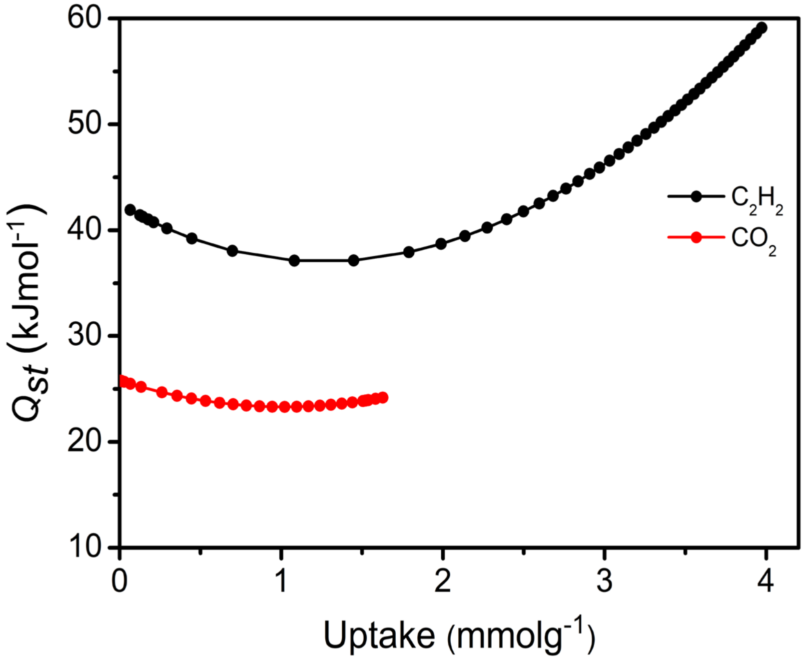

Figure S32. Isosteric enthalpies of adsorption for C_2H_2 and CO_2 for **NbOFFIVE-3-Cu**.

Q$_{st}$ Calculation - Virial Fitting

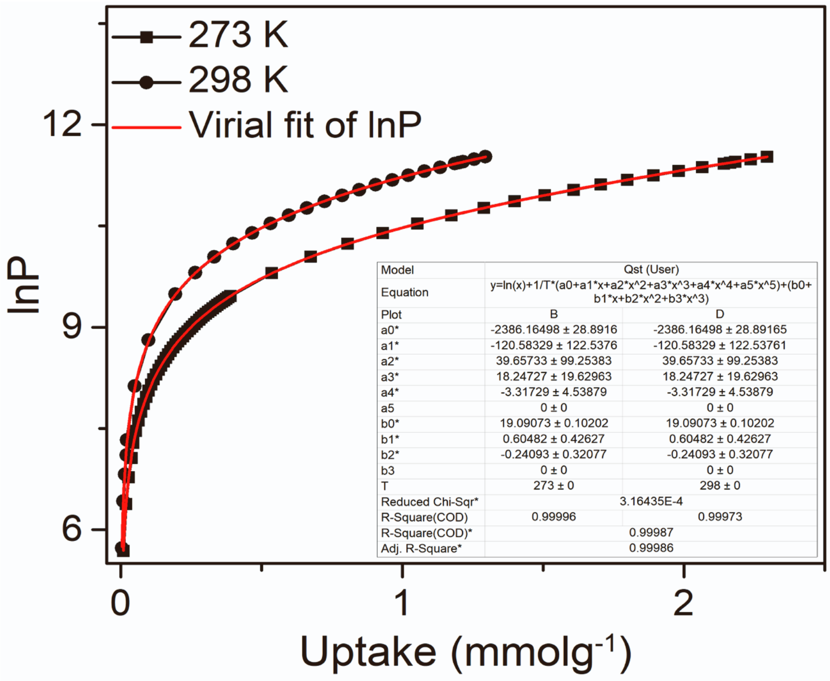

Model	Qst (User)	
Equation	y=ln(x)+1/T*(a0+a1*x+a2*x^2+a3*x^3+a4*x^4+a5*x^5)+(b0+b1*x+b2*x^2+b3*x^3)	
Plot	B	D
a0*	-2386.16498 ± 28.8916	-2386.16498 ± 28.89165
a1*	-120.58329 ± 122.5376	-120.58329 ± 122.53761
a2*	39.65733 ± 99.25383	39.65733 ± 99.25383
a3*	18.24727 ± 19.62963	18.24727 ± 19.62963
a4*	-3.31729 ± 4.53879	-3.31729 ± 4.53879
a5	0 ± 0	0 ± 0
b0*	19.09073 ± 0.10202	19.09073 ± 0.10202
b1*	0.60482 ± 0.42627	0.60482 ± 0.42627
b2*	-0.24093 ± 0.32077	-0.24093 ± 0.32077
b3	0 ± 0	0 ± 0
T	273 ± 0	298 ± 0
Reduced Chi-Sqr*	3.16435E-4	
R-Square(COD)	0.99996	0.99973
R-Square(COD)*	0.99987	
Adj. R-Square*	0.99986	

Figure S33. Fitting of the CO_2 isotherm data for **SIFSIX-21-Ni** to the virial equation.

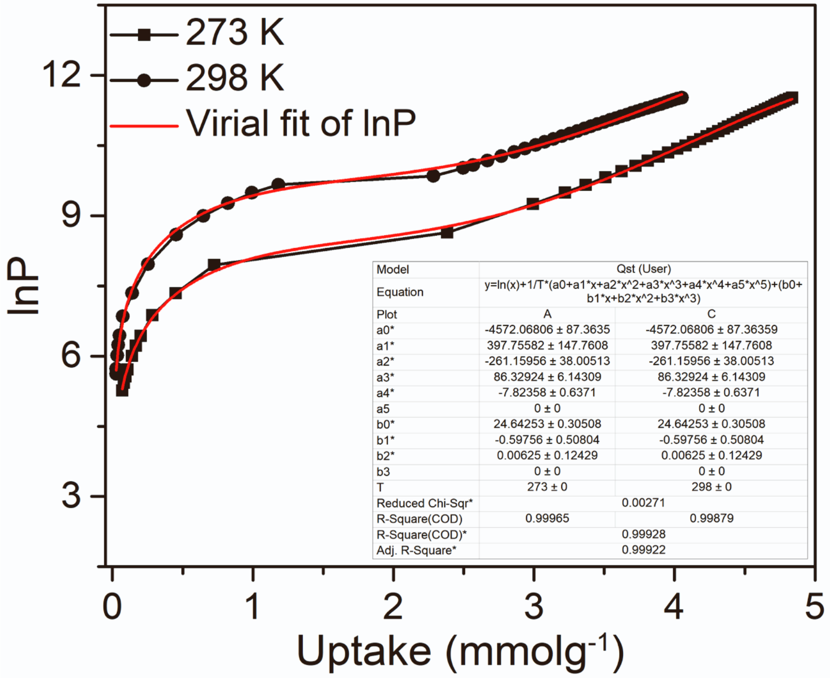

Model	Qst (User)	
Equation	y=ln(x)+1/T*(a0+a1*x+a2*x^2+a3*x^3+a4*x^4+a5*x^5)+(b0+b1*x+b2*x^2+b3*x^3)	
Plot	A	C
a0*	-4572.06806 ± 87.3635	-4572.06806 ± 87.36359
a1*	397.75582 ± 147.7608	397.75582 ± 147.7608
a2*	-261.15956 ± 38.00513	-261.15956 ± 38.00513
a3*	86.32924 ± 6.14309	86.32924 ± 6.14309
a4*	-7.82358 ± 0.6371	-7.82358 ± 0.6371
a5	0 ± 0	0 ± 0
b0*	24.64253 ± 0.30508	24.64253 ± 0.30508
b1*	-0.59756 ± 0.50804	-0.59756 ± 0.50804
b2*	0.00625 ± 0.12429	0.00625 ± 0.12429
b3	0 ± 0	0 ± 0
T	273 ± 0	298 ± 0
Reduced Chi-Sqr*	0.00271	
R-Square(COD)	0.99965	0.99879
R-Square(COD)*	0.99928	
Adj. R-Square*	0.99922	

Figure S34. Fitting of the C_2H_2 isotherm data for **SIFSIX-21-Ni** to the virial equation.

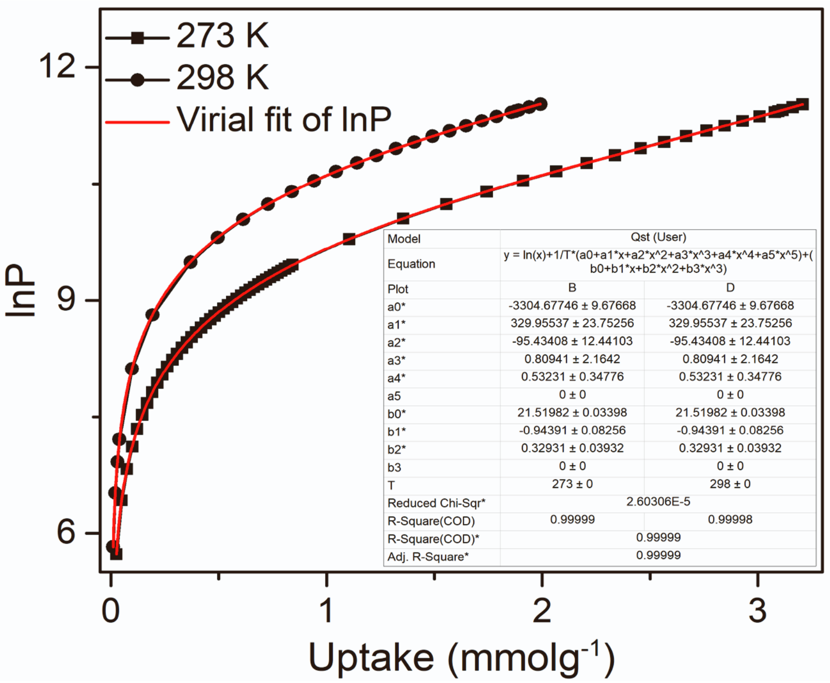

Model	Qst (User)	
Equation	y = ln(x)+1/T*(a0+a1*x+a2*x^2+a3*x^3+a4*x^4+a5*x^5)+(b0+b1*x+b2*x^2+b3*x^3)	
Plot	B	D
a0*	-3304.67746 ± 9.67668	-3304.67746 ± 9.67668
a1*	329.95537 ± 23.75256	329.95537 ± 23.75256
a2*	-95.43408 ± 12.44103	-95.43408 ± 12.44103
a3*	0.80941 ± 2.1642	0.80941 ± 2.1642
a4*	0.53231 ± 0.34776	0.53231 ± 0.34776
a5	0 ± 0	0 ± 0
b0*	21.51982 ± 0.03398	21.51982 ± 0.03398
b1*	-0.94391 ± 0.08256	-0.94391 ± 0.08256
b2*	0.32931 ± 0.03932	0.32931 ± 0.03932
b3	0 ± 0	0 ± 0
T	273 ± 0	298 ± 0
Reduced Chi-Sqr*	2.60306E-5	
R-Square(COD)	0.99999	0.99998
R-Square(COD)*	0.99999	
Adj. R-Square*	0.99999	

Figure S35. Fitting of the CO_2 isotherm data for **TIFSIX-4-Ni** to the virial equation.

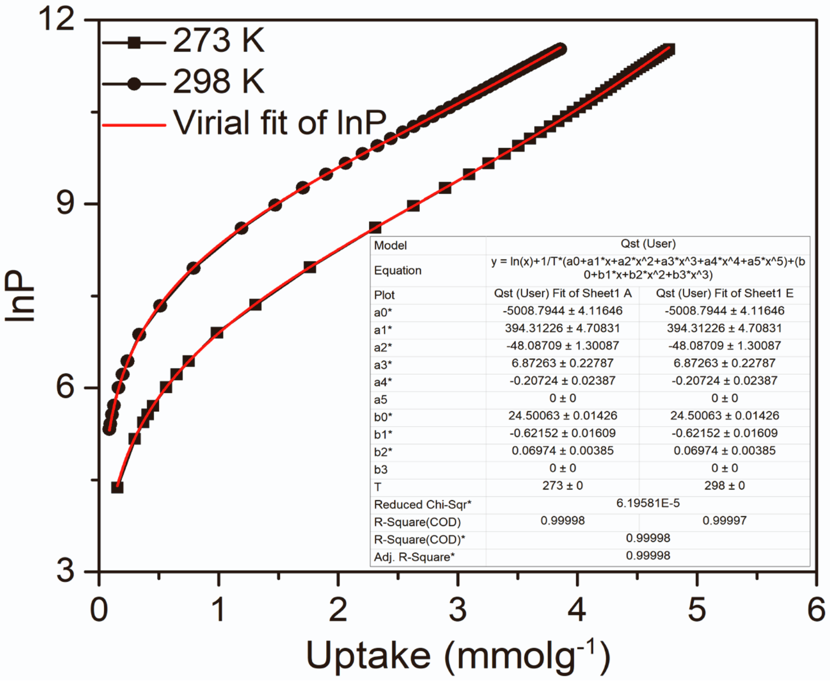

Model	Qst (User)	
Equation	y = ln(x)+1/T*(a0+a1*x+a2*x^2+a3*x^3+a4*x^4+a5*x^5)+(b0+b1*x+b2*x^2+b3*x^3)	
Plot	Qst (User) Fit of Sheet1 A	Qst (User) Fit of Sheet1 E
a0*	-5008.7944 ± 4.11646	-5008.7944 ± 4.11646
a1*	394.31226 ± 4.70831	394.31226 ± 4.70831
a2*	-48.08709 ± 1.30087	-48.08709 ± 1.30087
a3*	6.87263 ± 0.22787	6.87263 ± 0.22787
a4*	-0.20724 ± 0.02387	-0.20724 ± 0.02387
a5	0 ± 0	0 ± 0
b0*	24.50063 ± 0.01426	24.50063 ± 0.01426
b1*	-0.62152 ± 0.01609	-0.62152 ± 0.01609
b2*	0.06974 ± 0.00385	0.06974 ± 0.00385
b3	0 ± 0	0 ± 0
T	273 ± 0	298 ± 0
Reduced Chi-Sqr*	6.19581E-5	
R-Square(COD)	0.99998	0.99997
R-Square(COD)*	0.99998	
Adj. R-Square*	0.99998	

Figure S36. Fitting of the C_2H_2 isotherm data for **TIFSIX-4-Ni** to the virial equation.

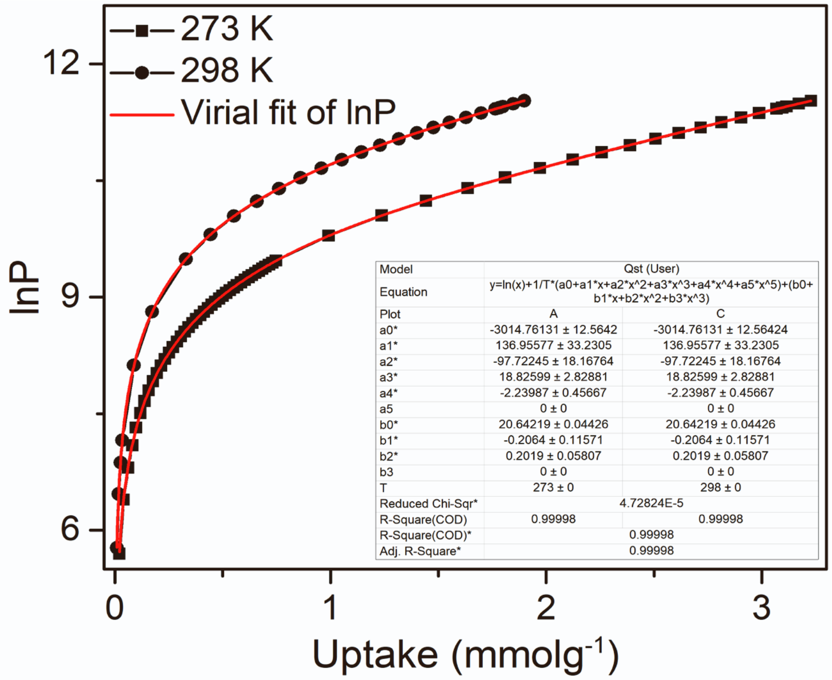

Model	Qst (User)	
Equation	y=ln(x)+1/T*(a0+a1*x+a2*x^2+a3*x^3+a4*x^4+a5*x^5)+(b0+ b1*x+b2*x^2+b3*x^3)	
Plot	A	C
a0*	-3014.76131 ± 12.5642	-3014.76131 ± 12.56424
a1*	136.95577 ± 33.2305	136.95577 ± 33.2305
a2*	-97.72245 ± 18.16764	-97.72245 ± 18.16764
a3*	18.82599 ± 2.82881	18.82599 ± 2.82881
a4*	-2.23987 ± 0.45667	-2.23987 ± 0.45667
a5	0 ± 0	0 ± 0
b0*	20.64219 ± 0.04426	20.64219 ± 0.04426
b1*	-0.2064 ± 0.11571	-0.2064 ± 0.11571
b2*	0.2019 ± 0.05807	0.2019 ± 0.05807
b3	0 ± 0	0 ± 0
T	273 ± 0	298 ± 0
Reduced Chi-Sqr*	4.72824E-5	
R-Square(COD)	0.99998	0.99998
R-Square(COD)*	0.99998	
Adj. R-Square*	0.99998	

Figure S37. Fitting of the CO_2 isotherm data for **NbOFFIVE-3-Ni** to the virial equation.

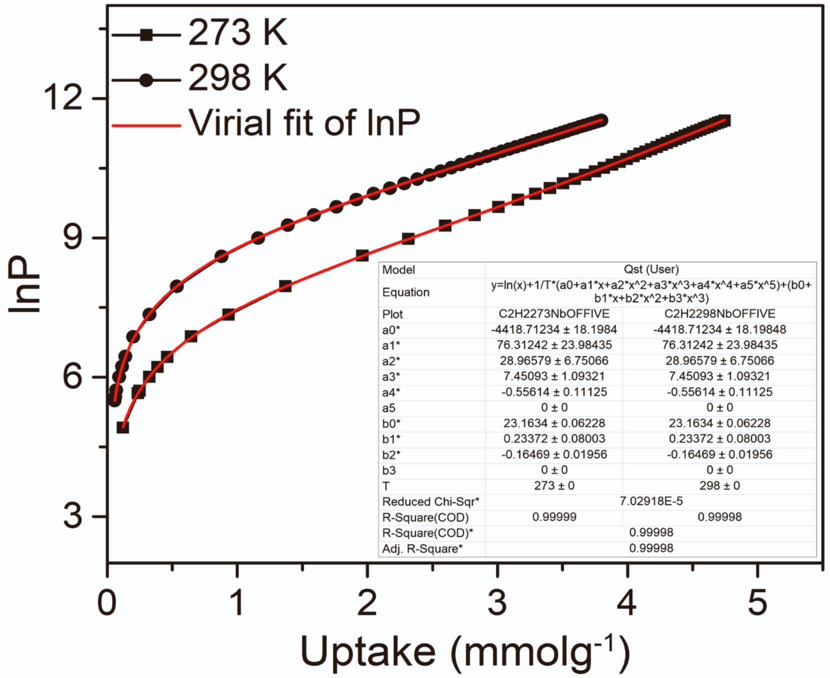

Model	Qst (User)	
Equation	y=ln(x)+1/T*(a0+a1*x+a2*x^2+a3*x^3+a4*x^4+a5*x^5)+(b0+ b1*x+b2*x^2+b3*x^3)	
Plot	C2H2273NbOFFIVE	C2H2298NbOFFIVE
a0*	-4418.71234 ± 18.1984	-4418.71234 ± 18.19848
a1*	76.31242 ± 23.98435	76.31242 ± 23.98435
a2*	28.96579 ± 6.75066	28.96579 ± 6.75066
a3*	7.45093 ± 1.09321	7.45093 ± 1.09321
a4*	-0.55614 ± 0.11125	-0.55614 ± 0.11125
a5	0 ± 0	0 ± 0
b0*	23.1634 ± 0.06228	23.1634 ± 0.06228
b1*	0.23372 ± 0.08003	0.23372 ± 0.08003
b2*	-0.16469 ± 0.01956	-0.16469 ± 0.01956
b3	0 ± 0	0 ± 0
T	273 ± 0	298 ± 0
Reduced Chi-Sqr*	7.02918E-5	
R-Square(COD)	0.99999	0.99998
R-Square(COD)*	0.99998	
Adj. R-Square*	0.99998	

Figure S38. Fitting of the C_2H_2 isotherm data for **NbOFFIVE-3-Ni** to the virial equation.

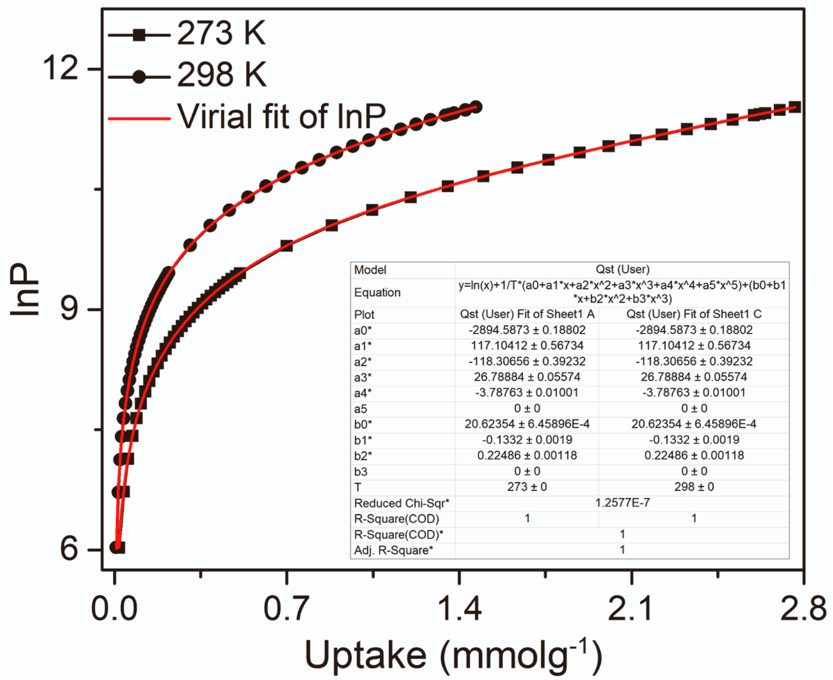

Model	Qst (User)	
Equation	y=ln(x)+1/T*(a0+a1*x+a2*x^2+a3*x^3+a4*x^4+a5*x^5)+(b0+b1*x+b2*x^2+b3*x^3)	
Plot	Qst (User) Fit of Sheet1 A	Qst (User) Fit of Sheet1 C
a0*	-2894.5873 ± 0.18802	-2894.5873 ± 0.18802
a1*	117.10412 ± 0.56734	117.10412 ± 0.56734
a2*	-118.30656 ± 0.39232	-118.30656 ± 0.39232
a3*	26.78884 ± 0.05574	26.78884 ± 0.05574
a4*	-3.78763 ± 0.01001	-3.78763 ± 0.01001
a5	0 ± 0	0 ± 0
b0*	20.62354 ± 6.45896E-4	20.62354 ± 6.45896E-4
b1*	-0.1332 ± 0.0019	-0.1332 ± 0.0019
b2*	0.22486 ± 0.00118	0.22486 ± 0.00118
b3	0 ± 0	0 ± 0
T	273 ± 0	298 ± 0
Reduced Chi-Sqr*	1.2577E-7	
R-Square(COD)	1	1
R-Square(COD)*	1	
Adj. R-Square*	1	

Figure S39. Fitting of the CO_2 isotherm data for **SIFSIX-21-Cu** to the virial equation.

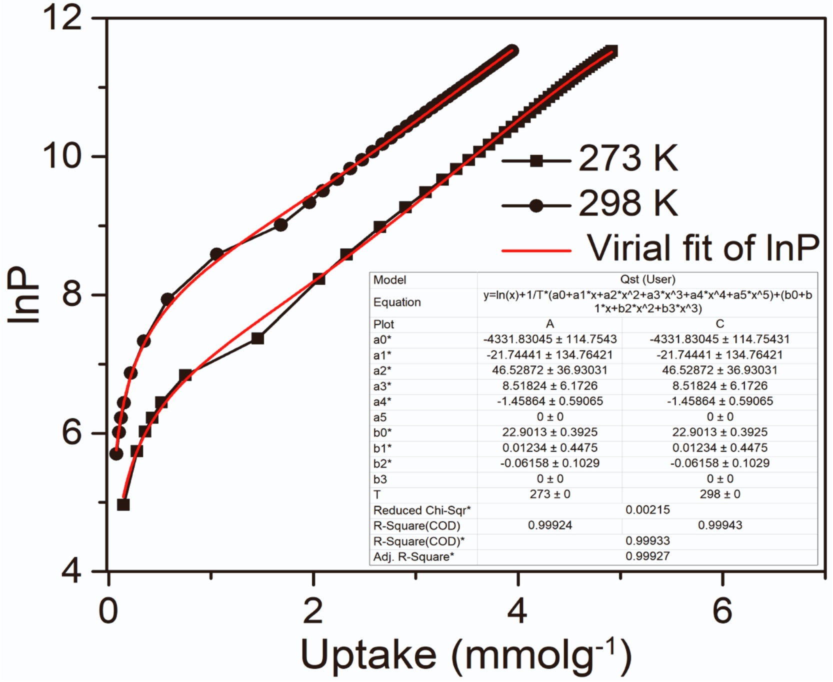

Model	Qst (User)	
Equation	y=ln(x)+1/T*(a0+a1*x+a2*x^2+a3*x^3+a4*x^4+a5*x^5)+(b0+b1*x+b2*x^2+b3*x^3)	
Plot	A	C
a0*	-4331.83045 ± 114.7543	-4331.83045 ± 114.75431
a1*	-21.74441 ± 134.76421	-21.74441 ± 134.76421
a2*	46.52872 ± 36.93031	46.52872 ± 36.93031
a3*	8.51824 ± 6.1726	8.51824 ± 6.1726
a4*	-1.45864 ± 0.59065	-1.45864 ± 0.59065
a5	0 ± 0	0 ± 0
b0*	22.9013 ± 0.3925	22.9013 ± 0.3925
b1*	0.01234 ± 0.4475	0.01234 ± 0.4475
b2*	-0.06158 ± 0.1029	-0.06158 ± 0.1029
b3	0 ± 0	0 ± 0
T	273 ± 0	298 ± 0
Reduced Chi-Sqr*	0.00215	
R-Square(COD)	0.99924	0.99943
R-Square(COD)*	0.99933	
Adj. R-Square*	0.99927	

Figure S40. Fitting of the C_2H_2 isotherm data for **SIFSIX-21-Cu** to the virial equation.

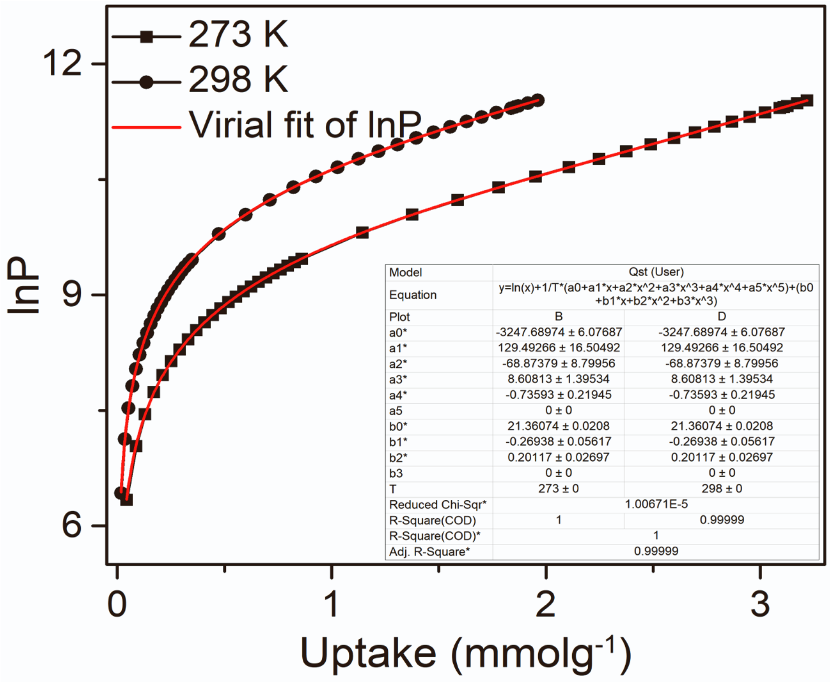

Model	Qst (User)	
Equation	y=ln(x)+1/T*(a0+a1*x+a2*x^2+a3*x^3+a4*x^4+a5*x^5)+(b0+b1*x+b2*x^2+b3*x^3)	
Plot	B	D
a0*	-3247.68974 ± 6.07687	-3247.68974 ± 6.07687
a1*	129.49266 ± 16.50492	129.49266 ± 16.50492
a2*	-68.87379 ± 8.79956	-68.87379 ± 8.79956
a3*	8.60813 ± 1.39534	8.60813 ± 1.39534
a4*	-0.73593 ± 0.21945	-0.73593 ± 0.21945
a5	0 ± 0	0 ± 0
b0*	21.36074 ± 0.0208	21.36074 ± 0.0208
b1*	-0.26938 ± 0.05617	-0.26938 ± 0.05617
b2*	0.20117 ± 0.02697	0.20117 ± 0.02697
b3	0 ± 0	0 ± 0
T	273 ± 0	298 ± 0
Reduced Chi-Sqr*	1.00671E-5	
R-Square(COD)	1	0.99999
R-Square(COD)*	1	
Adj. R-Square*	0.99999	

Figure S41. Fitting of the CO_2 isotherm data for **TIFSIX-4-Cu** to the virial equation.

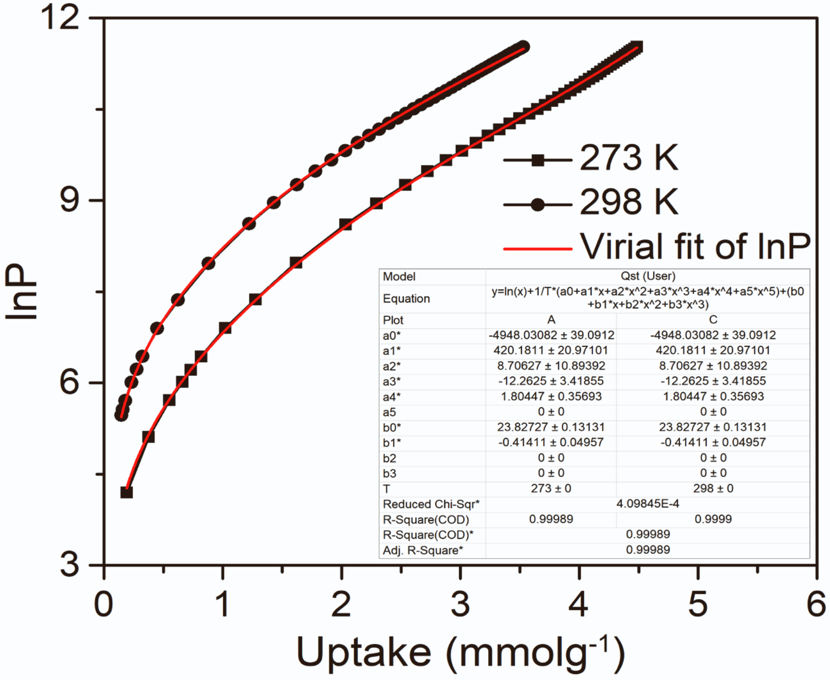

Model	Qst (User)	
Equation	y=ln(x)+1/T*(a0+a1*x+a2*x^2+a3*x^3+a4*x^4+a5*x^5)+(b0+b1*x+b2*x^2+b3*x^3)	
Plot	A	C
a0*	-4948.03082 ± 39.0912	-4948.03082 ± 39.0912
a1*	420.1811 ± 20.97101	420.1811 ± 20.97101
a2*	8.70627 ± 10.89392	8.70627 ± 10.89392
a3*	-12.2625 ± 3.41855	-12.2625 ± 3.41855
a4*	1.80447 ± 0.35693	1.80447 ± 0.35693
a5	0 ± 0	0 ± 0
b0*	23.82727 ± 0.13131	23.82727 ± 0.13131
b1*	-0.41411 ± 0.04957	-0.41411 ± 0.04957
b2	0 ± 0	0 ± 0
b3	0 ± 0	0 ± 0
T	273 ± 0	298 ± 0
Reduced Chi-Sqr*	4.09845E-4	
R-Square(COD)	0.99989	0.9999
R-Square(COD)*	0.99989	
Adj. R-Square*	0.99989	

Figure S42. Fitting of the C_2H_2 isotherm data for **TIFSIX-4-Cu** to the virial equation.

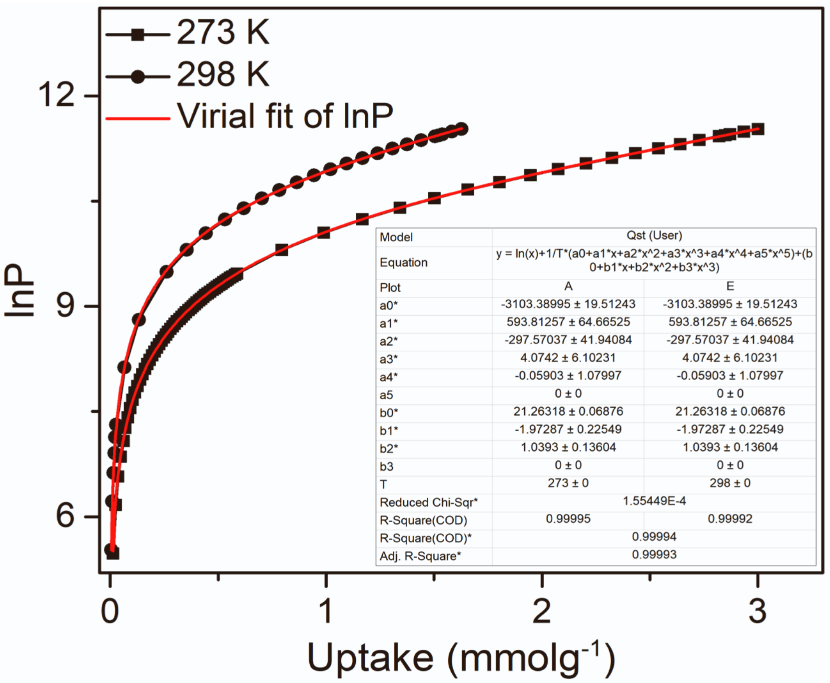

Model	Qst (User)	
Equation	y = ln(x)+1/T*(a0+a1*x+a2*x^2+a3*x^3+a4*x^4+a5*x^5)+(b0+b1*x+b2*x^2+b3*x^3)	
Plot	A	E
a0*	-3103.38995 ± 19.51243	-3103.38995 ± 19.51243
a1*	593.81257 ± 64.66525	593.81257 ± 64.66525
a2*	-297.57037 ± 41.94084	-297.57037 ± 41.94084
a3*	4.0742 ± 6.10231	4.0742 ± 6.10231
a4*	-0.05903 ± 1.07997	-0.05903 ± 1.07997
a5	0 ± 0	0 ± 0
b0*	21.26318 ± 0.06876	21.26318 ± 0.06876
b1*	-1.97287 ± 0.22549	-1.97287 ± 0.22549
b2*	1.0393 ± 0.13604	1.0393 ± 0.13604
b3	0 ± 0	0 ± 0
T	273 ± 0	298 ± 0
Reduced Chi-Sqr*	1.55449E-4	
R-Square(COD)	0.99995	0.99992
R-Square(COD)*	0.99994	
Adj. R-Square*	0.99993	

Figure S43. Fitting of the CO_2 isotherm data for **NbOFFIVE-3-Cu** to the virial equation.

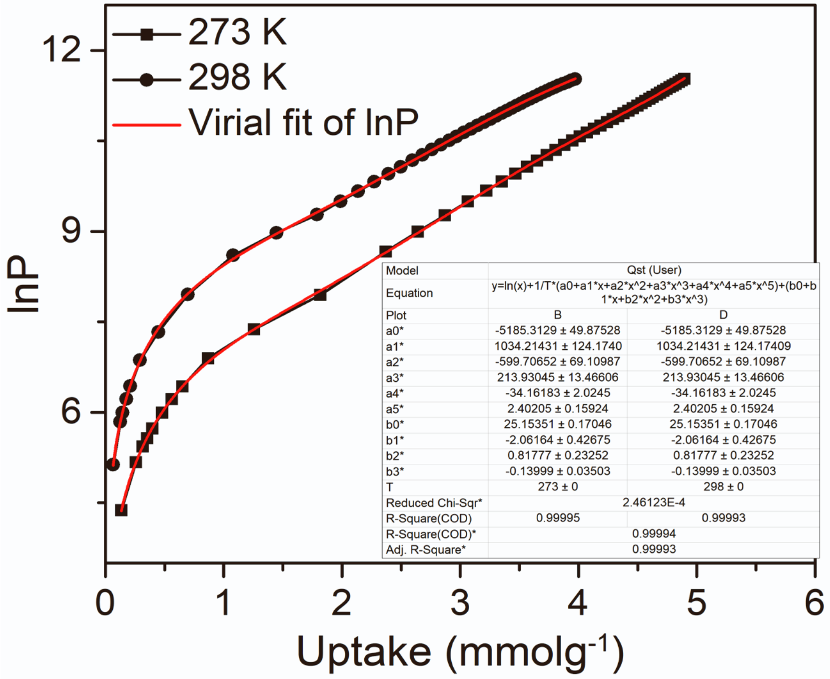

Model	Qst (User)	
Equation	y=ln(x)+1/T*(a0+a1*x+a2*x^2+a3*x^3+a4*x^4+a5*x^5)+(b0+b1*x+b2*x^2+b3*x^3)	
Plot	B	D
a0*	-5185.3129 ± 49.87528	-5185.3129 ± 49.87528
a1*	1034.21431 ± 124.1740	1034.21431 ± 124.17409
a2*	-599.70652 ± 69.10987	-599.70652 ± 69.10987
a3*	213.93045 ± 13.46606	213.93045 ± 13.46606
a4*	-34.16183 ± 2.0245	-34.16183 ± 2.0245
a5*	2.40205 ± 0.15924	2.40205 ± 0.15924
b0*	25.15351 ± 0.17046	25.15351 ± 0.17046
b1*	-2.06164 ± 0.42675	-2.06164 ± 0.42675
b2*	0.81777 ± 0.23252	0.81777 ± 0.23252
b3*	-0.13999 ± 0.03503	-0.13999 ± 0.03503
T	273 ± 0	298 ± 0
Reduced Chi-Sqr*	2.46123E-4	
R-Square(COD)	0.99995	0.99993
R-Square(COD)*	0.99994	
Adj. R-Square*	0.99993	

Figure S44. Fitting of the C_2H_2 isotherm data for **NbOFFIVE-3-Cu** to the virial equation.

IAST(S_{AC}) data.

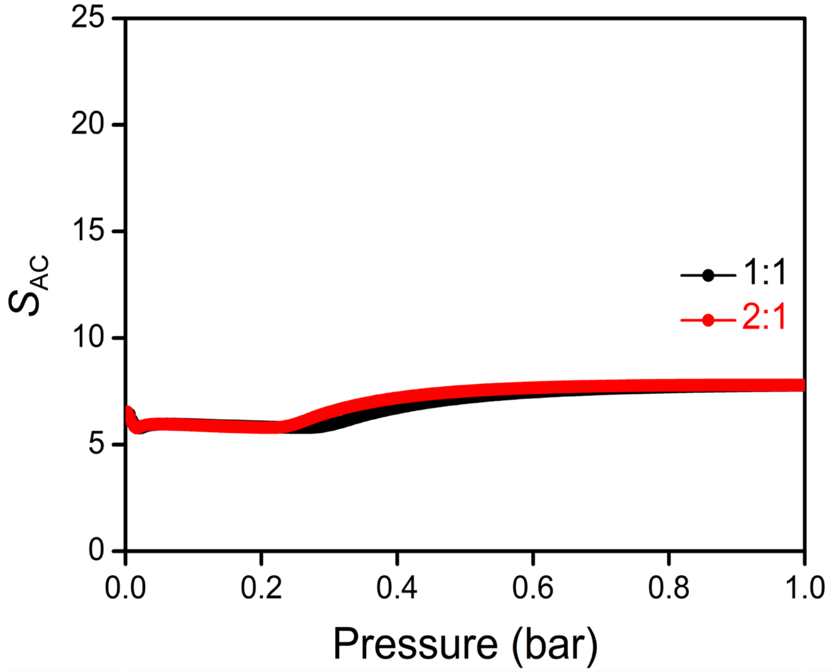

Figure S45. Selectivity for C_2H_2 and CO_2, S_{AC} (1:1 and 2:1 gas mixtures) to 1 bar and 298 K, as calculated by IAST for **SIFSIX-21-Ni**.

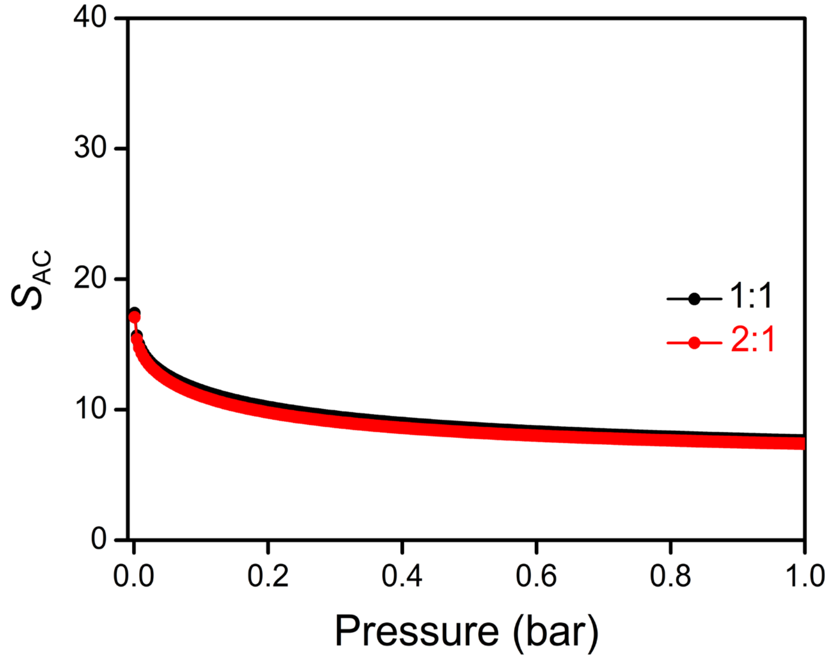

Figure S46. Selectivity for C_2H_2 and CO_2, S_{AC} (1:1 and 2:1 gas mixtures) to 1 bar and 298 K, as calculated by IAST for **TIFSIX-4-Ni**.

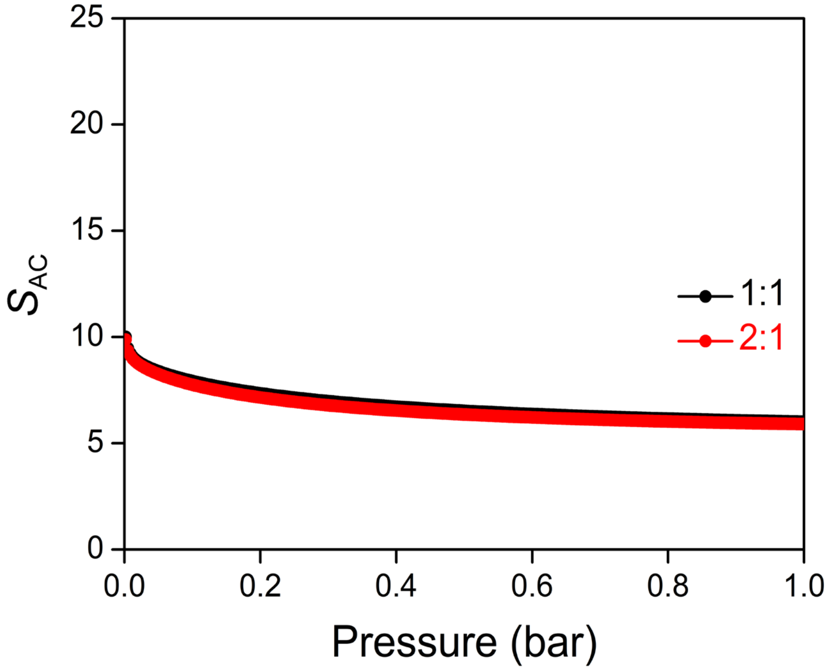

Figure S47. Selectivity for C_2H_2 and CO_2, S_{AC} (1:1 and 2:1 gas mixtures) to 1 bar and 298 K, as calculated by IAST for **NbOFFIVE-3-Ni**.

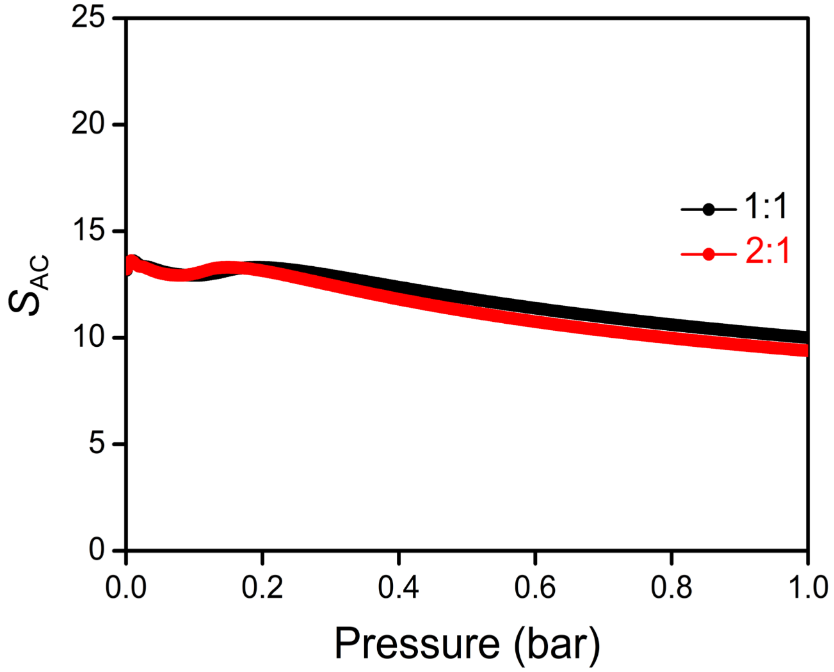

Figure S48. Selectivity for C_2H_2 and CO_2, S_{AC} (1:1 and 2:1 gas mixtures) to 1 bar and 298 K, as calculated by IAST for **SIFSIX-21-Cu**.

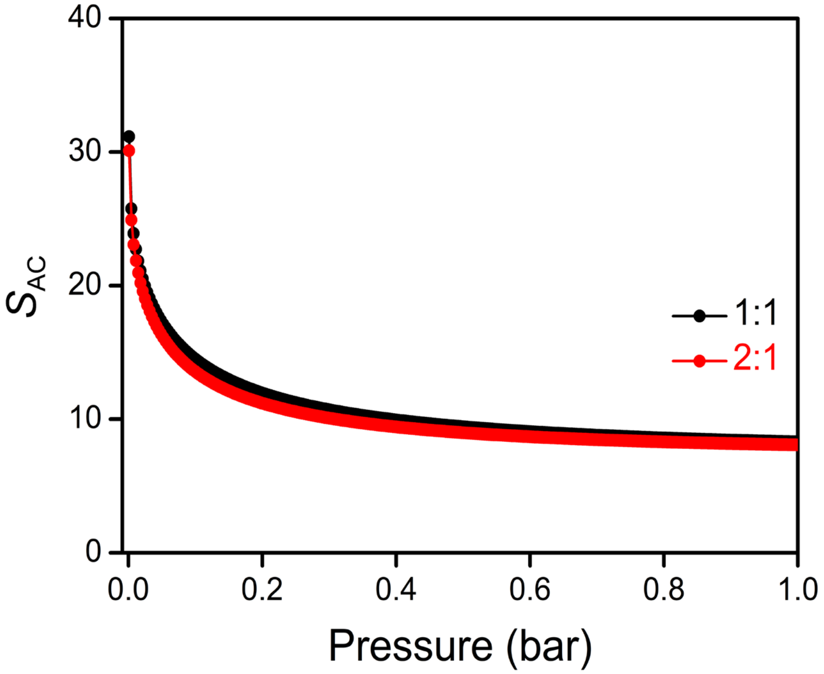

Figure S49. Selectivity for C_2H_2 and CO_2, S_{AC} (1:1 and 2:1 gas mixtures) to 1 bar and 298 K, as calculated by IAST for **TIFSIX-4-Cu**.

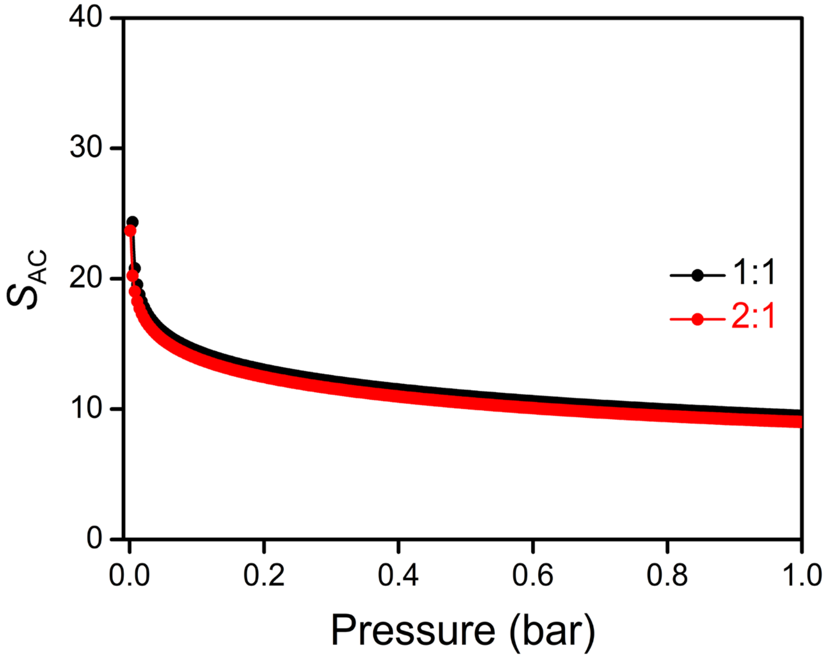

Figure S50. Selectivity for C_2H_2 and CO_2, S_{AC} (1:1 and 2:1 gas mixtures) to 1 bar and 298 K, as calculated by IAST for **NbOFFIVE-3-Cu**.

Mixed isotherms.

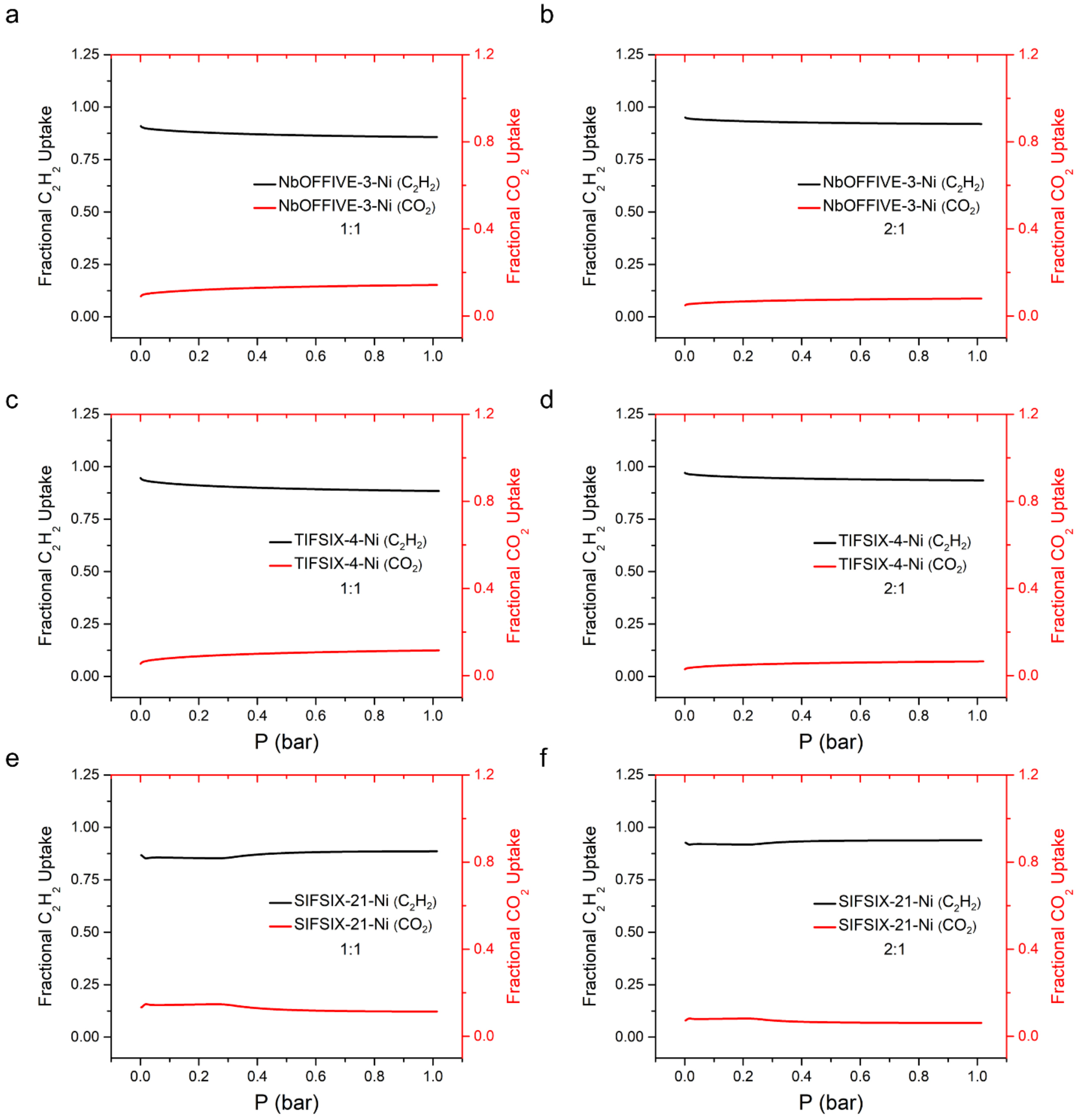

Figure S51. IAST calculations for C_2H_2 and CO_2 uptake capacities for equimolar(1:1) and 2:1 C_2H_2/CO_2 mixtures (X-axis refers to the total gas phase pressure in bar and Y-axis refers to fractional loading of the gases) at 298 K, for (a, b) **NbOFFIVE-3-Ni**, (c, d) **TIFSIX-4-Ni** and (e, f) **SIFSIX-21-Ni**.

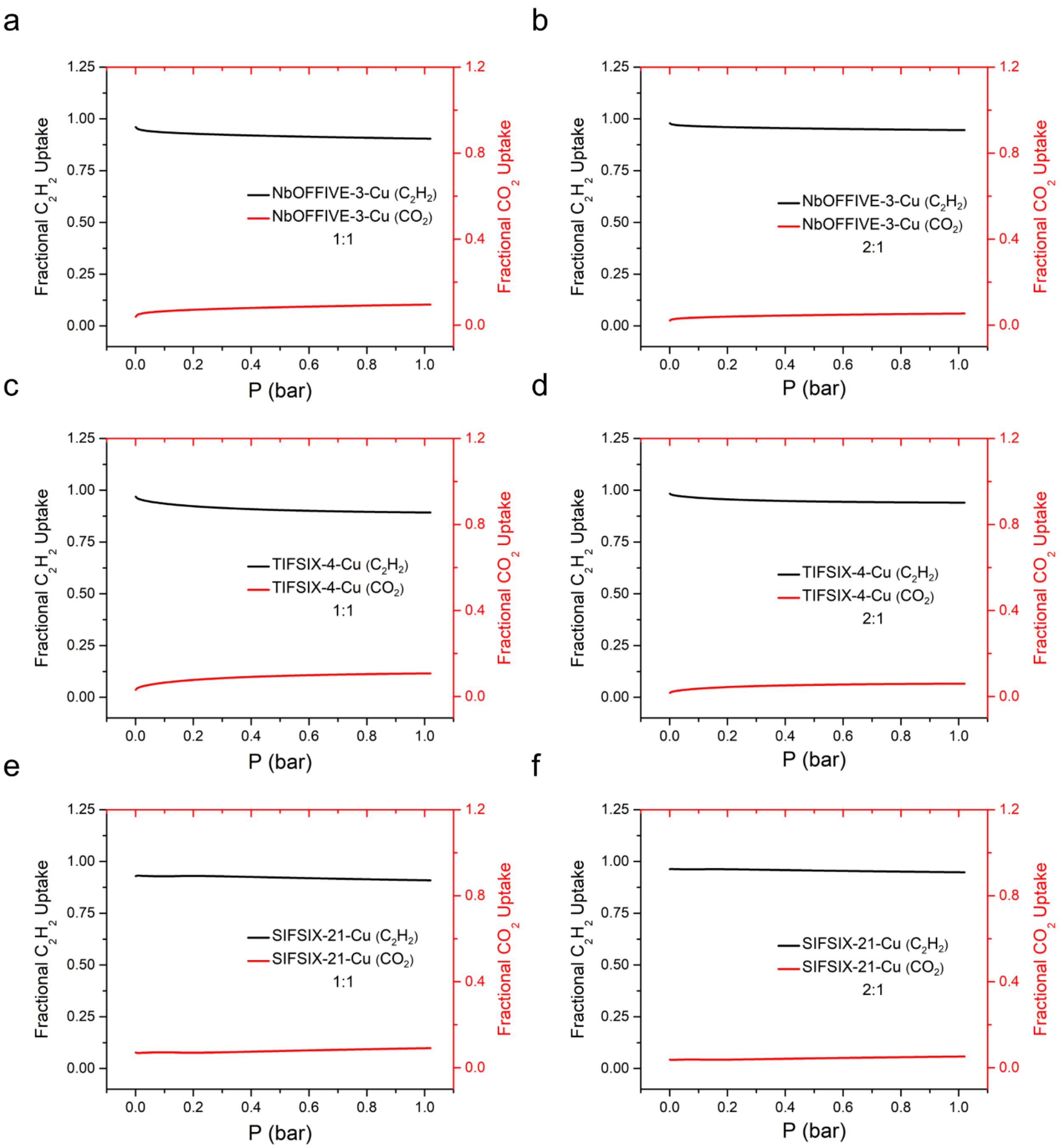

Figure S52. IAST calculations for C_2H_2 and CO_2 uptake capacities for equimolar (v/v = 1:1) and 2:1 (v/v) C_2H_2/CO_2 mixtures (X-axis refers to the total gas phase pressure in bar and Y-axis refers to fractional loading of the gases) at 298 K, for (a, b) **NbOFFIVE-3-Cu**, (c, d) **TIFSIX-4-Cu** and (e, f) **SIFSIX-21-Cu**.

Binding sites.

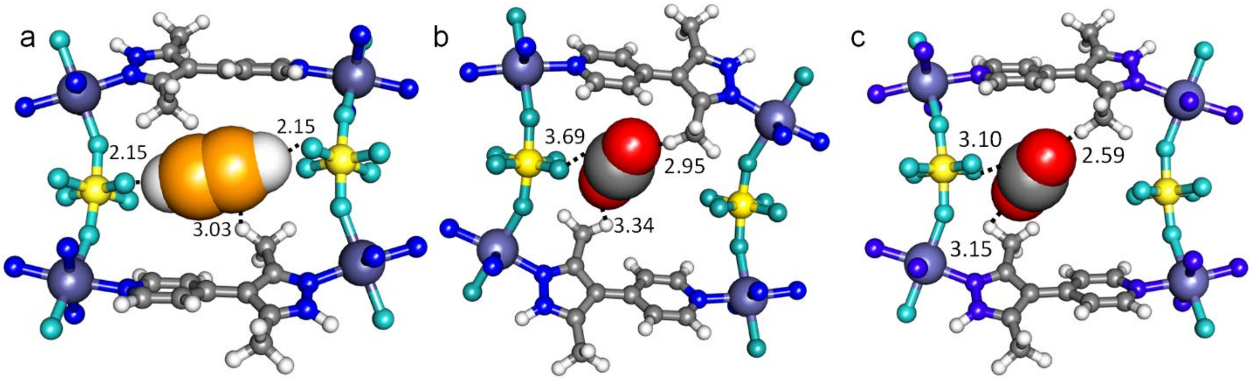

Figure S53. Plausible binding sites for **SIFSIX-21-Ni**, for C_2H_2 (a) and (b, c) CO_2.

Kinetic studies

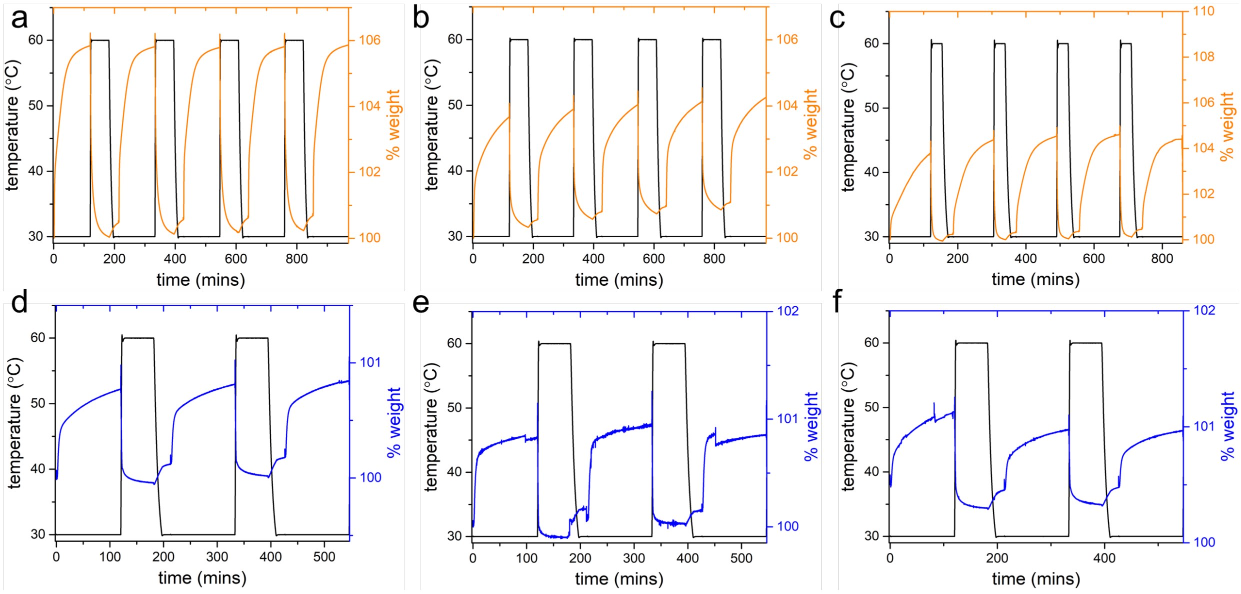

Figure S54. C_2H_2 kinetic plots for a) **SIFSIX-21-Ni**, b) **TIFSIX-4-Ni** and c) **NbOFFIVE-3-Ni**; CO_2 kinetic plots for d) **SIFSIX-21-Ni**, e) **TIFSIX-4-Ni** and f) **NbOFFIVE-3-Ni**.

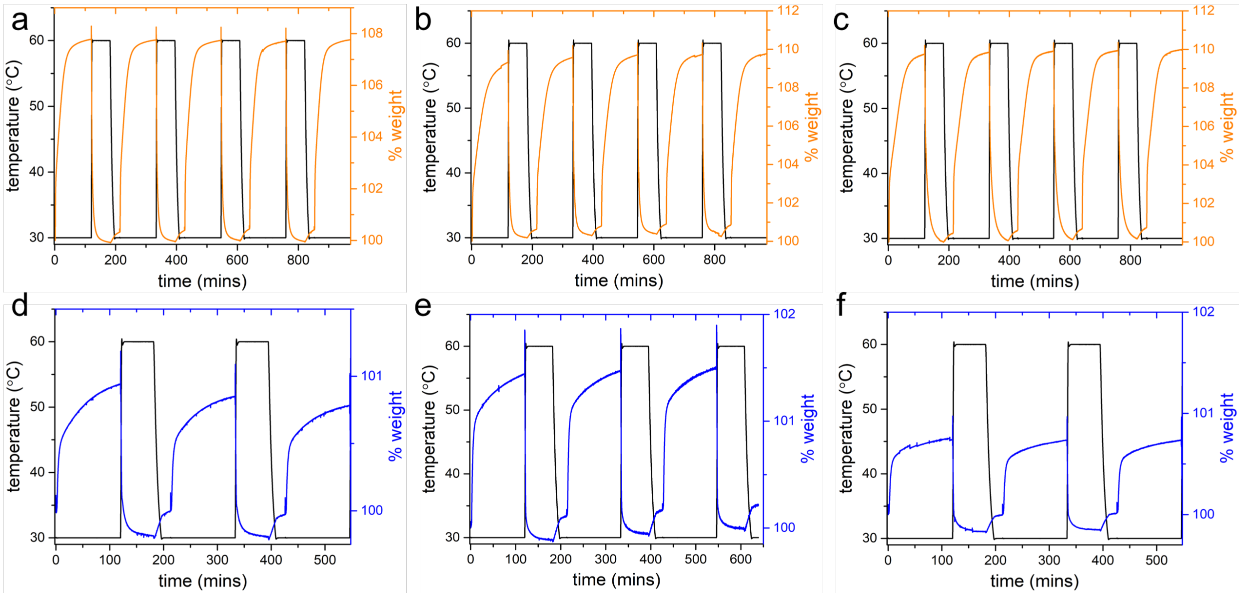

Figure S55. C_2H_2 kinetic plots for a) **SIFSIX-21-Cu**, b) **TIFSIX-4-Cu** and c) **NbOFFIVE-3-Cu**; CO_2 kinetic plots for d) **SIFSIX-21-Cu**, e) **TIFSIX-4-Cu** and f) **NbOFFIVE-3-Cu**.

Dynamic gas breakthrough separation experimental setup.

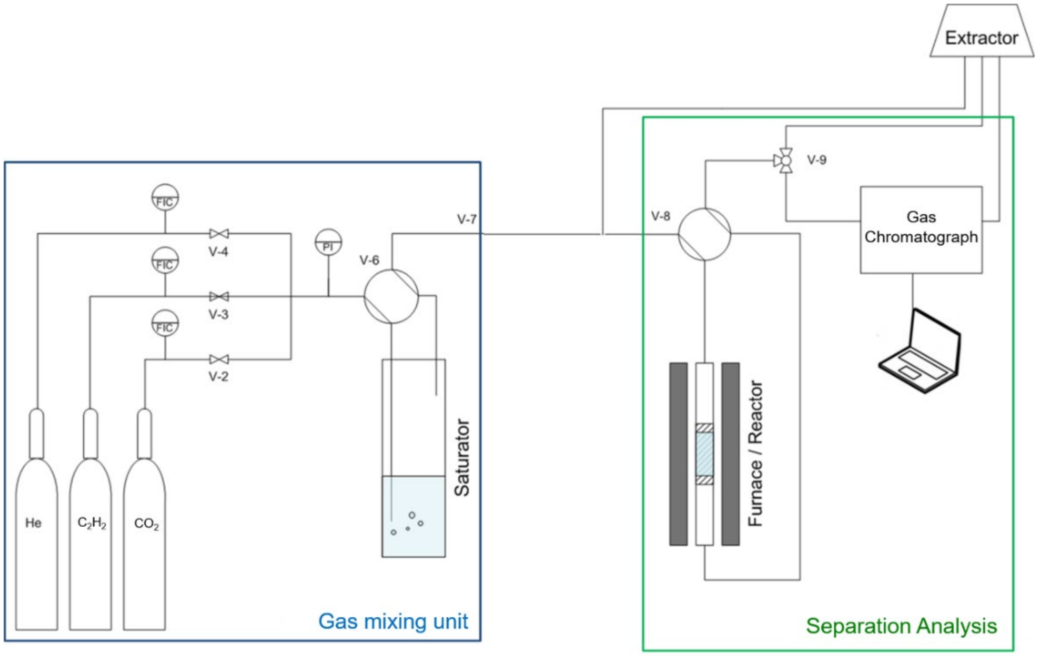

Figure S56. Schematic of gas mixing unit, gravimetric gas uptake analyser and gas separation analyser for breakthrough experiments.

Temperature programmed desorption.

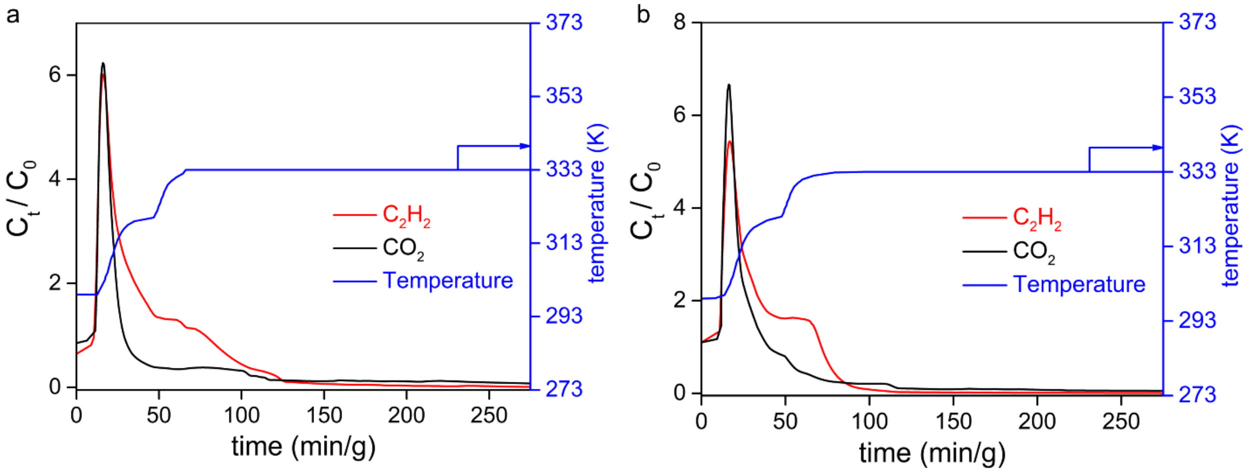

Figure S57. Temperature programmed desorption experiments conducted on a) **SIFSIX-21-Ni**; b) **NbOFFIVE-3-Cu** packed beds. Desorption temperature was set at 60 °C (set along the blue profile) and the He flow was maintained at 20 cm^3 min^{-1}.

$Q_{st}(C_2H_2)$ comparison.

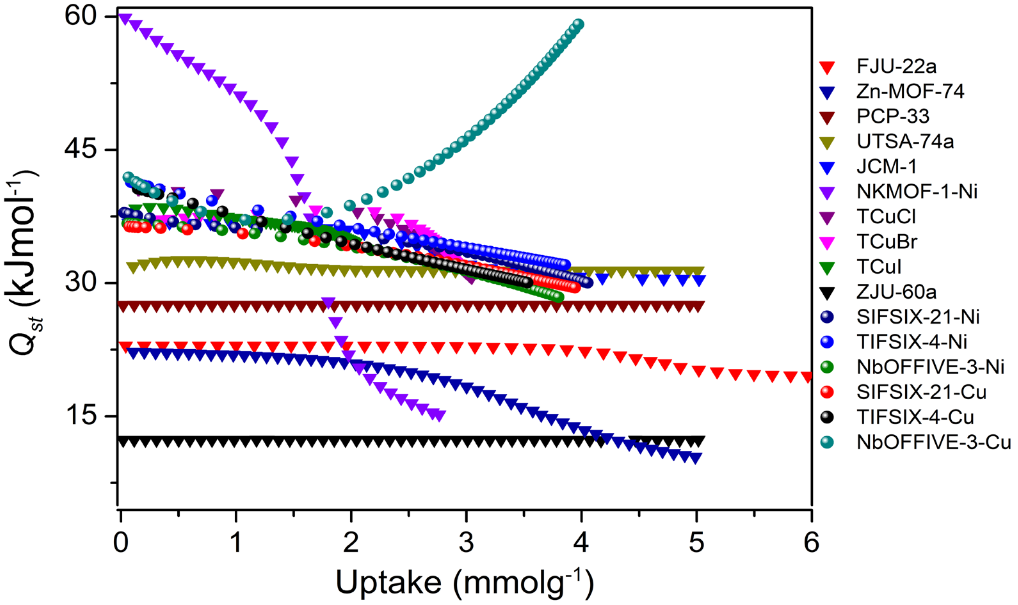

Figure S58. Comparison of isosteric heat of adsorption profiles for C_2H_2, considering all the C_2H_2/CO_2 separating MOM physisorbents.

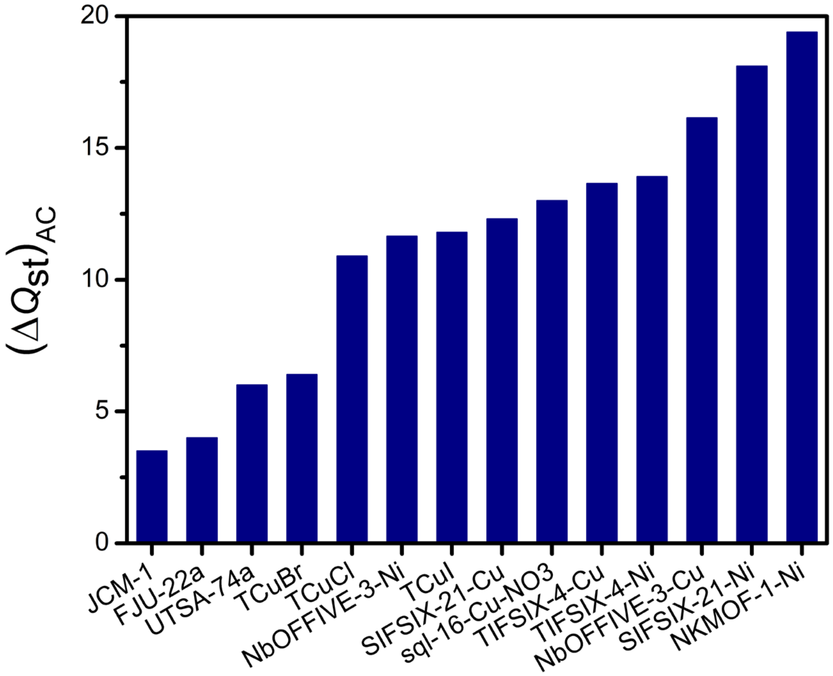

Figure S59. Comparison of $\Delta Q_{st}(C_2H_2/CO_2)$ at low loading, considering all the C_2H_2/CO_2 separating MOM physisorbents.

***In situ* Infrared (IR) spectra.**

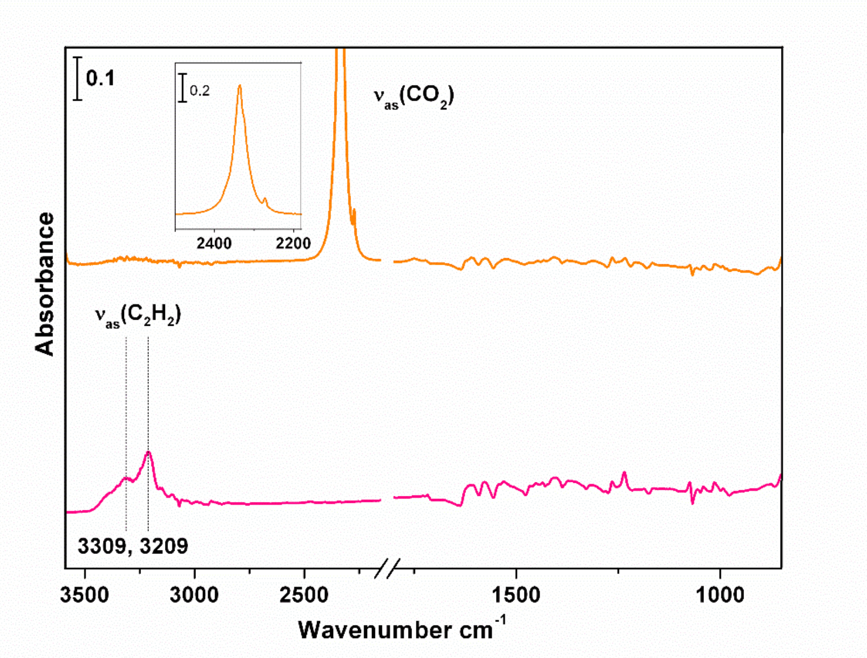

Figure. S60. Difference IR spectra showing the adsorbed CO_2 (orange) and C_2H_2 (pink) upon loading at 1 bar adsorbate pressure into **SIFSIX-21-Ni** and subsequent evacuation of the gas phase within 3 seconds, respectively. Each is referenced to the spectrum of activated HUMs. Inset shows the $\nu_{as}(CO_2)$ band.

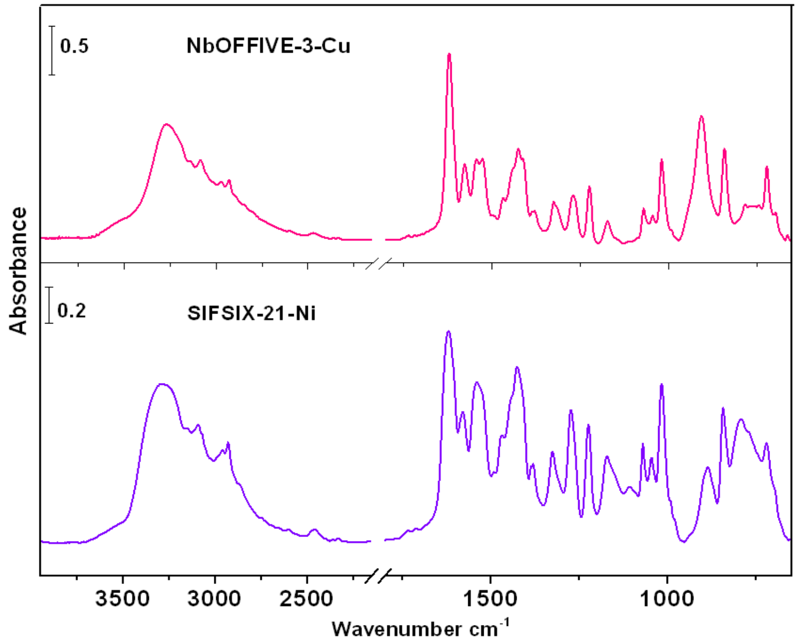

Figure S61. IR spectra of activated **NbOFFIVE-3-Cu** (top) and **SIFSIX-21-Ni** (bottom), referenced to pure KBr pellet in vacuum ($< 2.66645 \times 10^{-5}$ bar base pressure).

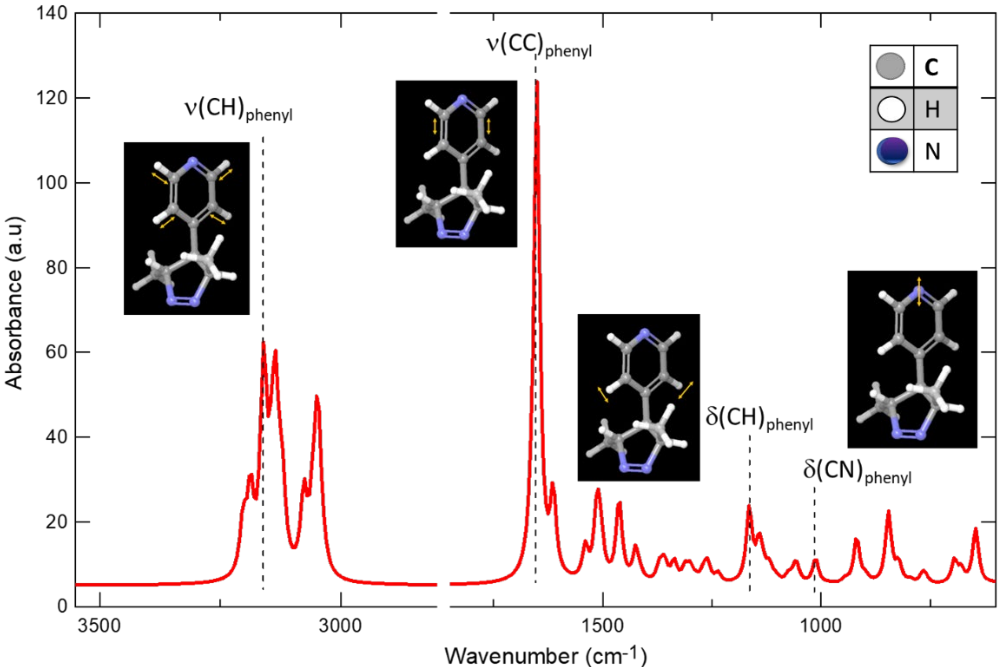

Figure S62. IR spectrum of pypz from DFT calculation.

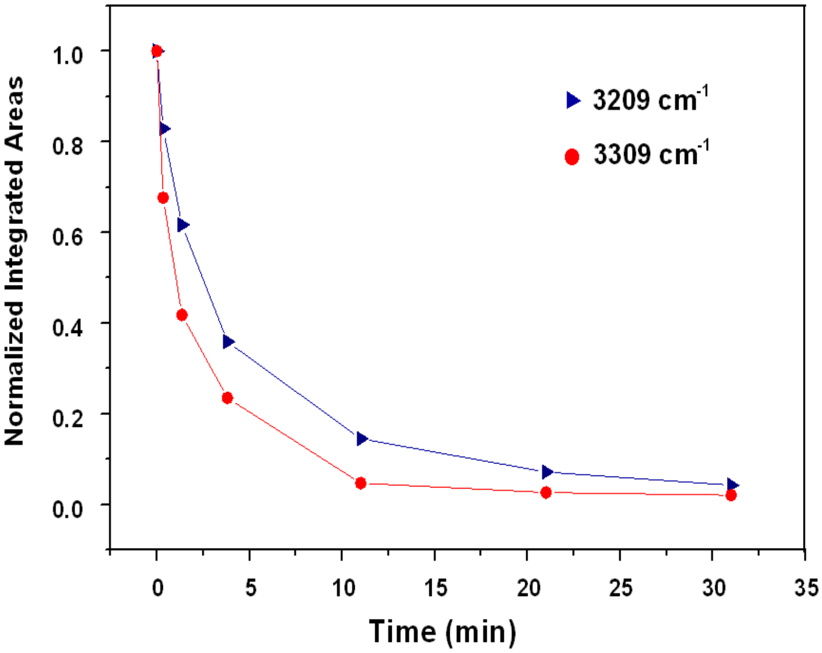

Figure S63. Evolution of the $\nu_{as}(C_2H_2)$ bands at 3308 (triangle) and 3209 cm^{-1} (circle) in **NbOFFIVE-3-Cu** under vacuum.

Solid-state NMR spectra

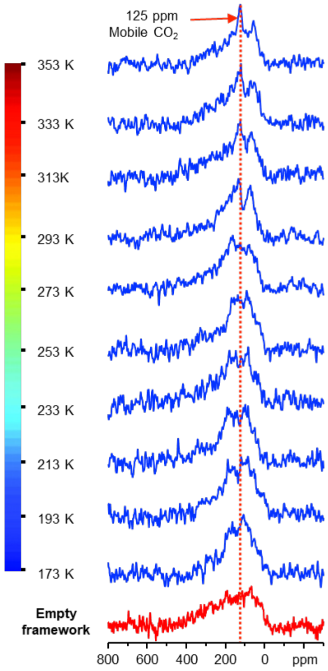

Figure S64. Experimental ^{13}C static NMR spectra of $^{13}CO_2$ adsorbed in **NbOFFIVE-3-Cu** as a function of temperature (blue line) and the spectrum of activated **NbOFFIVE-3-Cu** (red line).

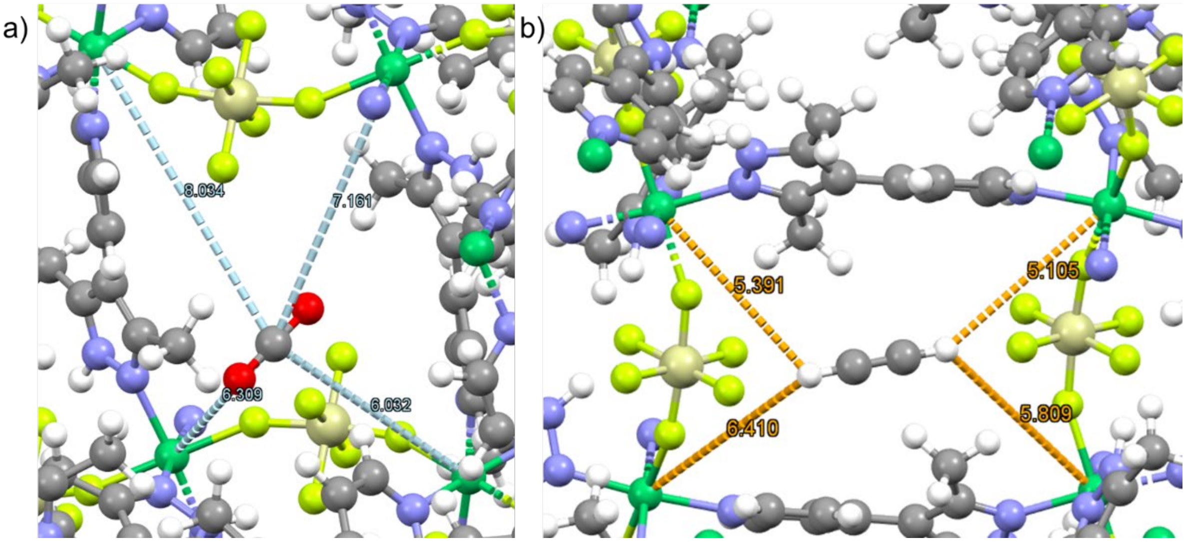

Figure S65. a) Modelled structure of **NbOFFIVE-3-Cu** showing the distances between the $C^{\delta+}$ of CO_2 and the nearby Cu(II) centres. b) Modelled structure of **NbOFFIVE-3-Cu** showing the distances between the H atoms in C_2H_2 and the nearby Cu(II) centres. Note: the structure of **SIFSIX-21-Ni** is used instead of the isostructural HUM **NbOFFIVE-3-Cu**.

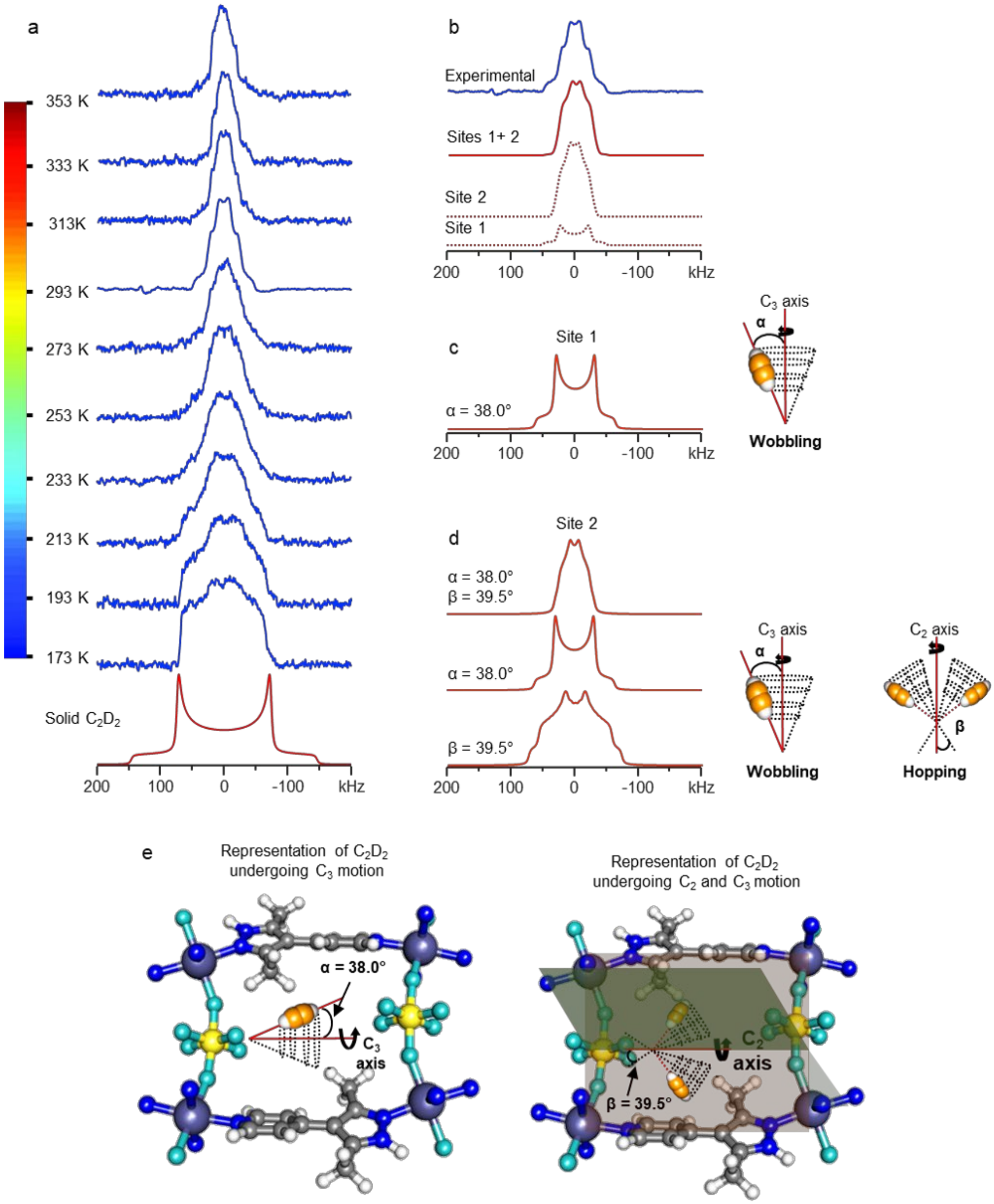

Figure S66. a) Experimental ^{2}H static spectra of 0.4 C_2D_2 per Cu adsorbed in **NbOFFIVE-3-Cu** as a function of temperature (blue line) and simulated ^{2}H spectrum of static C_2D_2. b) Experimental (blue) and simulated static ^{2}H spectra showing two different sites. c) Simulated ^{2}H spectra of C_2D_2 at site 1. Dynamical model for simulation: rotation of the C_2D_2 about a C_3 axis. d) Simulated ^{2}H spectra of C_2D_2 at site 2. Dynamical model for simulation: rotation of the C_2D_2 about a C_3 axis followed by a two-site hopping motion. e) Illustration of the dynamical models of C_2D_2 within **NbOFFIVE-3-Cu**. Note: the structure of **SIFSIX-21-Ni** is used instead of the isostructural HUM **NbOFFIVE-3-Cu**.

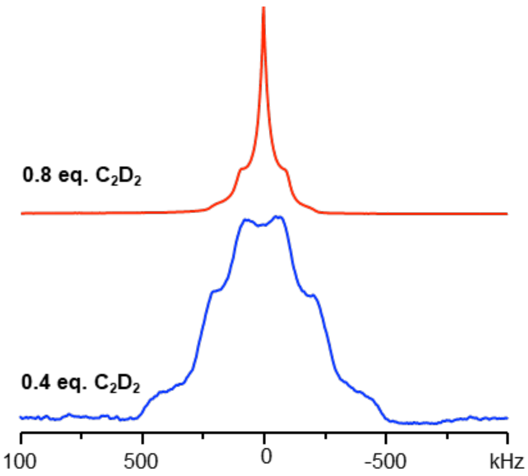

Figure S67. Comparison of experimental ^{2}H static NMR spectra of **NbOFFIVE-3-Cu** loaded with 0.4 and 0.8 C_2D_2 per Cu at room temperature.

Accelerated Stability Tests.

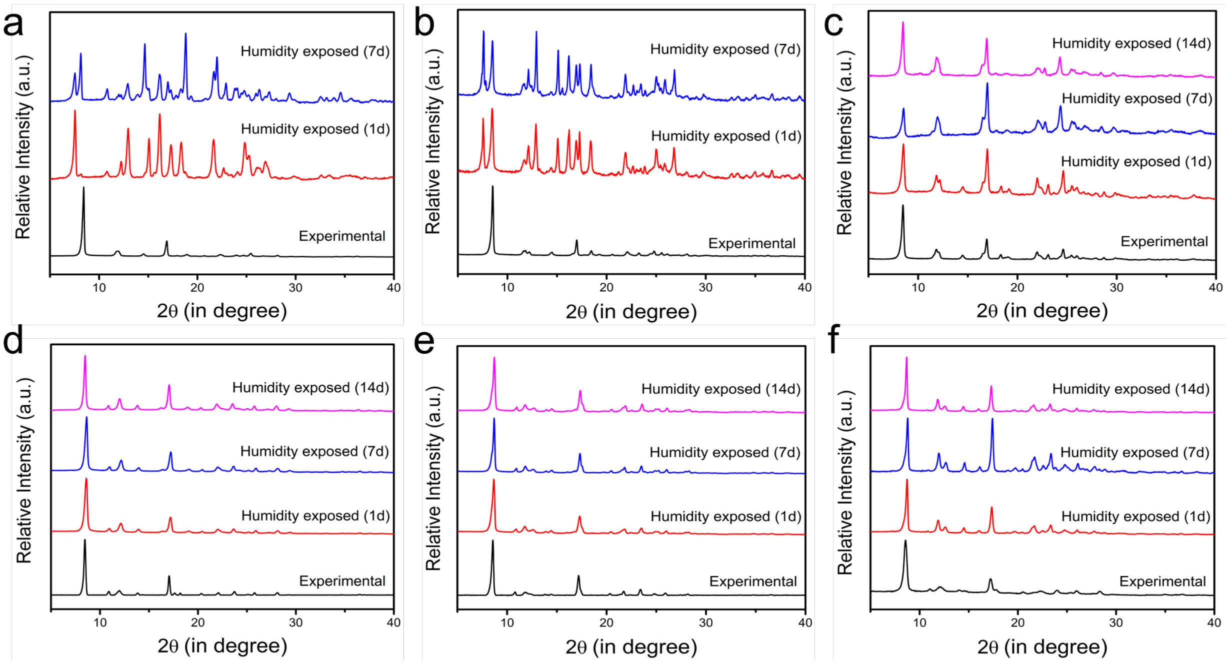

Figure S68. Comparison of experimental and calculated PXRD patterns with those of the three distinct humidity exposed phases: 1, 7 and 14 days a: **SIFSIX-21-Ni**, b: **TIFSIX-4-Ni**, c: **NbOFFIVE-3-Ni**, d: **SIFSIX-21-Cu**, e: **TIFSIX-4-Cu**, f: **NbOFFIVE-3-Cu**.

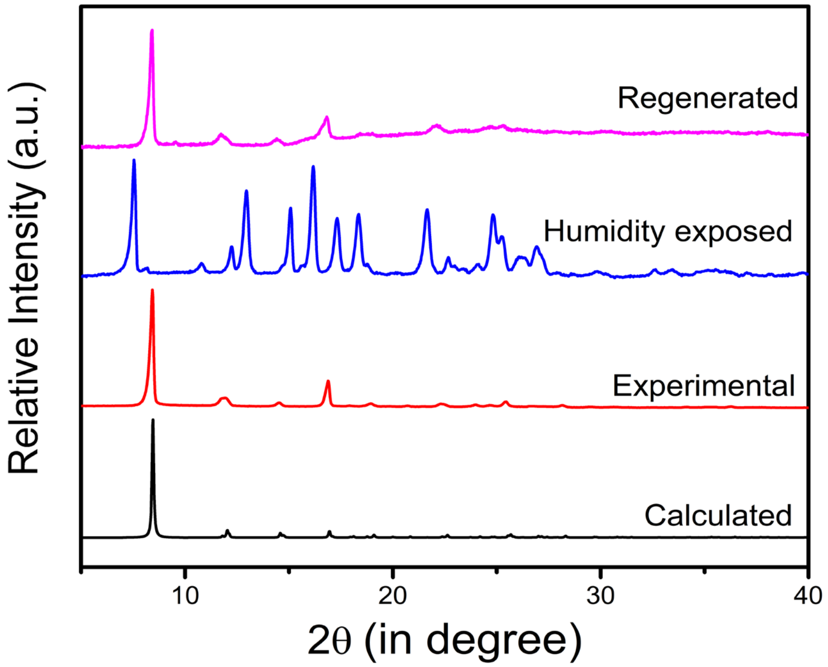

Figure S69. PXRD patterns of calculated (black), as-synthesised samples (red), the samples after exposed to humidity for a day (blue) and the regenerated **SIFSIX-21-Ni** (pink) in methanol solution.

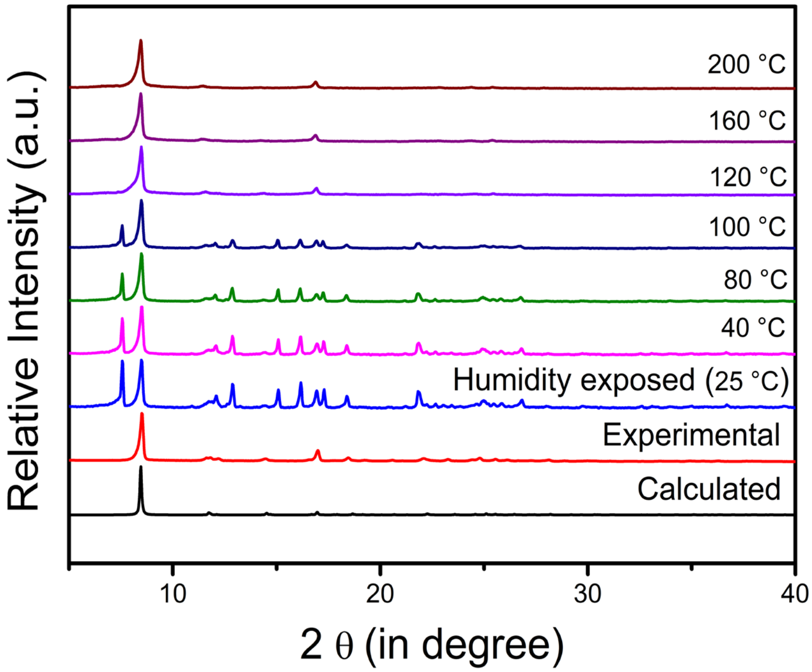

Figure S70. VT-PXRD profiles for humidity exposed samples (for 1 day) of **TIFSIX-4-Ni**.

Supplemental figures for the previously unreported HUMs.

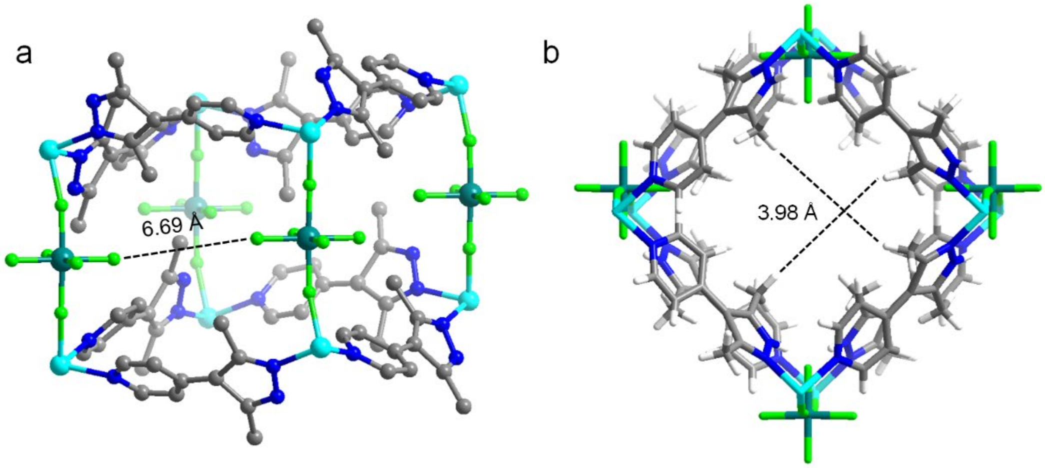

Figure S71. (a) View of the C_2H_2 binding pocket in adsorbent **TIFSIX-4-Ni** along the diagonally opposite F atoms of TiF_6^{2-} pillars; (b) View of the ultramicropore along the crystallographic b-axis of **TIFSIX-4-Ni**.

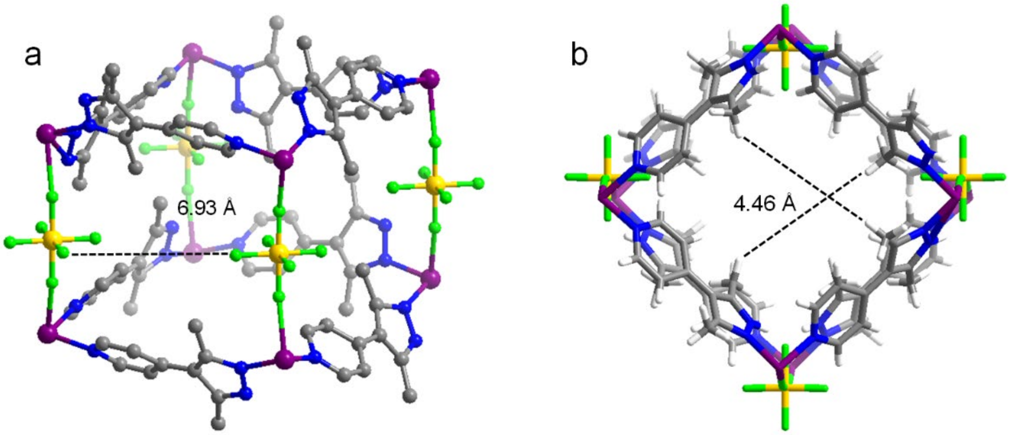

Figure S72. (a) View of the C_2H_2 binding pocket in adsorbent **SIFSIX-21-Cu** along the diagonally opposite F atoms of SiF_6^{2-} pillars; (b) View of the ultramicropore along the crystallographic b-axis of **SIFSIX-21-Cu**.

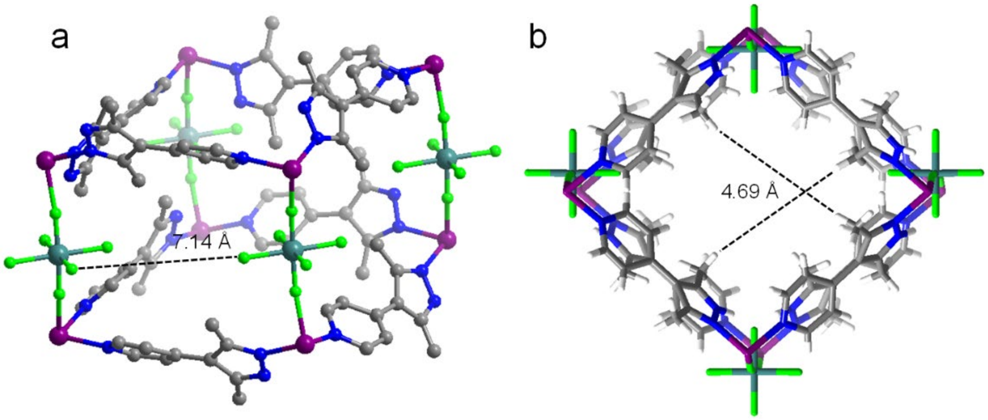

Figure S73. (a) View of the C_2H_2 binding pocket in adsorbent **TIFSIX-4-Cu** along the diagonally opposite F atoms of TiF_6^{2-} pillars; (b) View of the ultramicropore along the crystallographic b-axis of **TIFSIX-4-Cu**.

Tables S1-S4.

Table S1. Summary of structural information, sorption data and C_2H_2/CO_2 selectivities.

Material	Pore size (Å × Å)	S_{BET} / m^2g^{-1}	C_2H_2/CO_2 Q_{st} at zero loading (kJ mol^{-1})	C_2H_2/CO_2 Q_{st} at half loading (kJ mol^{-1})	C_2H_2/CO_2 uptakes at 1 bar,[a] mmol g^{-1}	S_{AC}[b]	α_{AC} (1:1/2:1)	Ref
$[Cu_2(pzdc)_2(pyz)]$[c]	4.0 × 6.0	571	42.5/31.9	–	1.9/0.07	26[d]	–	55, 56
Zn-MOF-74	11.0 × 11.0	1360	22.1/26.8	–	5.5/5.4	4[e]	–	57, 58
ZJU-60a	4.4 × 5.4	1627	17.6/15.2	–	6.7/3.3	6.7[e]	–	59
MIL–100(Fe)	5.5 × 8.6	2300	65.0/30.0	–	5.3/2.5	12.5[e]	–	60
PCP-33	9.0 × 22.0	1248	27.5/26.3	–	5.4/2.6	5.6[e]	–	61
FJU-22a	7.1 × 7.1	828	23.0/19.0	22.9/19.4	5.1/5.0	7.1[e]	1.9/–	12
UTSA-74a	8.0 × 8.0	830	31.0/25.0	31.4/25.5	4.8/3.2	14.3[e]	20.1/–	58
TIFSX-2-Cu-i	5.1 × 5.1	685	46.0/36.0	41.9/34.6	4.1/4.3	10.0[e]/10.7[f]	–/50[g]	62
UTSA-300a	2.4 × 3.3	311	57.6[h],30.0[i]/–	–	3.3/0.2	743	–	63
DICRO-4-Ni-i	6.2 × 6.6	398	37.7/33.9	35.4/34.6	1.9/1.0	18.2[e]/13.9[j]	–/13[g]	31
NKMOF-1-Ni	5.8 × 5.8	382	60.3/40.9	46.0/36.4	2.7/2.3	~60[e],[f]	2.6/1.8	64
JCM-1	12.5 × 3.9	550	36.9/33.4	–	3.3/1.7	13[e]	4.4/–	65
ZJU-196	5.1 × 5.1	–	39.2[h],15[i]/–	–	3.7/0.4	25[k]	–	66
$[Ni_3(HCOO)_6]$	4.3 × 4.3	289	40.9/24.5	–	2.4/1.6	22[l]	–	67
FJU-90a	5.4 × 5.1	1572	25.1/20.7	–	8.0/4.6	4.3[l]	–	68
JNU-1	16.3 × 6.6	818	13.0, 47.6[m]/–	–	2.7/2.2	3[e]	–	69
MUF-17	4.7 × 4.8	247	49.5/33.8	–	2.7[n]/2.2[n]	6[e]	–	70
ZJUT-2a	3.2 × 3.2	350	41.5/35.5	–	3.4/2.2	10[l]	–	71
FJU-89a	12 × 8	774	31.0/27.8	24.9/23.5	4.5/2.7	4.3	3	72
HOF-3	7.0 × 7.0	165	20.0	–	2.1/0.9	14.0	2.0	73
FJU-6-TATB	(15.6 × 6.4),	1306	29.0/26.0	–	4.9/2.6	5.3-3.1	2.3	74

	(16.9 × 21.9)							
SNNU-45	4.5 × 5.1	1006	39.9/27.1	31/26.9	6.0/4.3	8.5-4.5	2.9	75
JXNU-5	4.6, 6.7	406	32.9/25.2	30.2/26.8	2.5/1.5	5	9.9	76
FJU-36a	(9.1 × 13.4); (10.2 × 15.4)	409	32.9/31.1	–	2.3/1.6	2.8	2.1	77
FeNi-M′MOF	(4.15 × 4.27); (3.94 × 4.58)	383	27.0/24.5	27.0/24.9	4.3/2.7	24	1.7	78
TCuI	3.66 × 3.66	250	38.4/26.6	37.3/29.6	2.2/1.6	6.7[e]/6.5[f]	33.4/7.8	79
TCuBr	3.59 × 3.59	173	36.6/30.2	38.2/32.7	2.8/2.0	9.1[e]/9.1[f]	104.5/10.5	79
TCuCl	3.69 × 3.69	167	41.0/30.1	39.5/31.4	3.0/2.0	16.0[e]/16.1[f]	143.1/25.4	79
FJI-H8-Me	-	2044±3	33.7/21.8	-	10.2/4.7	10.4	-	80
SIFSIX-Cu-TPA	-	1330	39.1/25.7	-	8.3/4.8	5.3	1.97	81
SIFSIX-21-Ni	3.16 × 3.64	871	37.9/19.8	35.2/20.3	4.0/1.3	7.8	27.7/10.0	**This work**
TIFSIX-4-Ni	3.98 × 3.98	931	41.4/27.4	36.4/25.5	3.8/2.0	7.6	4.4/3.1	**This work**
NbOFFIVE-3-Ni	-	761	36.7/25.0	33.4/25.6	3.8/1.9	6.0	15.0/6.5	**This work**
SIFSIX-21-Cu	4.46 × 4.46	839	36.3/24.0	34.2/23.8	3.9/1.5	10.0	4.6/3.1	**This work**
TIFSIX-4-Cu	4.69 × 4.69	747	40.6/27.0	35.1/26.4	3.5/2.0	8.3	5.4/4.1	**This work**
NbOFFIVE-3-Cu	-	805	41.9/25.8	38.6/23.4	4.0/1.6	9.5	16.9/7.9	**This work**

[a] Unless otherwise mentioned, all values correspond to 298 K measurements; [b] unless otherwise mentioned, all values are calculated from IAST selectivities for 1:1 equimolar mixtures; [c] title compound is a metal-organic complex with 1D channels; [d] uptake ratio at 0.01 bar for 270 K measurements; [e] IAST selectivity at 0.15 bar for 1:1 ratio; [f] IAST selectivity at 0.15 bar for 2:1 ratio; [g] for gas mixture 10:5:85 $C_2H_2/CO_2/He$; [h] at zero loading; [i] consistent for loadings > 0.22 mmol g^{-1}; [j] uptake at 0.01 bar; [k] uptake ratio at 0.5 bar; [l] IAST selectivity at 1 bar for 1:1 ratio; [m] at uptake 2 mmol g^{-1}; [n] recorded at 293 K. [o] determined from Horvath–Kawazoe method applied on N_2 isotherm at 77 K.

Table S2. Crystallographic data of **SIFSIX-21-Ni**, **TIFSIX-4-Ni, SIFSIX-21-Cu** and **TIFSIX-21-Cu**.

	SIFSIX-21-Ni	**TIFSIX-4-Ni**	**SIFSIX-21-Cu**	**TIFSIX-4-Cu**
Formula	$C_{23}H_{34}F_6N_6NiO_3Si$	$C_{23}H_{34}F_6N_6NiO_3Ti$	$C_{26}H_{42}CuF_6N_6O_6Si$	**$C_{25}H_{40}CuF_6N_6O_5Ti$**
Formula weight	643.33	663.108	740.28	**730.02**
Temperature/K	100.0	100.0	120.0(5)	**120.00(12)**
Crystal system	orthorhombic	orthorhombic	orthorhombic	**orthorhombic**
Space group	*Pnna*	*Pnna*	*Pnna*	***Pnna***
a/Å	14.8769(12)	14.9625(11)	14.9853(16)	**16.2099(14)**
b/Å	14.6342(11)	15.0720(12)	15.7634(10)	**14.7716(14)**
c/Å	14.6946(11)	14.5962(12)	14.2288(16)	**14.445(2)**
α/°	90	90	90	**90**
β/°	90	90	90	**90**
γ/°	90	90	90	**90**
Volume/Å^3	3199.2(4)	3291.7(5)	3361.1(6)	**3458.8(7)**
Z	4	4	4	**4**
ρ_{calc}, g/cm^3	1.335	1.338	1.463	**1.402**
μ/mm^{-1}	1.845	3.365	1.982	**0.918**
F(000)	1113	1145.2	1124.0	**1156.0**
Radiation	CuKα (λ = 1.54178)	CuKα (λ = 1.54178)	CuKα (λ = 1.54184)	**Mo *Kα* (λ = 0.71073 Å)**
Reflections collected	17785	19154	18207	**15644**
Independent reflections	1758 [R_{int} = 0.0849, R_{sigma} = 0.0427]	2516 [R_{int} = 0.0700, R_{sigma} = 0.0468]	3516 [R_{int} = 0.1237, R_{sigma} = 0.0795]	**3857 [R_{int} = 0.1230, R_{sigma} = 0.1354]**
Data/restraints/parameters	1758/194/240	2516/126/240	3516/255/235	**3857/257/193**
Goodness-of-fit on F^2	1.065	1.335	0.956	**0.994**
Final R indexes [I>=2σ (I)]	R_1 = 0.0764, wR_2 = 0.2105	R_1 = 0.0986, wR_2 = 0.2798	R_1 = 0.0946, wR_2 = 0.2621	**R_1 = 0.1167, wR_2 = 0.2982**
Final R indexes [all data]	**R_1 = 0.0936, wR_2 = 0.2303**	**R_1 = 0.1069, wR_2 = 0.2951**	**R_1 = 0.1358, wR_2 = 0.3034**	**R_1 = 0.1722, wR_2 = 0.3432**

Table S3. DSLF fitting parameters summary for C_2H_2 and CO_2 sorption.

Adsorbent	**gas**	q_1	k_1	n_1	q_2	k_2	n_2	R^2
NbOFFIVE-3-Ni	C_2H_2	3.591	0.0006	0.965	3.125	0.008	0.954	0.999
	CO_2	4.609	0.0008	1.180	0.180	0.009	0.939	0.999
SIFSIX-21-Ni	C_2H_2	4.060	0.006	1.878	0.059	4173.33	15.759	0.998
	CO_2	6.581	0.0003	1.048	0.094	0.0008	0.657	0.999
TIFSIX-4-Ni	C_2H_2	4.08225	1.6914	0.852066	1.40998	19.4212	0.991972	0.999
	CO_2	1 2.352	0.668	1.469	1.995	1.320	0.984	0.999
NbOFFIVE-3-Cu	C_2H_2	0.551	1.089	4.068	4.331	5.973	0.914	0.999
	CO_2	1.398	0.671	1.923	2.466	0.904	1.033	0.999
SIFSIX-21-Cu	C_2H_2	3.614	9.498	1.162	0.691	1.435	3.729	0.999
	CO_2	9.033	0.187	0.985	0.0140	5.9e-08	218.447	0.999
TIFSIX-4-Cu	C_2H_2	4.681	1.585	0.757	0.782	51.723	1.032	0.999
	CO_2	2.293	1.121	0.982	1.746	0.815	1.558	1

Table S4: Calculated averaged total potential energies (in kJ mol^{-1}) for a single C_2H_2 and CO_2 molecule, individually, positioned at their global minimum in **SIFSIX-21-Ni** as determined from CMC simulations at 298 K/0.10 atm.

Adsorbate	**HUM–Adsorbate Energy (kJ mol^{-1})**
C_2H_2	–40.40
CO_2	–25.85

References.

1. Waterman, K. C., Understanding and Predicting Pharmaceutical Product Shelf-Life. In *Handbook of Stability Testing in Pharmaceutical Development: Regulations, Methodologies, and Best Practices*, Huynh-Ba, K., Ed. Springer New York: New York, **2009**; pp 115-135.
2. Kumar, A.; Hua, C.; Madden, D. G.; O'Nolan, D.; Chen, K.-J.; Keane, L.-A. J.; Perry, J. J.; Zaworotko, M. J., Hybrid ultramicroporous materials (HUMs) with enhanced stability and trace carbon capture performance. *Chem.Commun.* **2017**, *53*, 5946-5949.
3. Krause, L.; Herbst-Irmer, R.; Sheldrick, G. M.; Stalke, D., Comparison of silver and molybdenum microfocus X-ray sources for single-crystal structure determination. *J. Appl. Crystallogr.* **2015,** *48*, 3-10.
4. Shen, J.; He, X.; Ke, T.; Krishna, R.; van Baten, J. M.; Chen, R.; Bao, Z.; Xing, H.; Dincǎ, M.; Zhang, Z.; Yang, Q.; Ren, Q., Simultaneous interlayer and intralayer space control in two-dimensional metal−organic frameworks for acetylene/ethylene separation. *Nat. Commun.* **2020**, *11*, 6259.
5. Sheldrick, G., SHELXT - Integrated space-group and crystal-structure determination. *Acta Crystallogr., Sect. A* **2015**, *71*, 3-8.
6. Sheldrick, G., Crystal structure refinement with SHELXL. *Acta Crystallogr., Sect. C* **2015**, *71*, 3-8.
7. Dolomanov, O. V.; Bourhis, L. J.; Gildea, R. J.; Howard, J. A. K.; Puschmann, H., OLEX2: a complete structure solution, refinement and analysis program. *J. Appl. Crystallogr.* **2009**, *42*, 339-341.
8. Rohatgi, A., *WebPlotDigitalizer: HTML5 based online tool to extract numerical data from plot images* **2015**, *Version: 4.2*.
9. Origin(Pro), Version 2021. OriginLab Corporation, Northampton, MA, USA..
10. Myers, A. L.; Prausnitz, J. M., Thermodynamics of mixed-gas adsorption. *AIChE J.* **1965**, *11*, 121-127.
11. Yang, R. T., *Gas separation by adsorption processes*. Butterworth-Heinemann: **2013**.
12. Yao, Z.; Zhang, Z.; Liu, L.; Li, Z.; Zhou, W.; Zhao, Y.; Han, Y.; Chen, B.; Krishna, R.; Xiang, S., Extraordinary Separation of Acetylene-Containing Mixtures with Microporous Metal–Organic Frameworks with Open O Donor Sites and Tunable Robustness through Control of the Helical Chain Secondary Building Units. *Chem. Eur. J.* **2016**, *22*, 5676-5683.
13. Bochevarov, A. D.; Harder, E.; Hughes, T. F.; Greenwood, J. R.; Braden, D. A.; Philipp, D. M.; Rinaldo, D.; Halls, M. D.; Zhang, J.; Friesner, R. A., Jaguar: A high-performance quantum chemistry software program with strengths in life and materials sciences. *Int. J. Quantum Chem.* **2013**, *113*, 2110-2142.
14. Schrödinger Release 2020-1: Jaguar, Schrödinger, LLC, New York, NY. 2020] in the Schrödinger software suite (Release 2020-1).
15. Grimme, S.; Antony, J.; Ehrlich, S.; Krieg, H. *J. Chem. Phys.* **2010**, *132*, 154104.
16. Hehre, W. J.; Radom, L.; von R. Schleyer, P.; Pople, J. A. Ab initio molecular orbital theory (Wiley, New York, 1986).
17. Schrödinger Release 2020-1: Maestro, Schrödinger, LLC, New York, NY, **2020**.
18. Chen, M.; Chen, S.; Chen, W.; Lucier, B. E. G.; Zhang, Y.; Zheng, A.; and Huang, Y. Analyzing Gas Adsorption in an Amide-Functionalized Metal Organic Framework: Are the Carbonyl or Amine Groups Responsible? *Chem. Mater.*, **2018**, *30*, 3613-3617.

19. Gul-E-Noor, F.; Mendt, M.; Michel, D.; Pöppl, A.; Krautscheid, H.; Haase, J.; and Bertmer, M. Adsorption of Small Molecules on $Cu_3(btc)_2$ and $Cu_{3-x}Zn_x(btc)_2$ Metal–Organic Frameworks (MOF) As Studied by Solid-State NMR. *J. Phys. Chem. C* **2013**, *117*, 7703-7712.
20. Eichele, K., WSolids1, Version 1.20.15. Universität Tübingen: Tübingen, Germany, 2011.
21. Vold, R. L.; Hoatson, G. L., Effects of jump dynamics on solid state nuclear magnetic resonance line shapes and spin relaxation times. *J. Magn. Reson*. **2009**, *198*, 57-72.
22. Kruger, P. E.; Moubaraki, B.; Fallon, G. D.; Murray, K. S., Tetranuclear copper(II) complexes incorporating short and long metal–metal separations: synthesis, structure and magnetism. *J. Chem. Soc., Dalton Trans.* **2000**, 713-718.
23. Jorgensen, W. L.; Maxwell, D. S.; Tirado-Rives, J., Development and Testing of the OPLS All-Atom Force Field on Conformational Energetics and Properties of Organic Liquids. *J. Am. Chem. Soc.* **1996**, *118*, 11225-11236.
24. Rappe, A. K.; Casewit, C. J.; Colwell, K. S.; Goddard, W. A.; Skiff, W. M., UFF, a full periodic table force field for molecular mechanics and molecular dynamics simulations. *J. Am. Chem. Soc.* **1992**, *114*, 10024-10035.
25. Bayly, C. I.; Cieplak, P.; Cornell, W.; Kollman, P. A., A well-behaved electrostatic potential based method using charge restraints for deriving atomic charges: the RESP model. *J. Phys. Chem.* **1993**, *97*, 10269-10280.
26. Kühne, T. D.; Iannuzzi, M.; Del Ben, M.; Rybkin, V. V.; Seewald, P.; Stein, F.; Laino, T.; Khaliullin, R. Z.; Schütt, O.; Schiffmann, F.; Golze, D.; Wilhelm, J.; Chulkov, S.; Bani-Hashemian, M. H.; Weber, V.; Borštnik, U.; Taillefumier, M.; Jakobovits, A. S.; Lazzaro, A.; Pabst, H.; Müller, T.; Schade, R.; Guidon, M.; Andermatt, S.; Holmberg, N.; Schenter, G. K.; Hehn, A.; Bussy, A.; Belleflamme, F.; Tabacchi, G.; Glöß, A.; Lass, M.; Bethune, I.; Mundy, C. J.; Plessl, C.; Watkins, M.; VandeVondele, J.; Krack, M.; Hutter, J., CP2K: An electronic structure and molecular dynamics software package - Quickstep: Efficient and accurate electronic structure calculations. *J. Chem. Phys.* **2020**, *152*, 194103.
27. van Duijnen, P. T.; Swart, M., Molecular and Atomic Polarizabilities: Thole's Model Revisited. *J. Phys. Chem. A* **1998**, *102*, 2399-2407.
28. Pham, T.; Forrest, K. A.; McLaughlin, K.; Tudor, B.; Nugent, P.; Hogan, A.; Mullen, A.; Cioce, C. R.; Zaworotko, M. J.; Space, B., Theoretical Investigations of CO_2 and H_2 Sorption in an Interpenetrated Square-Pillared Metal–Organic Material. *J. Phys. Chem. C* **2013**, *117*, 9970-9982.
29. Pham, T.; Forrest, K. A.; Banerjee, R.; Orcajo, G.; Eckert, J.; Space, B., Understanding the H_2 Sorption Trends in the M-MOF-74 Series (M = Mg, Ni, Co, Zn). *J. Phys. Chem. C* **2015**, *119*, 1078-1090.
30. Kirkpatrick, S.; Gelatt, C. D.; Vecchi, M. P., Optimization by Simulated Annealing. *Science* **1983**, *220*, 671.
31. Scott, H. S.; Shivanna, M.; Bajpai, A.; Madden, D. G.; Chen, K.-J.; Pham, T.; Forrest, K. A.; Hogan, A.; Space, B.; Perry Iv, J. J.; Zaworotko, M. J., Highly Selective Separation of C_2H_2 from CO_2 by a New Dichromate-Based Hybrid Ultramicroporous Material. *ACS Appl. Mater. Interfaces* **2017**, *9*, 33395-33400.
32. Mullen, A. L.; Pham, T.; Forrest, K. A.; Cioce, C. R.; McLaughlin, K.; Space, B., A Polarizable and Transferable PHAST CO_2 Potential for Materials Simulation. *J. Chem. Theory Comput.* **2013**, *9*, 5421-5429.

33. Jones, J. E.; Chapman, S., On the determination of molecular fields- II. From the equation of state of a gas. *Proc. Math. Phys. Eng. Sci.* **1924**, *106*, 463-477.
34. Ewald, P. P., Die Berechnung optischer und elektrostatischer Gitterpotentiale. *Ann. Phys. (Berl.)* **1921**, *369*, 253-287.
35. Wells, B. A.; Chaffee, A. L., Ewald Summation for Molecular Simulations. *J. Chem. Theory Comput.* **2015**, *11*, 3684-3695.
36. Applequist, J.; Carl, J. R.; Fung, K.-K., Atom dipole interaction model for molecular polarizability. Application to polyatomic molecules and determination of atom polarizabilities. *J. Am. Chem. Soc.* **1972**, *94*, 2952-2960.
37. Thole, B. T., Molecular polarizabilities calculated with a modified dipole interaction. *Chem. Phys.* **1981**, *59*, 341-350.
38. Bode, K. A.; Applequist, J., A New Optimization of Atom Polarizabilities in Halomethanes, Aldehydes, Ketones, and Amides by Way of the Atom Dipole Interaction Model. *J. Phys. Chem.* **1996**, *100*, 17820-17824.
39. McLaughlin, K.; Cioce, C. R.; Pham, T.; Belof, J. L.; Space, B., Efficient calculation of many-body induced electrostatics in molecular systems. *J. Chem. Phys.* **2013**, *139*, 184112.
40. Belof, J. L.; Space, B. Massively Parallel Monte Carlo (MPMC). 2012, Available on GitHub. https://github.com/mpmccode/mpmc.
41. Franz, D. M.; Belof, J. L.; McLaughlin, K.; Cioce, C. R.; Tudor, B.; Hogan, A.; Laratelli, L.; Mulcair, M.; Mostrom, M.; Navas, A.; Stern, A. C.; Forrest, K. A.; Pham, T.; Space, B., MPMC and MCMD: Free High-Performance Simulation Software for Atomistic Systems. *Adv. Theory Simul.* **2019**, *2*, 1900113.
42. Kresse, G.; Furthmuller, J., Efficiency of ab-initio total energy calculations for metals and semiconductors using a plane-wave basis set. *Comp. Mater. Sci.* **1996**, *6*, 15-50.
43. Kresse, G.; Furthmuller, J., Efficient iterative schemes for ab initio total-energy calculations using a plane-wave basis set. *Phys. Rev. B* **1996**, *54*, 11169-11186.
44. Wellendorff, J.; Lundgaard, K. T.; Møgelhøj, A.; Petzold, V.; Landis, D. D.; Nørskov, J. K.; Bligaard, T.; Jacobsen, K. W., Density functionals for surface science: Exchange-correlation model development with Bayesian error estimation. *Phys. Rev. B* **2012**, *85*, 235149.
45. Blochl, P. E., Projector augmented-wave Method. *Phys. Rev. B* **1994**, *50*, 17953-17979.
46. Pack, J. D.; Monkhorst, H. J., "Special points for Brillouin-zone integrations"-a reply. *Phys. Rev. B* **1977**, *16*, 1748-1749.
47. Monkhorst, H. J.; Pack, J. D., Special points for Brillouin-zone integrations. *Phys. Rev. B* **1976**, *13*, 5188-5192.
48. Vandichel, M.; Hajek, J.; Vermoortele, F.; Waroquier, M.; De Vos, D. E.; Van Speybroeck, V., Active site engineering in UiO-66 type metal-organic frameworks by intentional creation of defects: a theoretical rationalization. *Crystengcomm* **2015**, *17*, 395-406.
49. Vandichel, M.; Hajek, J.; Ghysels, A.; De Vos, A.; Waroquier, M.; Van Speybroeck, V., Water coordination and dehydration processes in defective UiO-66 type metal organic frameworks. *Crystengcomm* **2016**, *18*, 7056-7069.
50. Ghysels, A.; Verstraelen, T.; Hemelsoet, K.; Waroquier, M.; Van Speybroeck, V., TAMkin: A Versatile Package for Vibrational Analysis and Chemical Kinetics. *J Chem Inf Model* **2010**, *50*, 1736-1750.

51. Sotomayor, F. J.; Cychosz, K. A.; Thommes, M., Characterization of micro/mesoporous materials by physisorption: concepts and case studies. *Acc. Mater. Surf. Res* **2018**, *3*, 34-50.
52. Schejn, A.; Aboulaich, A.; Balan, L.; Falk, V.; Lalevée, J.; Medjahdi, G.; Aranda, L.; Mozet, K.; Schneider, R., Cu^{2+}-doped zeolitic imidazolate frameworks (ZIF-8): efficient and stable catalysts for cycloadditions and condensation reactions. *Catal. Sci. Technol.* **2015**, *5*, 1829-1839.
53. Kooli, F.; Kiyozumi, Y.; Rives, V.; Mizukami, F., Synthesis and Textural Characterization of a New Microporous Silica Material. *Langmuir* **2002**, *18*, 4103-4110.
54. Liu, L.; Ma, D.; Zheng, H.; Li, X.; Cheng, M.; Bao, X., Synthesis and characterization of microporous carbon nitride. *Microporous and Mesoporous Materials* **2008**, *110*, 216-222.
55. Matsuda, R.; Kitaura, R.; Kitagawa, S.; Kubota, Y.; Belosludov, R. V.; Kobayashi, T. C.; Sakamoto, H.; Chiba, T.; Takata, M.; Kawazoe, Y.; Mita, Y., Highly controlled acetylene accommodation in a metal–organic microporous material. *Nature* **2005**, *436*, 238-241.
56. Bloch, E. D.; Queen, W. L.; Krishna, R.; Zadrozny, J. M.; Brown, C. M.; Long, J. R., Hydrocarbon Separations in a Metal-Organic Framework with Open Iron(II) Coordination Sites. *Science* **2012**, *335*, 1606-1610.
57. Xiang, S.; Zhou, W.; Zhang, Z.; Green, M. A.; Liu, Y.; Chen, B., Open Metal Sites within Isostructural Metal–Organic Frameworks for Differential Recognition of Acetylene and Extraordinarily High Acetylene Storage Capacity at Room Temperature. *Angew. Chem. Int. Ed.* **2010**, *49*, 4615-4618.
58. Luo, F.; Yan, C.; Dang, L.; Krishna, R.; Zhou, W.; Wu, H.; Dong, X.; Han, Y.; Hu, T.-L.; O'Keeffe, M.; Wang, L.; Luo, M.; Lin, R.-B.; Chen, B., UTSA-74: A MOF-74 Isomer with Two Accessible Binding Sites per Metal Center for Highly Selective Gas Separation. *J. Am. Chem. Soc.* **2016**, *138*, 5678-5684.
59. Duan, X.; Zhang, Q.; Cai, J.; Yang, Y.; Cui, Y.; He, Y.; Wu, C.; Krishna, R.; Chen, B.; Qian, G., A new metal–organic framework with potential for adsorptive separation of methane from carbon dioxide, acetylene, ethylene, and ethane established by simulated breakthrough experiments. *J. Mater. Chem. A* **2014**, *2*, 2628-2633.
60. Yoon, J. W.; Lee, J. S.; Lee, S.; Cho, K. H.; Hwang, Y. K.; Daturi, M.; Jun, C.-H.; Krishna, R.; Chang, J.-S., Adsorptive Separation of Acetylene from Light Hydrocarbons by Mesoporous Iron Trimesate MIL-100(Fe). *Chem. Eur. J.* **2015**, *21*, 18431-18438.
61. Duan, J.; Jin, W.; Krishna, R., Natural Gas Purification Using a Porous Coordination Polymer with Water and Chemical Stability. *Inorg. Chem.* **2015**, *54*, 4279-4284.
62. Chen, K.-J.; Scott, Hayley S.; Madden, D. G.; Pham, T.; Kumar, A.; Bajpai, A.; Lusi, M.; Forrest, K. A.; Space, B.; Perry, J. J.; Zaworotko, M. J., Benchmark C_2H_2/CO_2 and CO_2/C_2H_2 Separation by Two Closely Related Hybrid Ultramicroporous Materials. *Chem* **2016**, *1*, 753-765.
63. Lin, R.-B.; Li, L.; Wu, H.; Arman, H.; Li, B.; Lin, R.-G.; Zhou, W.; Chen, B., Optimized Separation of Acetylene from Carbon Dioxide and Ethylene in a Microporous Material. *J. Am. Chem. Soc.* **2017**, *139*, 8022-8028.
64. Peng, Y.-L.; Pham, T.; Li, P.; Wang, T.; Chen, Y.; Chen, K.-J.; Forrest, K. A.; Space, B.; Cheng, P.; Zaworotko, M. J.; Zhang, Z., Robust Ultramicroporous Metal–Organic Frameworks with Benchmark Affinity for Acetylene. *Angew. Chem. Int. Ed.* **2018**, *57*, 10971-10975.

65. Lee, J.; Chuah, C. Y.; Kim, J.; Kim, Y.; Ko, N.; Seo, Y.; Kim, K.; Bae, T. H.; Lee, E., Separation of Acetylene from Carbon Dioxide and Ethylene by a Water-Stable Microporous Metal–Organic Framework with Aligned Imidazolium Groups inside the Channels. *Angew. Chem. Int. Ed.* **2018**, *57*, 7869-7873.
66. Zhang, L.; Jiang, K.; Li, L.; Xia, Y.-P.; Hu, T.-L.; Yang, Y.; Cui, Y.; Li, B.; Chen, B.; Qian, G., Efficient separation of C_2H_2 from C_2H_2/CO_2 mixtures in an acid–base resistant metal–organic framework. *Chem. Commun.* **2018**, *54*, 4846-4849.
67. Zhang, L.; Jiang, K.; Zhang, J.; Pei, J.; Shao, K.; Cui, Y.; Yang, Y.; Li, B.; Chen, B.; Qian, G., Low-Cost and High-Performance Microporous Metal–Organic Framework for Separation of Acetylene from Carbon Dioxide. *ACS Sustain. Chem. Eng.* **2019**, *7*, 1667-1672.
68. Ye, Y.; Ma, Z.; Lin, R.-B.; Krishna, R.; Zhou, W.; Lin, Q.; Zhang, Z.; Xiang, S.; Chen, B., Pore Space Partition within a Metal–Organic Framework for Highly Efficient C_2H_2/CO_2 Separation. *J. Am. Chem. Soc.* **2019**, *141*, 4130-4136.
69. Zeng, H.; Xie, M.; Huang, Y.-L.; Zhao, Y.; Xie, X.-J.; Bai, J.-P.; Wan, M.-Y.; Krishna, R.; Lu, W.; Li, D., Induced Fit of C_2H_2 in a Flexible MOF Through Cooperative Action of Open Metal Sites. *Angew. Chem. Int. Ed.* **2019**, *58*, 8515-8519.
70. Qazvini, O. T.; Babarao, R.; Telfer, S. G., Multipurpose Metal–Organic Framework for the Adsorption of Acetylene: Ethylene Purification and Carbon Dioxide Removal. *Chem. Mater.* **2019**, *31*, 4919-4926.
71. Wen, H.-M.; Liao, C.; Li, L.; Yang, L.; Wang, J.; Huang, L.; Li, B.; Chen, B.; Hu, J., Reversing C_2H_2–CO_2 adsorption selectivity in an ultramicroporous metal–organic framework platform. *Chem. Commun.* **2019**, *55*, 11354-11357.
72. Ye, Y.; Chen, S.; Chen, L.; Huang, J.; Ma, Z.; Li, Z.; Yao, Z.; Zhang, J.; Zhang, Z.; Xiang, S., Additive-Induced Supramolecular Isomerism and Enhancement of Robustness in Co(II)-Based MOFs for Efficiently Trapping Acetylene from Acetylene-Containing Mixtures. *ACS Appl. Mater. Inter.* **2018**, *10*, 30912-30918.
73. Li, P.; He, Y.; Zhao, Y.; Weng, L.; Wang, H.; Krishna, R.; Wu, H.; Zhou, W.; O'Keeffe, M.; Han, Y.; Chen, B., A Rod-Packing Microporous Hydrogen-Bonded Organic Framework for Highly Selective Separation of C_2H_2/CO_2 at Room Temperature. *Angew. Chem. Int. Ed.* **2015**, *54*, 574-577.
74. Liu, L.; Yao, Z.; Ye, Y.; Yang, Y.; Lin, Q.; Zhang, Z.; O’Keeffe, M.; Xiang, S., Integrating the Pillared-Layer Strategy and Pore-Space Partition Method to Construct Multicomponent MOFs for C_2H_2/CO_2 Separation. *J. Am. Chem. Soc.* **2020**, *142*, 9258-9266.
75. Li, Y.-P.; Wang, Y.; Xue, Y.-Y.; Li, H.-P.; Zhai, Q.-G.; Li, S.-N.; Jiang, Y.-C.; Hu, M.-C.; Bu, X., Ultramicroporous Building Units as a Path to Bi-microporous Metal–Organic Frameworks with High Acetylene Storage and Separation Performance. *Angew. Chem. Int. Ed.* **2019**, *58*, 13590-13595.
76. Liu, R.; Liu, Q.-Y.; Krishna, R.; Wang, W.; He, C.-T.; Wang, Y.-L., Water-Stable Europium 1,3,6,8-Tetrakis(4-carboxylphenyl)pyrene Framework for Efficient C_2H_2/CO_2 Separation. *Inorg. Chem.* **2019**, *58*, 5089-5095.
77. Liu, L.; Yao, Z.; Ye, Y.; Chen, L.; Lin, Q.; Yang, Y.; Zhang, Z.; Xiang, S., Robustness, Selective Gas Separation, and Nitrobenzene Sensing on Two Isomers of Cadmium Metal–Organic Frameworks Containing Various Metal–O–Metal Chains. *Inorg. Chem.* **2018**, *57*, 12961-12968.

78. Gao, J.; Qian, X.; Lin, R.-B.; Krishna, R.; Wu, H.; Zhou, W.; Chen, B., Mixed Metal–Organic Framework with Multiple Binding Sites for Efficient C_2H_2/CO_2 Separation. *Angew. Chem. Int. Ed.* **2020**, *59*, 4396-4400.
79. Mukherjee, S.; He, Y.; Franz, D.; Wang, S.-Q.; Xian, W.-R.; Bezrukov, A. A.; Space, B.; Xu, Z.; He, J.; Zaworotko, M. J., Halogen–C_2H_2 Binding in Ultramicroporous Metal–Organic Frameworks (MOFs) for Benchmark C_2H_2/CO_2 Separation Selectivity. *Chem. Eur. J.* **2020**, *26*, 4923-4929.
80. Di, Z.; Liu, C.; Pang, J.; Chen, C.; Hu, F.;Yuan, D.; Wu, M.; Hong, M. Cage‐like Porous Materials with Simultaneous High C_2H_2 Storage and Excellent C_2H_2/CO_2 Separation Performance. *Angew. Chem. Int. Ed.* **2021**, https://doi.org/10.1002/anie.202101907.
81. Li, H.; Liu, C.; Chen, C.; Di, Z.; Yuan, D.; Pang, J.; Wei, W.; Wu, M.; Hong, M. An Unprecedented Pillar-Cage Fluorinated Hybrid Porous Framework with Highly Efficient Acetylene Storage and Separation. *Angew. Chem. Int. Ed.* **2021**, *60*, 7547-7552.